ISSN 2435-1288

Nikon Research Report

Vol.4 2022

Purpose of publication

This publication is being created to widely introduce the achievements of research and development activities conducted by Nikon Corporation. This is a result of R&D based on Nikon's core technologies of "opto-electronics" and "precision" technologies that have been incorporated in new products and/or often valued by external organizations such as academic societies.

Foreword

Representative Director
President

Toshikazu Umatate

Due to the ongoing COVID-19 pandemic as well as the instability of international affairs, we are facing a variety of challenges. Even in such a situation, we hope to support our customers in creating innovation by understanding the essence of what they want and finding solutions together.

In April 2022, we announced our Medium-Term Management Plan which further aims towards "Trustworthiness and Creativity." We set our Vision 2030 to become "a key technology solutions company in a global society where humans and machines co-create seamlessly." To achieve this, not only by means of our main businesses in imaging and precision equipment, but also through our strategic businesses in healthcare, components, and digital manufacturing, Nikon will deliver to our customers products and services optimized to meet their needs. We have defined two fields of value proposition for these businesses. "Industry," which expands possibilities for people via advanced manufacturing, and "Quality of Life," which makes lives better through advanced medical care and entertainment.

This report shares some of Nikon's technological developments such as material processing technologies that bring innovation to the world of *Monodzukuri* (manufacturing) in "Industry" and AI imaging technologies that advance medical treatment for "Quality of Life."

Executive Fellow
Division Manager
Advanced Technology
Research & Development Division

Masaaki Doi

Along with the significant ongoing global restrictions, there is an increase of uncertainties. We in technology development are required more than ever to respond flexibly and more rapidly to these situations. To provide products and services that meet the needs of our customers as quickly as possible, Nikon's research and development teams are working on diverse ideas, to develop technologies for our main businesses and the growth drivers defined in the Medium-Term Management Plan. Especially for the growth drivers, the results of continuous technological development are gradually becoming visible as achievements.

We will share the Nikon Group's research and development results for this year again through this report, which contains technological explanations of products released and announced in FY2021, and highly valued paper topics that were submitted and presented at various conferences during the same year, focusing on technology developments for the growth drivers. Although this covers only a small selection of the technological developments Nikon is working on, I hope that this report will help you to understand what we are engaged in and provide opportunities for Nikon's technology to contribute to society.

Nikon Research Report Vol.4
目次／ CONTENTS

技術解説/Technical Reports

研究開発論文/Research and Development Reports

技術解説

Technical Reports

フラッグシップフルサイズミラーレスカメラ「ニコン Z 9」の開発

尾崎浩二，斉藤義久

Development of Flagship Full-Size Mirrorless Camera with Interchangeable Lenses: Nikon Z 9

Koji OZAKI and Yoshihisa SAITO

ニコンの最先端技術を結集させ，静止画・動画ともにニコン史上最高の機能・性能を備えた「ニコン Z マウント」を採用した初のフラッグシップモデルとなるフルサイズ（ニコン FX フォーマット）ミラーレスカメラ「ニコン　Z 9」を2021年12月に発売した．ここでは，Z 9 の様々な開発要素について説明する．

In December, 2021, we launched the sales of the full-frame (Nikon FX-format) mirrorless camera Nikon Z 9. The Z 9 is the first flagship model of the Z series mirrorless cameras, combining Nikon's leading-edge technologies to deliver the best still and video features and performance in Nikon's history. Here, we explain the various development elements of the Z 9.

Key words レンズ交換式，ミラーレスカメラ
interchangeable lenses, mirrorless camera

1 Introduction

In December 2021, Nikon released its first flagship model, the Nikon Z 9, an FX-format mirrorless camera. This paper describes the various development elements of the Z 9.

Fig. 1　Nikon Z 9

2 AF and Continuous Shooting Performance

High-performance autofocus (AF) is supported by three technologies. They are Nikon's first AF calculations at the high speed of 120/s, superior subject detection developed using deep learning technology, and high-speed AF information communication unique to the Z-mount. The combination of these technologies enables high-dimensional AF tracking performance that accurately captures randomly moving subjects even during high-speed continuous shooting. Accurate AF calculations at the high speed of 120/s are achieved by the combination of high-speed readout by the new CMOS sensor and high-speed processing by EXPEED 7. Through an algorithm developed using deep learning technology, nine types of subjects can be detected: people, dogs, cats, birds, cars, motorcycles, bicycles, trains, and airplanes. The person detection function detects smaller pupils than before and can even detect them through goggles or sunglasses, or when the face is upside down. Highly accurate AF is achieved by transmitting distance information between the camera body and the lens in each frame. In addition, the CFexpress Type B high-speed writing enables continuous shooting of over 1000 frames at approximately 20 fps in JPEG FINE (L) or high-efficiency RAW setting. Combined with the AF performance, it is possible to shoot continuously for extended periods without concern for the buffer.

Fig. 2 Detectable subject images

3 Electronic Viewfinder

The Real-Live Viewfinder and Quad-VGA panel supporting a high brightness of 3000 cd/m^2 represent a major evolution from the conventional electronic viewfinder. The Real-Live Viewfinder displays all the moments that were previously lost with a conventional electronic viewfinder or with an SLR camera owing to the loss of image caused by mirror lock-up. Unlike conventional blackout-free shooting, which displays the same image to prevent the loss of viewfinder image, the actual movement of the subject is always displayed as it is. Nikon's newly developed Dual Stream technology enables the simultaneous processing of still image data for recording on a memory card and live-view data for display on the electronic viewfinder and image monitor. This has enabled processing specialized to live-view, which makes it possible for the Real-Live Viewfinder to allow the user to view every moment. The newly equipped Quad-VGA panel, which can adjust brightness up to 3000 cd/m^2, enables clear confirmation of subjects even in bright surroundings where it was previously difficult to view the details of subjects. The subject is visible even in very bright scenes, such as a midsummer beach or a sunny snowfield.

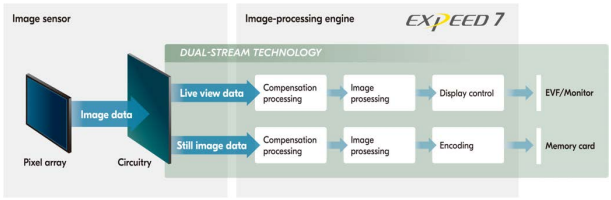

Fig. 3 Mechanism of Real-Live Viewfinder

4 Video

The heat dissipation path from the heat source to the exterior cover has been optimized, and the front and rear covers are integrated with the bottom cover to reduce parting lines and improve heat transfer efficiency, enabling the recording of approximately 125 min of 8K UHD/30p video on a memory card in the camera body without forced air cooling. Combined with an S-Line NIKKOR Z lens, which has excellent resolving power, this setup delivers a high descriptive performance to every corner of the image. Moreover, 4K UHD/120p/60p/30p is supported to meet the diverse video production needs of video creators. The Z 9 can shoot 4K UHD/120p video without screen cropping, allowing video editing with the same angle of view even if the video is shot at different frame rates. The camera supports 12-bit RAW video including over 8K/60p that exceeds high-resolution 4K UHD/60p given by 8K oversampling. Nikon's original 10-bit N-Log, Hybrid Log-Gamma (HLG), and N-RAW recording are also supported. The ProRes 422 HQ recording format is supported to meet a wide range of video production needs. In addition, the detection of nine types of subjects is supported in movie recording.

Fig. 4 Internal recording of 8K UHD/30p, 4K UHD video supported

5 High Image Quality

The Nikon Z 9 is equipped with a stacked CMOS image sensor with an effective 45.71 MP. The standard sensitivity is ISO 64 to 25600 and it can also be set to 1 EV (equivalent to ISO 32) below ISO 64 and to 2 EV (equivalent to ISO 102400) above ISO 25600. Auto ISO sensitivity control is also available. At high sensitivity, noise is processed at different

Fig. 5 Stacked Nikon FX format CMOS sensor

intensities for flat areas, such as a night sky, and for details, such as illuminated buildings, effectively reducing the rough noise that tends to occur in areas of night sky while maintaining the high resolution of fine details.

6 Design

The design of the Nikon Z 9 was the culmination of the pursuit of ease of use and high reliability as a tool for professional photographers who cannot afford mistakes when shooting. The integrated vertical grip ensures comfortable operation in both horizontal and vertical positions, and high reliability is achieved by improving the strength and rigidity of the body. The Z 9 has been designed so that professionals would find it easy to use. Several buttons with customizable settings have been added.

Menus with deep hierarchies tire professional users with repeated button presses because they take several pictures in a day. In such cases, the more buttons with a direct operation, the more the load on the photographer can be reduced. While meeting these needs, the Nikon Z 9 is approximately 20% lower in volume than the D6.

Fig. 6 Nikon Z 9, which is approximately 20% lower in volume than the D6

7 Operability and Reliability

The Z 9 is the first Nikon camera with a four-axis tilt image monitor, which provides high operability when shooting from high or low angles in either portrait or landscape mode. When shooting in the portrait mode, the still image live-view user interface automatically switches to the portrait mode, making it easy to check the display and operate the monitor. The buttons necessary for menu settings and image confirmation are illuminated, allowing operation in the dark as smoothly as in daylight. Reliability is ensured by the high scan rate, which suppresses rolling shutter distortion and eliminates the need for a mechanical shutter. This enables a large number of photos to be taken freely, without worrying about durability or the risk of malfunction, and eliminates dust from shutter wear. The optical filter in front of the image sensor is double coated, with a conductive coating to reduce dust adhesion and a fluorine coating to facilitate wiping off dust that does adhere. In addition, the Nikon Z 9 is equipped with a sensor shield that can be closed when it is turned off, preventing dust adhesion when changing lenses, and also preventing fingers from coming into contact with it. The top, front, and rear covers are made of a magnesium alloy, achieving Nikon's best-in-class robustness equivalent to that of the D6 and high dustproof and splash-proof performance. A review of the component parts reveals cold resistance that enables operation even at minus 10°C.

Fig. 7.1 Nikon's first four-axis tiltable image monitor with a high degree of angle freedom

Fig. 7.2 Body incorporating magnesium alloy

8 Summary

The Nikon Z 9 is Nikon's flagship mirrorless camera that incorporates all of Nikon's current technologies for both still and moving images, making it the perfect camera for professional photographers who demand the best performance from their cameras in any situation or place, and at any time.

We have already received considerable feedback on how the Nikon Z 9 enables the shooting of subjects that was previously impossible for the user. Nikon will continue to produce products that meet and exceed user expectations, without being satisfied with the status quo.

尾崎浩二　Koji OZAKI
映像事業部 開発統括部 設計部
Designing Department
Development Sector
Imaging Business Unit

斉藤義久　Yoshihisa SAITO
映像事業部 開発統括部 設計部
Designing Department
Development Sector
Imaging Business Unit

光加工機 Lasermeister1000SE/1000S の開発

江上茂樹

Development of the Lasermeister1000SE/1000S Optical Processing Machine

Shigeki EGAMI

光加工機はニコンの半導体露光装置の技術を応用して開発された加工機であり，2021年 9 月に初の光除去加工機である「Lasermeister1000S」をリリースした．Lasermeister1000S の座標系は高精度・広範囲に管理されており，加工データを忠実に再現することができる．光源には超短パルスレーザーを採用しており，あらゆる材料に対して非熱のレーザーアブレーション加工を実現できる．さらに，機上には3D 光計測機を搭載しているため，計測結果を精確にフィードバック加工することが可能である．加工パスは CAD データ，加工パラメーター，対象物の3D 計測結果から自動生成されるため，作業者のスキルに依存せずにサブマイクロメートルの高精度加工も実現できる．本稿では，これらの Lasermeister1000S の開発要素と，アプリケーションとして考えているきさげ，精密金型，セラミックス材料の加工事例を解説する．

An optical processing machine has been developed by applying Nikon's semiconductor lithography technology. The first optical subtractive processing machine, "Lasermeister1000S," was released in September 2021. The coordinate system of the Lasermeister1000S is adjustable with high accuracy over a wide range. Therefore, model data can be accurately reproduced with high fidelity in processing. An ultra-short pulse laser is used as the light source, with which non-thermal laser ablation processing can be applied to almost all materials. Furthermore, because a high-precision three-dimensional (3D) optical measuring device is mounted on-machine, accurate feedback of the measurement results to the laser processing for improved process quality is realized. The machining path is automatically generated from computer-aided design (CAD) data, processing parameters, and 3D measurement results of the object; hence, sub-micrometer processing accuracy can be achieved without relying on the operator's skill. In this paper, the development of the aforementioned elements is explained and processing examples with scraping, precision molding and processing on ceramic material are discussed, which are areas of application for this optical processing machine.

Key words 光加工機，超短パルスレーザー，レーザーアブレーション，機上3D 計測
optical processing machine, ultra-short pulse laser, laser ablation, on-machine 3D measurement

1 Introduction

As the first optical processing machine, the metal 3D printer "Lasermeister100A" was developed in April 2019 by applying the semiconductor lithography technology that Nikon has built up over the years. This optical processing machine, which can realize high-precision metal additive manufacturing at low cost and footprint, has wide applicability to market needs. A model with enhanced functions, such as five-axis machining, was also released in 2020, with titanium alloy support further added in 2021.

Nikon's optical processing machines are not limited to the additive manufacturing processing of this metal 3D printer "+ (plus)," but have also been advancing product development of subtractive processing of "– (minus)." The subtractive optical processing machine can realize high-precision surface-shape processing by repeating 3D precision measurements with an on-machine optical measuring device and

Fig. 1 High-precision surface-shape processing machine: Lasermeister1000S.

non-thermal/non-contact processing together with an ultra-short pulse laser. This high-precision surface-shape processing machine was released in September 2021 as "Lasermeister1000SE" and "Lasermeister1000S" (hereafter collectively referred to as "Lasermeister1000S") (Fig. 1).

2 Concept of Lasermeister1000S

The Lasermeister1000S is a new processing machine that achieves high-precision surface-shape processing and microfabrication based on the concept of "remake manufacturing." This processing machine can simplify or automate the processing setup such as computer-aided manufacturing (CAM), conditions setting, chucking, or reference surface setting. These processes, typical in conventional processing machines, enable the realization of machining that was difficult owing to the wear of cutting tools and constraints of the target object in terms of, for instance, material, shape, and rigidity, with a micro-to-submicrometer precision and requiring no additional operator skill.

"Lasermeister1000SE" constitutes an entry model equipped with an ultra-short pulse laser and a processing/measurement system that uses an on-machine non-contact 3D optical measurement to realize high-precision subtractive processing. In addition to this basic performance, the standard model "Lasermeister1000S" is equipped with more precise positioning mechanism and coordinate correction system, and it is capable of accurate surface-shape finishing and microfabrication over a wide range. This article describes the features and applications of Lasermeister1000S.

3 Features of Lasermeister1000S

The features of the Lasermeister1000S with emphasis on its newly developed elements are introduced below.

3.1. Highly Precise and Widely Managed Global Coordinates

The processing machine must construct and manage an accurate coordinate system to reproduce with fidelity computer-aided design (CAD) data (Fig. 2). The coordinate system of a general-purpose processing machine is not always constructed accurately, in particular over wide range, due to insufficient operator skill and unsuitable setup. However, the coordinate system of Lasermeister1000S includes advanced correction systems (tilt, scaling, orthogonality, etc.) developed by using Nikon's semiconductor lithography equipment technology that can construct an accurate global coordinate system regardless of operator skill (Fig. 3). Conventional high-precision processing machines require significant effort to suppress drift caused by environmental temperature fluctuations, but the Lasermeister1000S can correct and manage the highly corrected coordinate system. In addition, this processing machine utilizes an air bearing based work stage, as the optical measurement and processing techniques renders mechanical contact unnecessary. Friction-less sliding of the air bearings installed on the stage against the surface plate finished with a high flatness ensures high running reproducibility throughout the stroke without the vibration or loss of precision that may be caused by mechanical driveshafts.

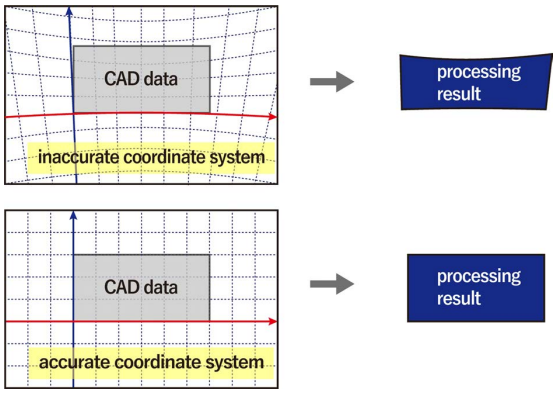

Fig. 2 Effect of coordinate system on processing.

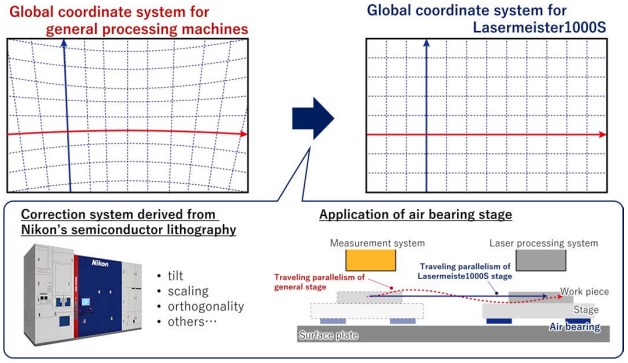

Fig. 3 Lasermeister1000S's global coordinate system.

3.2. Processing for a Wide Range of Shapes and Materials by Ultra-short Pulse Laser Ablation

Laser ablation is a phenomenon in which the surface of an object is explosively scattered and evaporated by irradiation of a high-intensity pulsed laser. Ablation processing using an ultra-short pulse laser (ranging from femtoseconds to several picoseconds) of pulse width shorter than the time required for heat conduction can remove the material without converting the laser energy into heat. Consequently, processing can be performed without causing thermal deformation or including a heat-affected zone (HAZ) of the target object

(Fig. 4), as opposed to CW laser and nanosecond laser processing. In addition, given that laser processing is non-contact and enables processing with almost zero reaction force, a chuck is unnecessary. Therefore, high-precision processing can be realized on the work pieces of thin plates and low-rigidity parts without causing deformation due to that might otherwise be caused chucking and machining force, which is a problem in conventional processing machines.

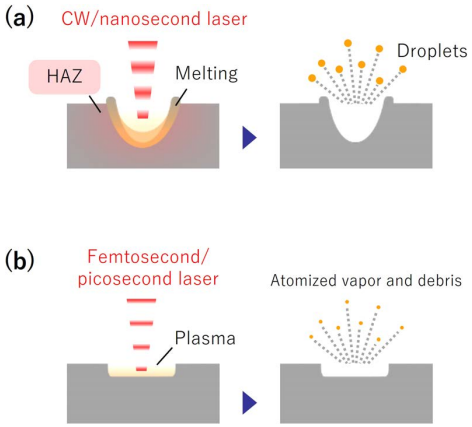

Fig. 4 Differences in processing as a function of laser pulse width: (a) Thermal processing with CW/nanosecond laser; (b) non-thermal processing with femtosecond/picosecond laser.

An additional advantage of ablation processing by ultra-short pulse laser is that there are few constraints on the materials that can be processed. Ultra-short pulse lasers can process even materials having band gaps larger than the photon energy (i.e., materials that do not absorb light) due to non-linear photon behavior at extremely short pulses. The ultra-short pulse laser adopted in Lasermeister1000S enables processing of general metals and a wide range of materials such as those that are hard and difficult-to-process, e.g., cemented carbides and diamond, and also easy-to-break brittle materials, e.g., ceramics and optical glass (Table 1).

In conclusion, laser ablation using an ultra-short pulse laser can minimize adverse effects on the work piece and is effective for machining of a wide range of shapes and materials.

Table 1 Materials that can be processed with the Lasermeister1000S.

Typical metals	Highly reflective metals	Difficult-to-cut metals	Ceramics/ Semiconductors/ Sintered materials	Others
Austenitic stainless steel	Aluminum	Die steel	Silicon	Borosilicate crown glass
Martensitic stainless steel			Silicon carbide	
Ferritic stainless steel	Copper	Tungsten	Silicon nitride	Fused silica glass
Carbon steel		Titanium	Aluminum nitride	
Chromium molybdenum steel	Gold		Alumina	Single crystal diamond
Zinc		Titanium alloy	Zirconia	
Aluminum alloy	Platinum	Nickel alloy	Cemented carbide	Polycrystalline Diamond
Cupper alloy				

Processing accuracy and safety depend on materials. Processing of materials other than the above is also possible.

3.3. On-machine Feedback Processing by On-machine 3D Measurement

The on-machine 3D measurement equipment installed in Lasermeister1000S employs optical interference technology, which enables high-precision and high-throughput 3D measurement. By measuring the surface shape of the target object with high accuracy, it is possible to accurately enable machining feedback according to the target shape. As a result, it is possible to obtain the desired high-precision surface easily by repeating the machining feedback using this high-precision measurement (Fig. 5).

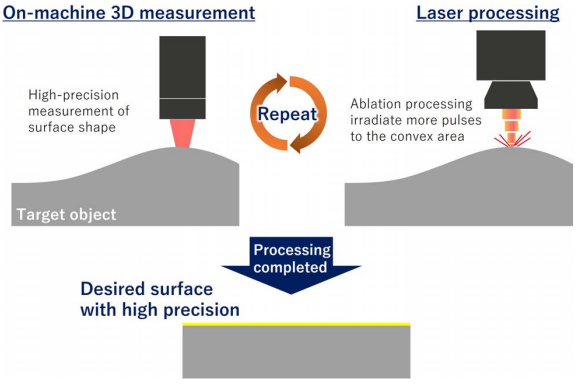

Fig. 5 On-machine feedback processing by on-machine 3D measurement.

Figure 6 shows a typical example of common flat surface processing (processing to achieve uniform flatness over multiple locations) using on-machine feedback machining. The work piece was a thin plate of stainless steel: SUS304 (80 mm x 75 mm x 1 mm thick), and common flat surface processing of 10 mm x 10 mm was performed on these four corners. This stainless steel thin plate exhibited a swell of approximately 100 um before processing. However, as can be seen from the color contour diagram, the targeted area was processed to have a very high precision common flatness (0.4 um) with submicrometer geometric tolerance. It is difficult to realize such ultra-high precision processing of thin

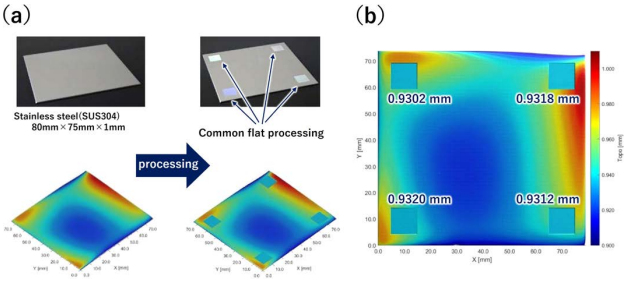

Fig. 6 Common flat surface processing of SUS304 thin plate: (a) Photograph of the target object before and after machining and diagonal contour diagram of height; (b) planar contour diagram after machining; common flatness of 0.4 um was achieved.

plates with grinding machines, but the Lasermeister1000S can readily achieve this without chucking and particular operator skill.

3.4. Automatic Generation of Machining Data by On-machine CAM/3D Alignment

For typical NC machine tools, it is necessary to create a machining program with CAM based on a design model created with CAD. CAM improves the work efficiency of the process and can handle complicated machining shapes and perform machining simulations. However, it requires specialized knowledge in programming, and the time required for creation and data quality varies depending on the operator's skill.

Lasermeister1000S incorporates CAM-equivalent functionality (on-machine CAM) into the device software (Fig. 7). Only the 3D models of the work piece and the machining target design, together with the machining and measurement parameters, are input into the device. As the machining area and machining path are automatically generated from these model data, parameters, and on-machine 3D measurement results, the operator's specialized knowledge is no longer required, leading to shortened program creation times and stabilized data quality.

Elimination of setup by a "3D alignment" procedure that automatically positions the target object is also a prominent feature of the Lasermeister1000S. In conventional processing machines, the operator fixes the work piece with a jig and performs position measurements involving contact of the measurement stylus at multiple sample points; however, it is typically an extremely complicated procedure. With the Lasermeister1000S having on-machine measurement capability, such procedures can be automatically performed.

Figure 8 shows the process of 3D alignment. First, the work piece is placed at any arbitrary position on the table. Lasermeister1000S is equipped with two types of 3D mea-

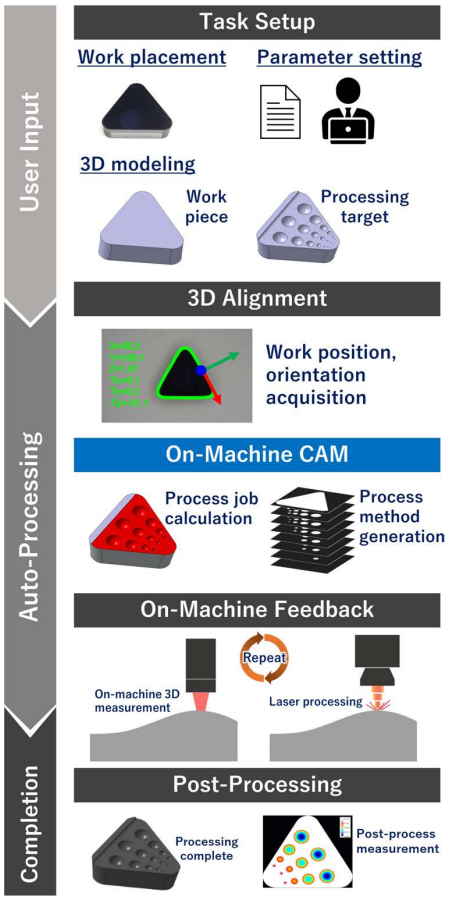

Fig. 7 Processing flow of the Lasermeister1000S.

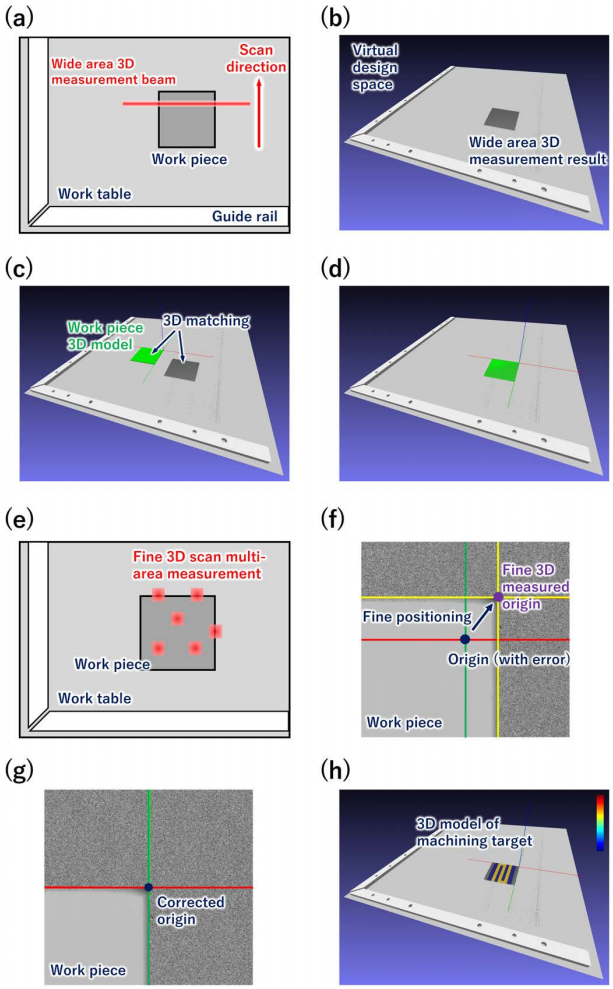

Fig. 8 3D alignment process: (a) Work piece measurement with wide-area 3D scanner; (b) placement of wide-area 3D scanner measurement results in virtual space; (c) 3D matching of base-material 3D model and measurement results; (d) 3D matching results; (e) measurement of edge position and height of the work piece at multiple areas with a fine 3D scanner; (f) fine positioning of the work piece origin based on the measurement results of the fine 3D scanner; (g) fine positioning results; (h) placement of 3D model of machining target in virtual space.

suring machines: a wide-area 3D scanner implementing an optical cutting method and a fine 3D scanner implementing an optical interference method. Next, the wide-area 3D scanner measures the entire image of the work piece in a short time, and 3D matching is performed with the 3D model input into the system. From the result of this matching, the work piece's position and orientation can be automatically aligned, and the actual position and orientation of the work piece can be reproduced in a virtual space on the computer. However, 3D alignment with a wide-area 3D scanner has an error of several hundreds of micrometers; thus, when more precise alignment is required, it is performed with the fine 3D scanner. With reference to the results of the wide-area 3D scanner, by then accurately measuring the edge position and height of the work piece at multiple areas with the fine 3D scanner, it is possible to finely position the model and orientation of the work piece in the processing space with micrometer precision. The 3D model of the machining target is placed in a virtual space based on the actual position and orientation of the work piece on the work table, and then machining can be accurately performed according to the input machining parameters.

4 Applications

Lasermeister1000S, which integrates the above-mentioned technologies, can easily realize high value-added processing with micro-to-submicrometer geometric tolerances for various applications. Examples of applications include precision molding, precision surface, cutting tools, grinding wheels, low rigidity parts, difficult-to-cut materials processing (ceramics, diamonds, carbide, optical glass, etc.), and microfabrication. Here we will introduce some of them.

4.1. Reproduction Processing of Scraping

Scraping is used in sliding parts of machine tools, such as grinding machines, and as reference flats. It is an important technique indispensable for machine tools. Scraping, which results in an ultra-flat finish that cannot be achieved with conventional processing machines, still requires a traditional processing technique where a craftsman hand-scrapes a surface to induce shallow depressions while maintaining the original flat surface. Oil will readily adhere to this scraped surface, creating an oil sump of several microns, allowing smooth movement when used as a sliding surface. Figure 9 shows the processing that digitally reproduced this scraping.

Gray cast iron (FC300) was prepared as the base material, and the hand-scraping result was reproduced in the center of the work piece with dimensions 60 x 60 mm (laser processing time: 35 min). Figures 9 (a) – (c) show a photograph after processing, the height contour diagram, and the profile, respectively. As can be seen from the profile results in Fig. 9 (c), the shape after processing was faithfully reproduced in submicrometer scale with respect to the target shape, realizing the automation of scraping that typically requires more than a decade of skill mastery. An evaluation of the sliding characteristics was also conducted in another case, and results comparable to hand-scraping made by a craftsman were obtained. Note that it is easy to pattern the oil sump with arbitrary shape and regularity, making it possible to eliminate the quality variation introduced by different operators. Thus, we demonstrated that this processing machine is a powerful tool for realizing digital manufacturing of scraping.

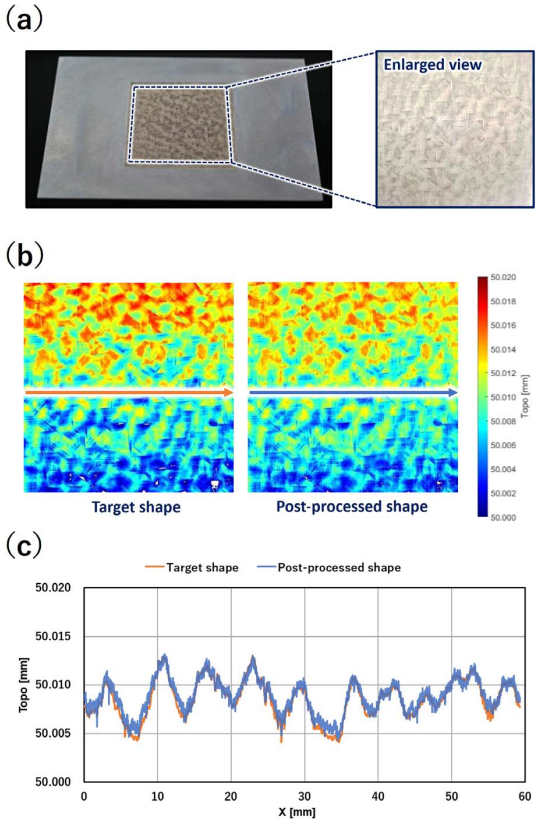

Fig. 9 Reproduction processing of scraping: (a) Photograph of processed scraper; (b) contour diagram of heights of machining target and post-processed shape; and (c) corresponding shape profiles.

4.2. Mold Processing of Fuel-cell Separator

Fuel-cell separators are manufactured by press molding, but materials with high hardness and abrasion resistance, such as die steel, high-speed tool steel, and cemented carbide, are used as mold materials. Consequently, it is difficult to realize high-precision machining of the molds with con-

ventional processing machines. In addition, the machining shape of the separator mold is complicated, and the processing difficulty is also high. The separator has a flow path through which gas flows, and to promote gas diffusion, an irregularly shaped flow path may be needed. As the separator is used for stacking, high flatness is also required. Figure 10 shows a processing example model of a hypothetical separator mold.

PD613 (Daido Steel Co., Ltd.), which is a die steel, was used as the base material for this processing objective. In the flow path of the 3D model of the machining target, aperture and taper were included, and a structure with a high degree of freedom was machined for this mold material (laser processing time: 3.3 h). The flow path model has a 45-degree taper, and the processing in Fig. 10 results show that it can be reproduced precisely. The surface shape could be processed with extremely high precision: the average difference between the shape after processing and the target shape to be processed was 1.3 um. The surface roughness was Ra 0.15 um at the deepest point. It was confirmed in another example that similar processing can be carried out even with cemented carbide. Thus, these processes demonstrate the processing of separator molds for fuel cells, which is one of the applications of precision molding.

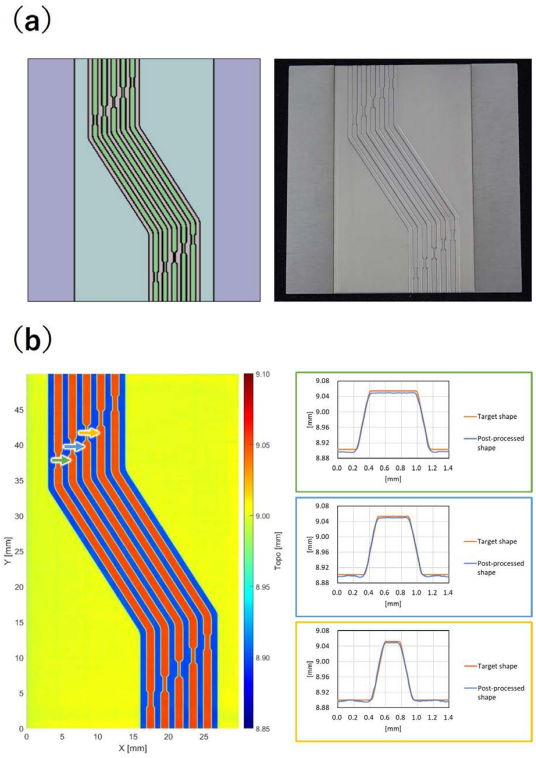

Fig. 10 Processing example of a model of a hypothetical fuel-cell separator mold: (a) 3D model of processing target and work piece after processing; (b) height contour diagram of shape after processing and cross-sectional profile of flow path through the aperture.

4.3. Fine Shape Processing of Ceramic Materials

Ceramic materials such as alumina have excellent mechanical strength, wear resistance, and electrical insulation properties and are used as structural materials for electrostatic and vacuum chucks that hold silicon wafers on a flat surface with high accuracy. Tens of thousands of fine pin shapes with a diameter of hundreds of micrometers and a height of tens of micrometers are formed on the surface of these chuck parts to suppress trash traps; but these parts demand high productivity and must be processed in a short time. Blasting is usually employed for this pin formation as it can accomplish surface grinding, satin processing, and surface modification, even in places where machine tools do not reach. However, the setup of the masking and mask peeling process is complicated and difficult to automate. The degree of freedom of the processing shape is also complicated to manage and there are many restrictions. In this context, we introduce an example of ceramics processing by Lasermeister1000S.

Figure 11 shows the results of conducting grooving, common flat surface processing, and fine pins processing on an alumina substrate. Grooving is a machining procedure that assumes a groove for the gas flow path of an air bearing or electrostatic chuck. It can be seen that a target machining depth of 20 um can be achieved in each groove with a machining accuracy of ± 1 um or better (Fig. 11 (b)). Similar to the stainless steel machining example, common flat surface processing could achieve a flatness of 0.4 um even for alumina (Fig. 11 (c)). Pin pattern machining was successful with models of diameters 250 um and 500 um by imagining electrostatic and vacuum chucks. The height of

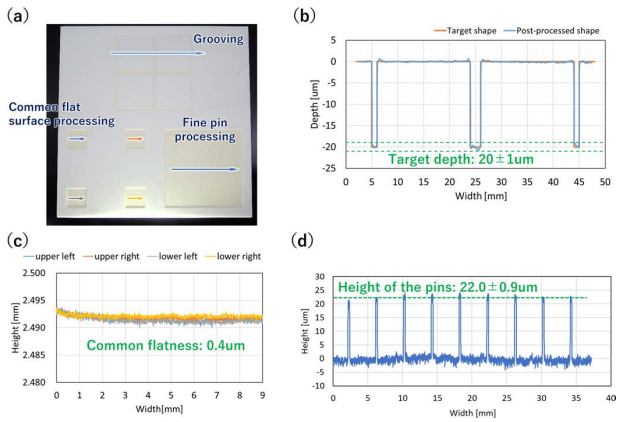

Fig. 11 Fine shape processing on alumina substrate: (a) Photograph of alumina substrate with after fine-shape processed; (b)-(d) cross-sectional profile of grooving, common flat surface processing, and fine pin processing, respectively.

the pins of diameter 250 um was 22.0 ± 0.9 um, highlighting suppression of variation among pins (Fig. 11 (d)). Given that the machining accuracy of chuck parts affects the distortion when gripping the flat surface of the wafer and the temperature controllability for keeping the wafer temperature constant, it is a requirement to process the pin height and groove depth uniformly. Lasermeister1000S controls these parameters on a micro-to-submicrometer scale.

5 Conclusions

Lasermeister1000S is a novel processing machine that has a dramatic effect on the design of machining tasks, reduces the waste of “processes that were common so far”, and realizes “processing that was impossible so far.” Being able to easily process a wide variety of machine parts with light will revolutionize manufacturing. Therefore, we will introduce machining support tools, such as automatic processing condition setting and processing unevenness correction, and advance the development of elements such as five-axis stage/laser re-melt to enable the development of more valuable next-generation optical processing machines for users in the future.

江上茂樹　Shigeki EGAMI
次世代プロジェクト本部 第一開発部
1st Development Department
Next Generation Project Division

江上茂樹
Shigeki EGAMI

LiB 検査市場に貢献するニコンの X-Ray CT 技術

坂口直史，David Bate，Jan De Geeter，Jos Jans，Ben Morgan

Nikon's X-Ray CT Technology that Contributes to the LiB Inspection Market

Naoshi SAKAGUCHI, David BATE, Jan DE GEETER, Jos JANS and Ben MORGAN

電気自動車の急速な普及に伴い，バッテリーセルの適切な検査は，バッテリーセルの長期的な性能と安全性を保証するために重要な要素となる．

本稿では，この市場ニーズに応えるニコンの新しい XT H 225 ST 2x X 線コンピューター断層撮影（CT）システムと，システムに搭載する新機能を紹介する．

最初に，X 線の生成とイメージングの原理，および従来の CT 取得と再構成の手法について説明する．続いて新機能とアプリケーションの紹介を行う．

改良された Rotating.Target2.0により，従来の静的反射ターゲットと比較して，特定の焦点スポットサイズに対して 3 倍の高出力 X 線を得る．独自の Half.TurnCT 取得および再構成アルゴリズムにより，より高速なスキャンが可能になり，X.Tend ヘリカル CT は，高解像度でアーチファクトのないデータを提供する．Auto.FilamentControl はフィラメントの寿命を 2 倍にする．これらすべての新しい2x の機能は，生産環境でのエンドオブラインテストおよびプロセス制御に X 線 CT を使用するための重要な要件である高速で高品質の CT スキャンを可能にする．

最後に産業用アプリケーションの実例として，リチウムイオン電池セルの高速検査のための XT H 225ST2x システムの使用例について紹介する．

With the rapid adoption of Electrical Vehicles, proper inspection of battery cells is critical to guarantee their long term performance and safety. This paper introduces Nikon's new XT H 225 ST 2x X-ray Computed Tomography (CT) system as well as the new features that come with the system to meet this market need. First the principles of X-ray generation and imaging are explained as well as the traditional CT acquisition and reconstruction techniques. Next, we will introduce new features and applications. The improved Rotating.Target 2.0 makes it possible have a 3 times higher X-ray flux for a given focal spot size compared to a traditional static reflection target. The unique Half.Turn CT acquisition and reconstruction algorithms enables faster scans while X.Tend helical CT provides high-resolution, artefact free data. Auto. Filament Control doubles the lifetime of the filament. All these new 2x features enable fast and high quality CT scans that are a key requirement for the usage of X-ray CT for end-of-line testing and process control in a production environment. Finally, as an example of such an industrial application, the paper discusses the usage of the XT H 225 ST 2x system for fast inspection of Li-Ion battery cells.

Key words X 線，コンピュータートモグラフィー，リチウムイオンバッテリー，検査，生産
X-ray, Computed Tomography, Lithium-ion battery, inspection, production

1 Introduction

Nikon offers a wide range of industry-leading X-ray and Computed Tomography (CT) systems to do non-destructive inspection of parts as small as MEMS up to large castings and this for a wide range of industries including aerospace, automotive, consumer products, electronics and much more. At the heart of these systems are Nikon's X-ray microfocus sources, ranging from 130 kV through to 450 kV, that Nikon X-Tek Systems in Tring (UK) has been developing and manufacturing in-house since 1986. Unique X-ray source technology such as rotating target, integrated generator and the worlds-only 450 kV microfocus source allow superior image quality across the entire range of systems.

In the early days, X-ray CT was mainly used in Research & Development (R&D) and Failure Analysis. More recently, production quality control teams have seen the benefit of using CT to shorten production set-up time by doing detailed first article inspection and to improve process control by doing systematic end-of-line inspection. In both cases,

a single CT scan enables inspection of internal and external dimensions and reveals defects and assembly issues, all in a non-destructive way and faster than other technologies. The latest trend is to move CT inspection into the production line to catch issues as early as possible. This trend can certainly be seen in the growing market of Li-Ion battery cells that power hybrid and electrical vehicles. Manufacturing quality in this case is important to guarantee long term battery performance and safety.

In the production line, the challenge is to reduce inspection cycle times as much as possible without compromising on data quality. The remainder of the paper will explain how Nikon has responded to this challenge by further improving source performance and implementing innovative CT scanning techniques and reconstruction algorithms which resulted in the new XT H 225 ST 2x X-ray CT system.

2 Technology Background

2.1. Principle of X-ray Imaging

X-rays are a form of electromagnetic radiation, just like visible light, but compared to many other types of radiation, X-rays are more energetic. An X-ray photon can be hundreds or thousands of times more energetic than a photon of visible light, see Fig. 1.

Wilhelm Roentgen first described X-rays in 1895, an achievement for which he was awarded the very first Nobel Prize in Physics. During World War I, X-rays were already being used for medical purposes.

Most of the X-rays in the universe arise when highly excited atoms decay back to their ground state configuration. For example, if an electron is removed from the inner shell orbitals of an atom — perhaps by a collision with something — then the atom will emit an X-ray photon as it returns to its equilibrium state.

Another common source of X-rays is from a process called "bremsstrahlung", which is German for "braking radiation." X-rays are emitted when a highly energetic beam of charged particles such as electrons is rapidly decelerated — because it runs into a metal target, for example.

In medical and industrial X-ray sources, a beam of energetic electrons is focused onto a target, usually a piece of Tungsten. As the electrons are decelerated, this generates bremsstrahlung X-rays. In addition, the incoming electrons can collide with a Tungsten atom and knock an electron out from its inner orbit. This kind of device actually produces X-rays by both mechanisms simultaneously.

The high energy of the X-rays combined with their interactions with the electron cloud in the atoms means that X-rays can penetrate significant amounts of material; the exact length depends on density and atomic number and broadly falls off as either increases. The X-rays that pass through the material (as well as those scattered) can then be detected. Originally this was done using film but over the years a number of electronic means have become available.

Today the most common type of detector in industrial X-ray is the flat panel detector, that consists of a scintillator material (most often Caesium Iodide (CI) or Gadolinium Oxysulphide (GadOx)) that converts the incident X-rays into light. These scintillators sit on top of a layer of photo diodes which convert the light generated into a 2D image which is read out to a computer.

The key equation in X-ray image formation is the Beer Lambert law which describes how the intensity of the detected X-rays falls off with the thickness of material:

$$I = I_0 e^{-\mu t} \quad (1)$$

The equation (1) is true for a monochromatic beam traversing a uniform material with attenuation coefficient μ, the equation can be extended to polychromatic beams as found in typical microfocus sources and to multiple materials.

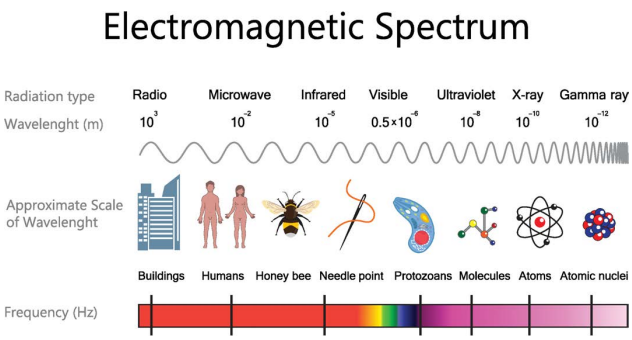

Fig. 1 Overview of the Electromagnetic spectrum showing the place of X-rays within it.

When an image is collected the values of I_0 and I can be measured before and after the sample is introduced. This in turn will allow calculation of the attenuation along that path, this will be important later when we discuss Computed Tomography.

2.2. Features of Microfocus X-ray Sources

There are several different types of X-ray sources. Of most use in industry are the Mini-focus tube (X-ray focal spot size > 100 microns) and the Microfocus tube (focal spot size < 100 microns, typically < 10 micron at best). Within each type there are two competing construction methods: sealed tube in which the source is put under

vacuum and then sealed and runs in a sealed state until failure, when it is replaced. Next to this, there is or the open tube, in which the source can be vented to air and the filament or other failed parts replaced, giving it an unlimited lifetime.

The customer will choose the type that best matches their sample and imaging needs.

A typical Microfocus tube will consist of the following elements, see Fig. 2.

1) A high voltage receptacle to allow the high voltage (typically around 200 kV) to be delivered
2) An electron source, often a heated Tungsten hairpin
3) A cathode/anode assembly causing electrons to be extracted from the filament and accelerated
4) A drift space with steering coils to make sure the beam passes through the centre of the lens
5) An electromagnetic lens to focus the beam
6) A metallic target of a suitable material to generate X-rays (typically Tungsten).

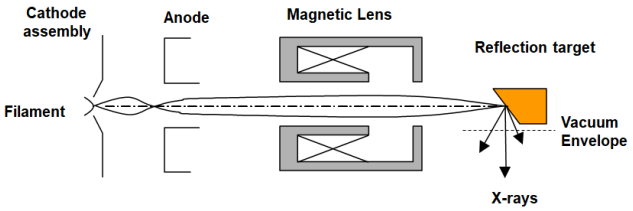

Fig. 2 Outline of a microfocus source.

The biggest remaining variation is on the type of target used, there are two axes:

a) Stationary or Rotating

A stationary target is fixed in place; it has the advantage that with no moving parts it can give a stable source. The rotating target allows a much higher power density (electrons per unit area) which leads to a much higher X-ray flux for a given spot size.

b) Reflection or Transmission

A reflection target sends the beam of electrons into a large block of the target material and the X-rays used are those that come back out of the target (i.e. are 'reflected' back), it is easier to cool but allows the electrons to spread in the target so limits the X-ray source size. A transmission target is a thin film where the electrons hit one side and the X-rays are taken off the other side (i.e. they are 'transmitted'). This enables a smaller spot to be achieved but is harder to cool so can only be used at lower powers.

2.3. Introduction to Computed Tomography and Reconstruction Algorithms

By combining 2D radiographs from an object taken from different directions, a 3D representation of the object can be created. The most commonly used Computed Tomography algorithm is Circular FDK CT.

In this mode individual images (call projections) are taken while the object rotates 360 degrees in the X-ray beams, see Fig. 3. By application of the Radon transform to the attenuation found from the images the data can be back projected into the 3D volume of the sample.

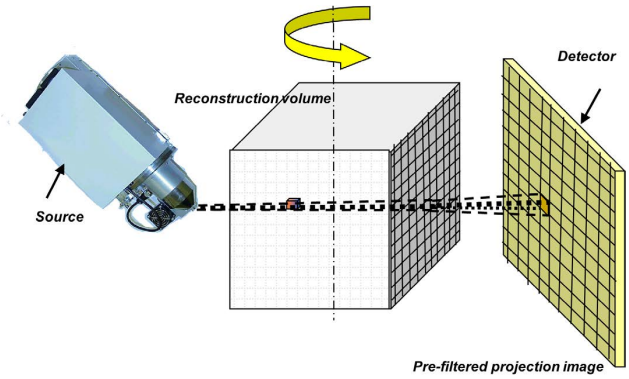

Fig. 3 Schematic of CT data acquisition.

It was found that if the attenuation was simply back projected then the resulting image was blurred and so a filtering step was introduced to form Filtered Back Projection, the most commonly used algorithm for this is the FDK algorithm from Feldkamp et al [1].

The FDK algorithm is imperfect and can lead to errors in the final volume Below is a short list of the most common errors:

1) Off axis errors – the algorithm is only fully correct on the central horizontal slice that passes through the focal spot of the source. As the angle to the object increases there is a loss of information and this introduces off axis errors, usually a blurring or drop in SNR.
2) Field of view – the algorithm relies on the whole object being contained with the cone subtended by the detector. If parts of the object are outside this cone then errors will occur; usually this introduces a bright ring.
3) Beam hardening – as the X-ray beam is polychromatic and the Beer Lambert law is monochromatic there is a mismatch. This is made worse as attenuation changes with kV but only the integrated intensity is measured, which leads to a non-linear value of the attenuation. There are extensions of FDK that allow for correction of this effect for single and multiple materials.

3 New XT H 225 ST 2x features

3.1. Introduction of the XT H 225 ST 2x System

The XT H 225 ST 2x standard system is equipped with a 225 kV source with Rotating.Target 2.0 with a focal spot size of 10 µm < 30 W and a maximum focal spot size of 160 µm at 450 W. The 8.3 MP flat panel has a pixel size of 150 µm. Fig. 4 is a system picture.

Fig. 4 Picture of the XT H 225 ST 2x system.

3.2. Improved Rotating.Target 2.0

One ongoing issue with all X-ray CT is that the image quality of the result is directly related to the amount of X-ray flux collected. This means that for a given flux a longer scan will have better image quality than a shorter scan.

In order to improve the quality of short scans the 2x system incorporates a Rotating.Target 2.0. Such a target consists of a rotating disc with a sloped surface and Tungsten coating. As 99% of the power of the electrons hitting the target is converted into heat and only 1% into X-rays, focusing the electron beam on a very small area of the target will melt the target. With the rotating target, this focal spot is not a single spot but a much larger circular area that can be cooled much more efficiently through a combination of water cooling and radiative cooling. This approach allows a much higher electron power density on the target. This can then be used to either have a much higher flux at the same spot size or a much smaller spot size at a given flux. For the 2x the main use is the former, where the X-ray flux can be increased by a factor of about 3x from the static reflection target, this can then shorten the time taken for a given quality by the same factor.

3.3. Auto.Filament Control Doubles the Life of Filaments

High-resolution microfocus X-rays start with electrons emitted from a thin filament that has to be replaced periodically due to wear. Less frequent changing of the filament is desirable, as it means that system availability is higher. Long-life filaments are available but they are thicker, so the high resolution nature of the microfocus X-rays is lost. With the XT H 225 ST 2x, the user no longer has to choose between high-resolution and long-life filaments. Auto.Filament Control intelligently controls the X-ray source to double the lifetime of the filament and increase system availability.

Auto.Filament Control carefully controls the current through the filament to optimize its lifetime. The current through the filament causes the filament to warm up, which allows electrons to be emitted which are then accelerated and focused on the X-ray target to generate X-rays. Increasing the current through the filament will increase the temperature and the amounts of electrons produced, up to a point where this saturates, and further increasing the current will not significantly increase the amounts of electrons emitted This function has the general shape of a logistic function, or S-shaped function. The challenge is to determine at every point in time, and for every combination of desired beam current and energy *(µA, kV)* where this saturation point or "knee" point is. Whilst this needed to be identified by an operator before, this is now fully automated in the XT H 225 ST 2x. After the installation of a new filament, with one click of a button, the system automatically identifies this knee point in the filament demand curve for every combination of beam current and energy *(µA, kV)*, see Fig. 5.

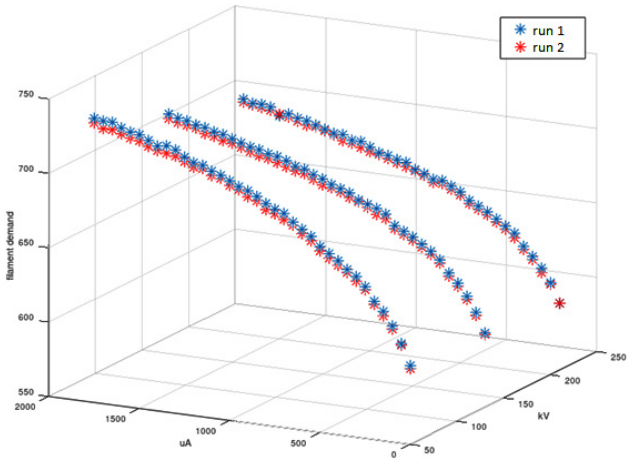

Fig. 5 Identified filament demand map, showing the knee point in the filament demand curve (arbitrary units from high-voltage generator) as a function of desired beam current (µA) and energy (kV). This graph shows two repeated runs with several days in between, showing that the identified values are stable and repeatable.

Experiments have shown that the map shown in Fig. 5 is stable over time. However, as the filament starts to wear, and

other parameters in the source vary slightly, the map becomes slightly offset, but the shape remains the same. Therefore, the XT H 225 ST 2x periodically identifies this offset without further operator intervention, achieving the optimal lifetime of the filament all the way to the end when it will finally break. This way, this new Auto.Filamant Control function has proven to extend the lifetime of filaments by a factor of 2 compared to filaments that are manually tuned.

3.4. X.Tend, Error-Free Helical CT Reconstruction

In the above discussion of FDK one of the errors was that the equations were only accurate on the central plane. Helical CT was devised to address this weakness. There are a number of different helical algorithms but they all work on the same basic principle. By moving the sample vertically as the sample rotates the angles at which the object is seen vary continuously changing the volume of correct slices.

Many helical algorithms work to smear out the errors over the whole volume, however, there are a few algorithms that are exact, one of which is the Katsevich algorithm [2], [3], [4] which Nikon uses for its helical CT reconstruction, this uses a smaller region of the detector during the scan combined with an algorithm to arrive at an accurate reconstruction which does not contain any errors due to the reconstruction process.

Another benefit of helical CT is that for taller samples, the whole part does not need to be in the field-of-view of the flat panel. In practice this means that the part can be brought closer to the source and can be scanned at higher magnification, see Fig. 6.

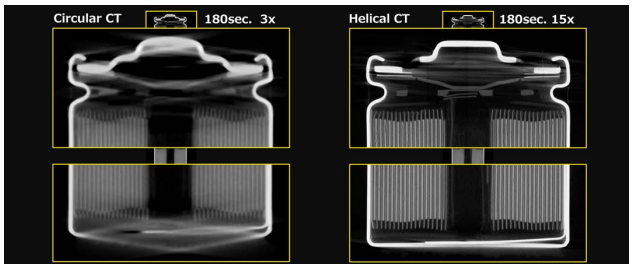

Fig. 6 Cylindrical battery cell on the left scanned with circular CT at 3 times magnification and scanned on the right hand side with X.Tend helical CT at 15 times magnification.

3.5. Half.Turn CT Doubling the Speed of the Acquisition

The new XT H 225 ST 2x system doubles the speed of the acquisition compared to a similar acquisition on the XT H 225 ST, without giving in on data quality. This is achieved by a more sensitive detector, in combination with the new Half. Turn CT acquisition and reconstruction software.

The duration of a CT acquisition is shown as (2)

$$T_a = \frac{\Delta\theta * R_\theta}{F} \tag{2}$$

where T_a is the time of the acquisition in (sec), $\Delta\theta$ is the angular range of the scan (rad), R_θ is the desired angular resolution (frames/rad) and F is the frame rate of the detector (frames/sec).

R_θ is usually optimized based on the resolution of the detector, such that $\frac{r}{R_\theta}$ is more or less equal to the pixel size of the imager, where r is the radius of the object begin scanned. Reducing R_θ will reduce the resolution of the reconstructed volume, and will increase motion blur, which is undesirable.

F is limited by the maximum frame rate of the detector, and its sensitivity. The Varex XRD4343CT panel is more sensitive than the Varex PE1621EHS used before. Running the XRD4343CT detector at 15 frames per second gives a similar quality image as the PE1621EHS detector at 11 frames per second. Further increasing the frame rate is not possible, as 15 frames per second is the maximum speed of the detector in full frame mode.

Therefore, if we want to double the speed of the acquisition without compromising the resolution while the imager is already at full frame rate, then the only remaining parameter we can play with is $\Delta\theta$, the angular range of the scan. For regular CT scans, $\Delta\theta$ is $2^*\pi$ or a full turn. However, is that really needed? In case we have a system with a parallel X-ray beam, the image at angle θ should contain the exact same information as the image at angle $\theta + \pi$. So, $\Delta\theta = \pi$ should give the same resolution of the reconstructed volume, albeit with a lower signal to noise ratio compared to the full turn scan as we capture only half the number of images.

In case of a cone beam, $\Delta\theta$ needs to be larger than π because of the cone beam opening angle. For every point on the scanned object to be seen by rays in the whole range from 0 to π, the rotate stage needs to turn over an angular range $\Delta\theta = \pi + \alpha$, where α is the cone beam opening angle. Fig. 7 explains this.

This scan over a range $\Delta\theta = \pi + \alpha$ with a cone beam system presents a particular challenge to reconstruction. It is well known that straightforward reconstruction of such an acquisition with standard Filtered Back Projection introduces artefacts. The origin of these artefacts is the “asymmetry” in the dataset caused by the cone beam. As Fig. 7 shows, some parts of the objects are penetrated by more rays than others, and hence more information is available about the parts closer to the source. The new Half.Turn CT reconstruction solves this unfairness, and provides a reconstruction of the

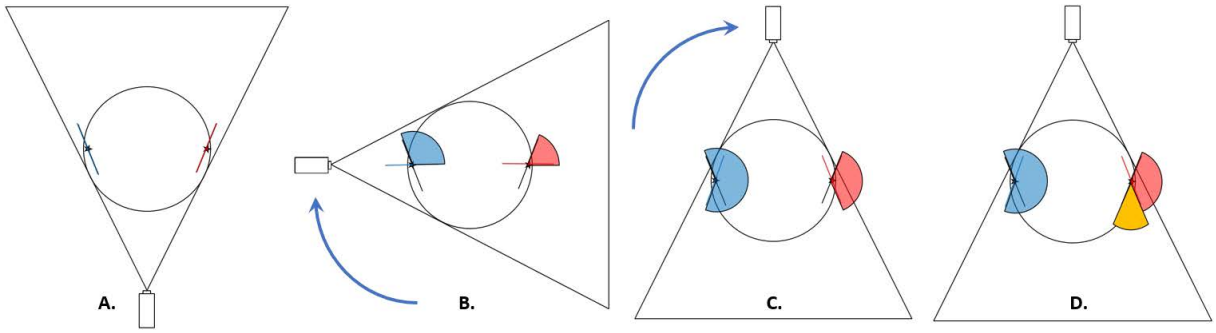

Fig. 7 For every region of the object to be seen by rays in a range of 0 to π, the stage needs to rotate over an angle of π + cone beam angle α. (A) Consider regions at opposite ends of the sample. The beam passes through these at an angle. (B) After 90° of rotation, the blue feature receives a wider angular coverage for the same rotation. The red feature on the opposite end receives less coverage. (C). After 180° of rotation, the blue feature has over 180° of coverage, and therefore has more than enough projection data to allow reconstruction. The red feature, however, has insufficient coverage. It will be missing detail at angles which have not been covered. (D) We must therefore rotate further to cover this missing angle. This additional angle is equal to the cone beam angle.

same quality as a full turn CT, without adding noticeable computation time. Fig. 8 shows that the quality of the new Half.Turn CT reconstruction is comparable to that of a standard FDK reconstruction of a full turn scan of the same opbject, while needing only about half of the images.

Fig. 9 compares the acquisition time of 2 CT acquisitions that produce equivalent data quality, one full turn scan on the XT H 225 ST, and one Half.Turn CT scan on the new XT H 225 2x system. The doubling of the speed is achieved through a combination of a more sensitive detector, allowing it to run at full frame rate of 15 frames per second, and the new Half.Turn CT reconstruction providing a reconstruction quality that is similar to that of the full turn scan.

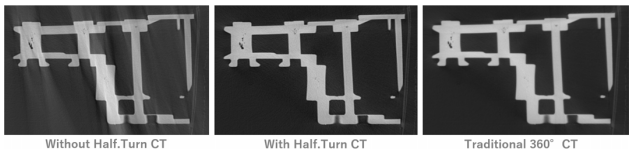

Fig. 8 Comparison between a Half.Turn CT acquisition reconstructed with standard FDK (left), the same acquisition reconstructed with the new Half.Turn CT reconstruction (middle), and a full turn CT acquisition reconstructed with standard FDK (right). The left figure clearly shows artefacts, while the quality of the Half.Turn CT reconstruction (middle) is comparable to that of a standard FDK reconstruction of a full turn scan (right).

4 2x improvements applied to Li-Ion battery cell inspection

For Li-Ion batteries, defects like inclusion of foreign particles, electrode delamination and incorrect anode overhang can be disastrous for their long-term performance and safe

	XT H 225 ST	XT H 225 ST & Half.Turn CT
Detector panel	PE1621EHS	XRD4343CT
Beam energy	165kV	180kV
Beam current	236µA	222µA
Power	39W	40W
Exposure time	88ms	67ms
Projections per full turn	3141	3800
Number of projections	3141	2126
Acquisition time	**4m52s**	**2m26s**

Fig. 9 Comparison of the acquisition time between a full turn CT acquisition on a XT H 225 ST, and a Half.Turn CT scan on the new XT H 225 ST 2x system. Acquisition speed is exactly doubled by the use of a more sensitive detector, combined with the new Half.Turn CT reconstruction.

operation. That's why it is important to catch these issues at the end of the line or even better, during the assembly process. As this is high volume production, cycle time is key without compromising on image quality.

The examples below show how the combination of Rotating.Target 2.0, the latest flat panel technology and Half.Turn CT allows users to drastically reduce scan time. See Fig. 10–14.

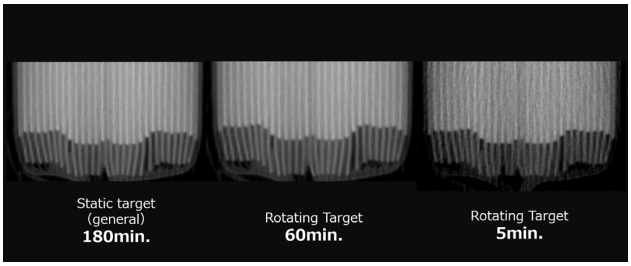

Fig. 10 Comparison of image quality of battery anode overhang using Rotating. Target 2.0 and ever shorter scan times.

Fig. 10 is a CT image of the anode overhang of the electrode stack of a Li-Ion battery cell, demonstrating the change of image quality when the scan time is shortened by using a Rotating.Target 2.0. The image on the left was acquired using a standard static reflection target; for the center image a Rotating.Target 2.0 was used and the scan time was reduced with a factor 3, while for the image on the right the scan time was further reduced with a factor 12. Even in the last case where the scan time is 36 times shorter than the original scan time, the image maintains sufficient resolution for proper overhang analysis.

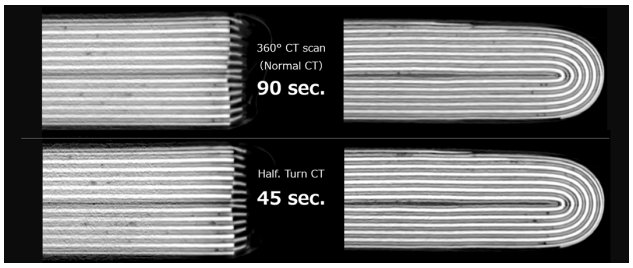

Fig. 11 Comparison of image quality using traditional circular CT versus Half.Turn CT.

Fig. 11 is a comparison of the image acquired in 90 seconds using traditional circular CT and the image acquired in 45 seconds using Half.Turn CT. In the last case, almost equivalent image quality is obtained in half of the time needed to scan the battery cell.

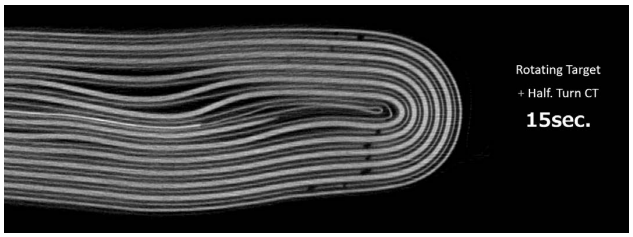

Fig. 12 Delamination and deformation of battery electrodes are clearly visible in a 15 seconds scan.

During the winding or stacking process of the anode, separator and cathode and during the further assembly process of the battery cell, delamination or deformation of the electrodes can happen. Fig. 12 is a CT image showing electrode delamination and deformation inside such a Li-Ion battery cell. The data set is acquired in just 15 seconds using Rotating Target 2.0 and Half.Turn CT.

Fig. 13 shows a CT image that captures the crack in a battery electrode. Cracks are a critical internal defect that can be introduced during the slitting process. A normal CT scan takes 45 seconds to acquire, but Nikon has made it possible to acquire it in just 15 seconds with Rotating.Target 2.0 and Half.Turn CT. Almost equivalent image quality is obtained with a 3 times shorter scan.

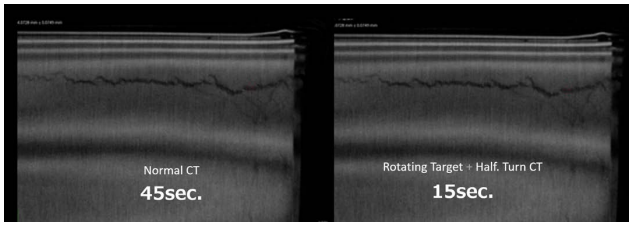

Fig. 13 Visualisation of an electrode crack in a 15 second CT scan.

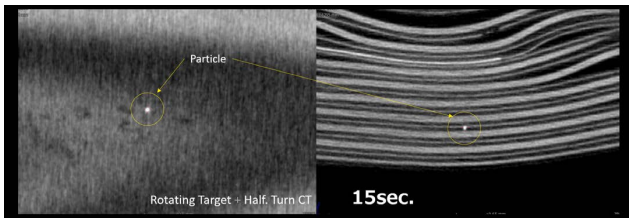

Fig. 14 Visualisation of foreign particle in a Li-Ion battery cell.

During the whole process from winding or stacking of electrodes up to the sealing of the battery cell, foreign particles can be catched inside the cell. Also the welds that connect the anode and cathode to the external battery terminal can include voids that result in bad electrical conductivity.

On Fig. 14 some foreign particles can be clearly seen on the CT image that was acquired in only15 seconds using Rotating.Target 2.0 and Half.Turn CT.

5 Conclusion

In this paper the new and improved features of Nikon's latest XT H 225 ST 2x industrial CT system were explained. These include Auto.Filament Control, that doubles filament lifetime, Half.Turn CT and X.Tend helical acquisition and reconstruction algorithms and the improved 225 kV Rotating.Target 2.0 X-ray source. It was shown how these features increase the scan speed of the system while maintaining or improving the image quality.

Fast scans and reliable analysis are a key requirement to enable the usage of X-ray CT for end-of-line testing and process control in a production environment. As an example of such an industrial application, the paper discusses the usage of the XT H 225 ST 2x system for fast inspection of Li-Ion battery cells. The results show that critical defects like incorrect anode overhang, electrode delamination and foreign particle inclusions can be detected in scans that take no more than 15 seconds.

This makes Nikon's X-ray CT system with its unique X-ray source and software technology, particularly suited for the inspection of Li-Ion battery cells, of which production volumes are increasing rapidly with the growing demand for Electric Vehicles. Also the mass production of other components like Plastic Injection Moulded connectors and small castings, that are widely used in Electrical Vehicles, will benefit from these advances in X-ray CT inspection.

References

[1] Feldkamp, L.A, David. L.C, Kress, J.W., "Practical cone beam algorithm," *Journal of the Optical Society of America A,* vol. 1, no. 6, p. 612–619, 1984.

[2] A. Katsevich, "Exact Filtered Back Projection (FBP) algorithm for spiral Computer Tomography," US Patent 6,574,299, Jun. 3, 2003.

[3] A. Katsevich, "Theoretically exact Filtered Back Projection-type inversion algorithm for spiral cone-beam," *SIAM J. Appl. Math.*, vol. 62, no. 6, p. 2012–2026, 2002.

[4] A. Katsevich, "An improved exact Filtered Back Projection algorithm for spiral Computed Tomography," *Adv. Appl. Math.*, vol. 32, no. 4, p. 681–697, 2004.

坂口直史　Naoshi SAKAGUCHI
産業機器事業部 マーケティング部
Global Marketing Department
Industrial Metrology Business Unit

David BATE
Nikon X-TEK Systems Ltd

Jan DE GEETER
Nikon Metrology NV

Jos JANS
Nikon Metrology NV

Ben MORGAN
Nikon Metrology NV


坂口直史
Naoshi SAKAGUCHI


David BATE


Jan DE GEETER


Jos JANS


Ben MORGAN

顕微鏡対物レンズ CFI Plan Apochromat λD シリーズの開発

高木英嗣

Development of the CFI Plan Apochromat Lambda D Series Objectives for Biological Microscopes

Hidetsugu TAKAGI

プランアポクロマート λD シリーズを2021年12月に発売した．世界最高レベルの NA と WD を有し，視野全域における優れた光学性能を誇り，広波長帯域の色収差補正がなされたプランアポクロマート対物レンズシリーズである．ニコンの顕微鏡対物レンズの最高峰に位置するプランアポクロマート対物レンズシリーズには，これまで λ シリーズと VC シリーズがあった．本論文では λ シリーズと VC シリーズの長所を継承した λD シリーズの光学設計技術と製造技術について紹介する．

顕微鏡システムにおいて最も重要な心臓部と言われる顕微鏡対物レンズの重要事項の 1 つに光学硝材選択がある．特に，広波長帯域の色収差補正を実現するには，最適な光学硝材を選択する必要がある．ここでは 2 枚の薄肉単レンズの色消しから出発し，3 枚の薄肉単レンズの色消しについて説明する．更に共焦点レーザー走査型蛍光顕微鏡における色収差の影響を解説し，観察画像を比較する．

ニコンの誇る波面収差計測技術と最適化技術から生まれた波面収差最適化システムについて説明する．この波面収差最適化システムのシミュレーション結果を報告する．

In December 2021, we launched seven models of CFI Plan Apochromat Lambda D Series objectives for biological microscopes. The Plan Apochromat objective lens series provides the world's highest levels of Numerical Aperture and Working Distance, excellent optical performance over the entire field of view, and chromatic aberration correction across a wide wavelength range.

To date, the Plan Apochromat objective lens series, which is the highest spec of Nikon's microscope objective lenses, comprised the λ and VC series. Herein, we introduce the optical design and manufacturing technologies of the λD series, which has the advantages of both λ and VC series.

We begin with the achromatism of two thin lenses, explain that of three thin lenses and the influences of chromatic aberration in a confocal laser scanning fluorescence microscope, and finally show the actual images.

Furthermore, we explain the wavefront aberration optimization system developed using Nikon's wavefront aberration measurement and optimization technologies. Finally, we report the simulation results of this wavefront aberration optimization system.

Key words 対物レンズ，解像限界，顕微鏡
objective lens, resolution limit, microscopy

1 Introduction

In recent years, remarkable progress has been made in optical microscopy systems. However, from the time of E. Abbe to the present day, the objective microscope lens remains the heart of the optical microscope and determines its resolution.

This paper introduces the CFI plan apochromat λD series launched in December 2021 (Fig. 1).

2 Development Background

Thus far, among the pinnacle of Nikon's plan apochromatic objective lens series were the λ and VC series.

The λ series has high aberration performance with wide and peripheral fields of view, which are the most prominent features of Nikon microscope systems, and high transmittance from the visible to the near-infrared region using Nano Crystal Coat. On the other hand, the VC series features an axial chromatic aberration performance in the visible range from 405 nm, which the λ series does not have, and was

highly regarded in the market, especially concerning confocal laser scanning fluorescence microscopy.

In recent years, with the development of digital imaging technology and fluorescent dye technology in the biological microscopy market, there has been a desire for a microscope objective lens that enables observation in a wide field of view and a wide wavelength band from bright-field observation to confocal laser scanning fluorescence microscopy. Indeed, the microscope objective lens, which inherits the advantages of the λ series and VC series, was what was needed.

Fig. 1 Images of the present objective lens series

3 Specifications

The CFI plan apochromat λD series is a series of plan apochromatic objective lenses with the world's highest numerical aperture (NA) and working distance (WD) standards, excellent optical performance at the field of view

Table 1 Specifications of CFI plan apochromat λD series

	60x	100x	40x	20x
NA	1.42	1.45	0.95	0.80
WD [mm]	0.15	0.13	0.21*	0.80
Chromatic correction	Apo	Apo	Apo	Apo
Flatness	Plan	Plan	Plan	Plan
Immersion medium	Oil	Oil	Dry	Dry

	10x	4 x	2 x
NA	0.45	0.20	0.10
WD [mm]	4.00	20.0	8.50
Chromatic correction	Apo	Apo	Apo
Flatness	Plan	Plan	Plan
Immersion medium	Dry	Dry	Dry

* with correction ring

periphery, and chromatic aberration correction over a wide wavelength band. It supports all Nikon microscopes and systems. In developing this new series, the power layout was reviewed from the ground up, and everything from design to manufacturing and inspection was completely redesigned.

The specifications of the objective lens series in this report are shown in Table 1.

4 Chromatic Aberration Correction in the Wide Wavelength Range

One of the essential factors in the optical design of microscope objectives is the selection of optical glass material. Here, we introduce the axial chromatic aberration based on three thin lenses necessary to realize the correction of axial chromatic aberration in a wide wavelength range and explain the basic concept of lateral chromatic aberration correction.

First, the first-order and second-order color cancellation conditions for two thin lenses, a and b, are confirmed, and then the conditions are extended to three thin lenses. First-order chromatic aberration means that the focal points of two wavelengths overlap, and second-order chromatic aberration means that the focal points of three wavelengths overlap. Second-order chromatic aberration correction is essential for correcting chromatic aberration in a wide wavelength band. The composite focal length and conditions for achromatization for two thin lenses can be written as follows:

$$\Phi_a + \Phi_b = \Phi \tag{1}$$

$$\frac{\Phi_a}{\nu_a} + \frac{\Phi_b}{\nu_b} = 0 \tag{2}$$

$$P_a \frac{\Phi_a}{\nu_a} + P_b \frac{\Phi_b}{\nu_b} = 0 \tag{3}$$

Here, νa, Pa , Φa, represent the Abbe number, partial dispersion ratio, and power of the thin lens, respectively. The power is the reciprocal of the focal length. The optical glass material that satisfies the condition in Eq. (4) is required to achieve first-order and second-order color cancellation with two thin lenses. To achieve the above Conditions for achromatization as close as possible, the dispersion properties of glasses of the optical glass of thin lenses a and b must have a larger Abbe number difference and a smaller partial dispersion ratio difference.

$$\frac{(P_a - P_b)}{(\nu_a - \nu_b)} \Phi \cong 0 \tag{4}$$

However, optical glass materials are discrete and limited

even when fluorite or other materials are used, making it impossible to achieve axial chromatic aberration correction over a wide wavelength band.

Therefore, we extend the idea of two thin lenses to three thin lenses, *a*, *b*, and *c*.

$$\Phi_a + \Phi_b + \Phi_c = \Phi \tag{5}$$

$$\frac{\Phi_a}{\nu_a} + \frac{\Phi_b}{\nu_b} + \frac{\Phi_c}{\nu_c} = 0 \tag{6}$$

$$P_a \frac{\Phi_a}{\nu_a} + P_b \frac{\Phi_b}{\nu_b} + P_c \frac{\Phi_c}{\nu_c} = 0 \tag{7}$$

These equations can be expressed as follows: [1]–[3].

$$\Phi_b = \frac{P_c - P_a}{P_b - P_a} \frac{\nu_b}{T} \Phi \tag{8}$$

$$T = \frac{\nu_a (P_b - P_c) + \nu_b (P_c - P_a)}{P_b - P_a} - \nu_c \tag{9}$$

Fig. 2 shows the Glass map of partial dispersion ratio and Abbe number. Here, T is the line length extending from point c to the line connecting points **a** and **b** parallel to the horizontal axis in axis in the Glass map of partial dispersion ratio and Abbe number. It is difficult to satisfy the achromatic conditions for two thin lenses, by using two optical glass materials, **a** and **b**, a virtual optical glass material d' is created. Especially, the sign of Φ_b is noteworthy: Φ_b has a positive power when glass materials with dispersion properties of glasses are used, as shown in Fig. 2. This convention shows that axial chromatic aberration can be reduced by adding flint-type optical glass with a positive partial dispersion ratio, in addition to fluorite and crown-type optical glass.

In existing optical systems, in practice, a more complex design is required. More than a dozen pieces of optical glass

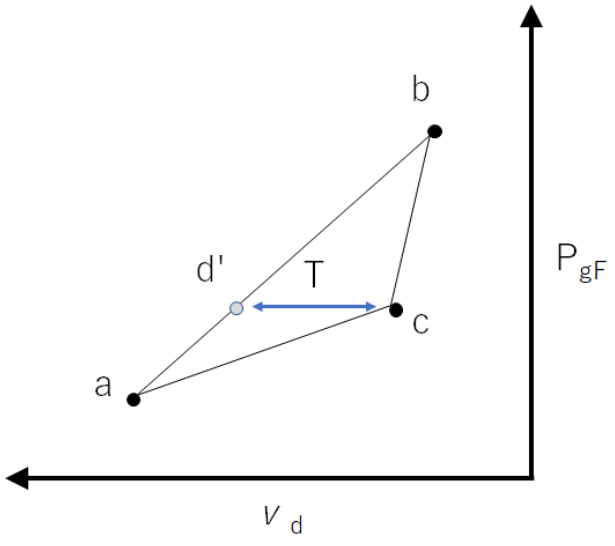

Fig. 2 Glass map of partial dispersion ratio and Abbe number

are combined to correct axial chromatic aberration over a wide wavelength band.

Before explaining the correction of lateral chromatic aberration, I would like to mention the history of the development of microscope objective lenses. The compensating method compensates for lateral chromatic aberration using an eyepiece and objective lens combination. Hence, lateral chromatic aberration occurred when observing a camera without an eyepiece. Therefore, around 1976, Nikon adopted the chromatic aberration Free (CF) method and developed a microscope system in which the objective and eyepiece lenses are each individually corrected for aberration [4]. Furthermore, in confocal laser scanning fluorescence microscopy, which is widely used as a general observation method, the shading in the periphery of the field of view due to the magnification chromatic aberration, which has not been a problem until now, has become an issue.

This paper introduces technology that can correct lateral chromatic aberration, especially in high-magnification objective lenses.

As shown in Fig. 3, the main power configuration of a high magnification objective lens is arranged in the order of the front group with positive power and the rear group with negative power, starting from the object (sample) side. For simplicity, the figure shows the d-line ray (green) as the primary ray and only the direction of the F-line ray (purple) to show the chromatic aberration at short wavelengths. The front group corrects image curvature, axial chromatic, and spherical aberrations. On the other hand, the rear group is at a greater distance from the optical axis that the rays pass through. As shown in Fig. 3, both the front group with positive power and the rear group with negative power produce positive lateral chromatic aberration on the image plane. As shown in Fig. 3, the flint-type optical glass has higher dispersion than the crown-type optical glass, so its F-line can be corrected more efficiently.

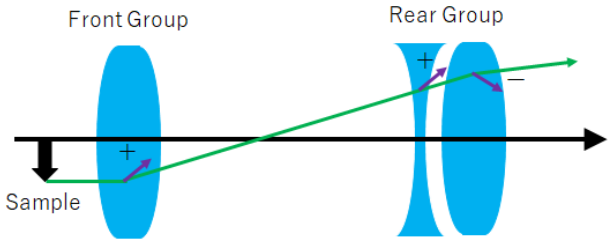

Fig. 3 Power configuration of high-magnification objective lenses

In particular, the immersion medium of oil-immersion objective lenses has higher dispersion than water or silicone immersion lenses. Since the chromatic aberration caused by

the oil is large, the chromatic aberration that must be corrected with the oil immersion objective lens is also large. High-dispersion optical glass may be used for the flint-type optical glass with the positive power described above. In this case, the second-order spectrum of lateral chromatic aberration is generated as the residue after the first-order spectrum of lateral chromatic aberration is corrected. For this reason, it is desirable to use optical glass with a lower partial dispersion ratio for the positive lens in the rear group and optical glass with a higher partial dispersion ratio for the negative lens. Nikon has a high degree of freedom in selecting glass materials because the development of the production process of optical glass materials is performed within the Nikon Group, enabling optical design that corrects for the axial chromatic aberration and second-order spectrum of lateral chromatic aberration. The effect of this lateral chromatic aberration on image quality and the effect of the designs are described in the next section.

5 Confocal Laser Scanning Fluorescence Microscope

This section discusses the effect of the second-order spectrum of lateral chromatic aberration on confocal laser scanning fluorescence microscopy. The confocal laser scanning fluorescence microscope is configured as follows (Fig. 4).

Excitation light from a laser light source passes through the objective lens and irradiates a fluorescent sample, and the fluorescence emitted is detected as a signal by the objective lens. At that moment, the wavelength of the excitation light and the fluorescence wavelength differs by several 10 to several 100 nm due to the Stokes shift. Here, we consider how the slight chromatic aberration in this wavelength difference affects image quality.

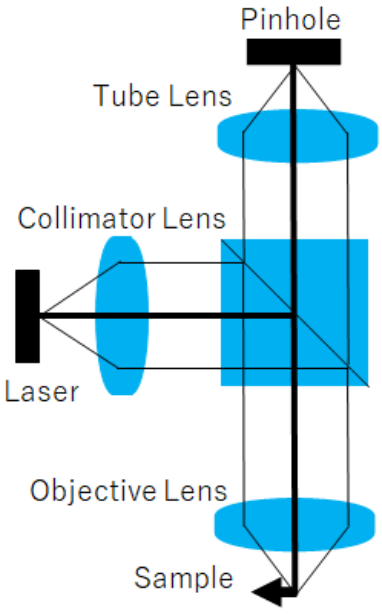

Fig. 4 Schematic of the confocal laser scanning microscope

$PSF_{ex}(x)$ is the Point Spread Function of the excitation optics of the confocal laser scanning fluorescence microscope, and $PSF_{em}(x)$ is Point Spread Function of the fluorescence optics. $PH(x)$ is the transmittance distribution representing the pinhole shape, and the Point Spread Function I obtained by laser scanning is multiplied by

$$I = o(x) * [PSF_{ex}(x) \cdot (PSF_{em}(x) * PH(x))] \quad (10)$$

where $o(x)$ is the density distribution of the fluorescent sample. $*$ is the convolution integral. The effective Point Spread Function $PSF_{eff}(x)$ is then defined as follows [5]:

$$I = o(x) * PSF_{eff}(x) \quad (11)$$

$$PSF_{eff}(x) = [PSF_{ex}(x) \cdot (PSF_{em}(x) * PH(x))] \quad (12)$$

Fig. 5 shows the Point Spread Function $PSF_{ex}(x)$ of the excitation light, $PSF_{em}(x)$ of the fluorescence, transmittance distribution (PH) of the pinhole, effective Point Spread Function $PSF_{eff}(x)$, Point Spread Function of excitation light $PSF_{ex}(x)$, Point Spread Function of fluorescence $PSF_{em}(x)$, and the effective Point Spread Function of the pinhole $PSF_{eff}(x)$. Here, $PSF_{ex}(x)$, $PSF_{em}(x)$, and $PH(x)$ are normalized

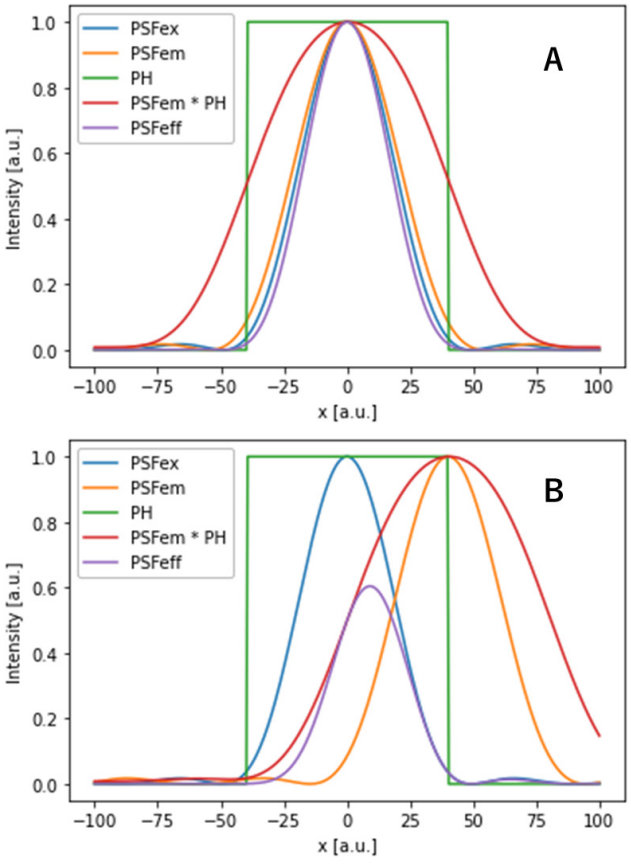

Fig. 5 Effective Point Spread Function of confocal laser scanning microscope PSF_{eff}

to be at most 1.

On the other hand, Fig. 5B shows the calculation results when lateral chromatic aberration occurs. The intensity distribution of the excitation light $PSF_{ex}(x)$ and the fluorescence $PSF_{em}(x)$ are shifted horizontally, and the intensity of the effective Point Spread Function $PSF_{eff}(x)$ is reduced. As a result, the confocal laser scanning fluorescence microscope image appears as shading.

More intuitively, the fluorescent sample excited by the laser passes through the detection optics, and the signal is detected through the pinhole, and if the detection optics has chromatic aberration, the signal intensity is reduced. If the detection optics has chromatic aberration, the signal intensity is reduced. For axial chromatic aberration, similar behavior is observed in the optical axis direction.

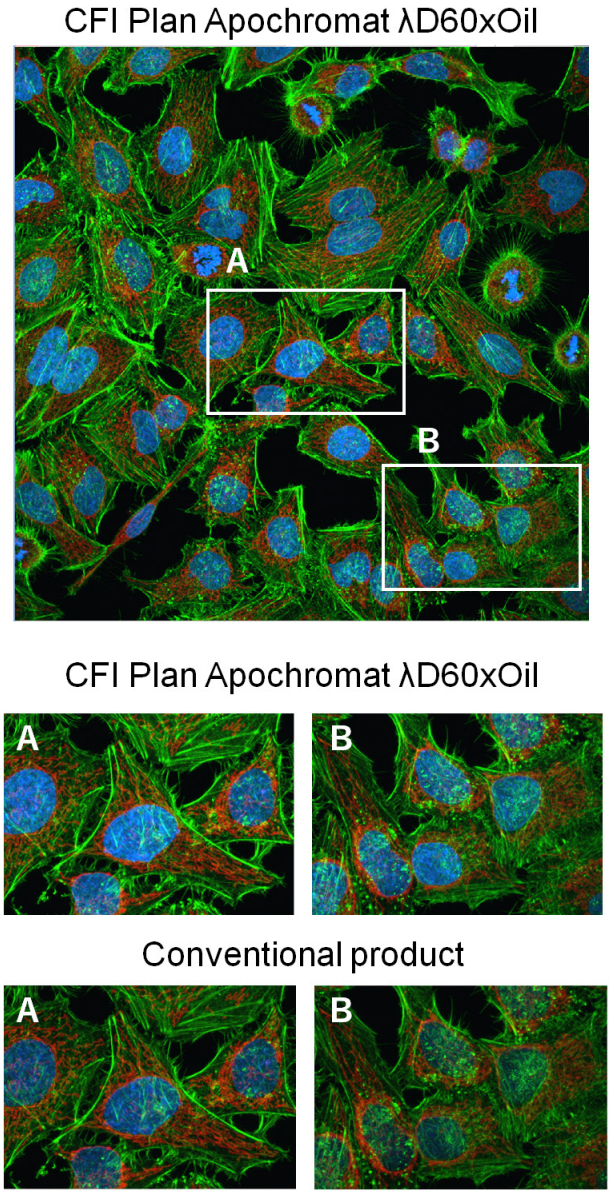

Fig. 6 Confocal laser scanning microscope FOV25 images of CFI plan apochromat λD60xOil and conventional objective lens
Hela cells: DAPI, 488-Actin, 568-Mitochondria

In the calculations shown in Fig. 5, the effect of lateral chromatic aberration was not included in the discussion of the effect of lateral chromatic aberration. However, when off-axis coma aberration and off-axis asymmetry occur, the Effective Point Spread Function $PSF_{eff}(x)$ decreases, and the shape of $PSF_{eff}(x)$ collapses, reducing resolving power. In the newly developed series of objective lenses, coma and asymmetric aberrations have been thoroughly eliminated to obtain sharp images with a little shading to the periphery of the field of view.

To demonstrate the effect of the developed objective lens, we compared the developed objective lens with a conventional objective lens in wide-field confocal laser scanning fluorescence microscopy with an FOV25. All observation conditions other than the objective lens were the same. In the conventional product, DAPI-stained cell nuclei are dark even at the center of the field of view due to axial chromatic aberration and extremely dark on the periphery of the field of view due to lateral chromatic aberration.

This shading change from the field of view center to the periphery does not change even when the laser power is increased. On the other hand, the CFI plan apochromat λD 60x, in which axial and lateral chromatic aberrations are corrected, produces sharp and uniform image qualities from the center of the field of view to the periphery.

6 Wavefront Aberration Optimization System

This section introduces the manufacturing technology of microscope objective lenses. Although microscope objective lenses are designed to be nearly aberration-free, aberrations occur due to manufacturing errors. Therefore, it is vital to have a wavefront aberration measurement device that accurately measures the wavefront aberration amount of the objective lens and an optimization technique that brings it as close to the designed value as possible.

A microscope observes a collection of point light sources emitted from a sample as an object. The light emitted from an ideal point source is converted to a parallel plane wave through the microscope objective. If the microscope objective lens has an aberration, it has an error from the ideal plane wave. This small error is called wavefront aberration and is used to evaluate the imaging performance of the optical system. In particular, the Zernike polynomial is an orthogonal polynomial defined on the unit circle, which is a good match for optical aberration. Nikon's wavefront mea-

surement technology is used in microscope objectives but also in semiconductor lithography equipment and interchangeable camera lenses, making it one of the most important technologies supporting imaging technology.

Even if each lens is manufactured with manufacturing tolerances of a few microns, the generated wavefront aberration cannot be ignored because the wavelength of light is several 100 nm. Therefore, the assembly must be optimized to minimize wavefront aberrations, equivalent to solving the following problem. For example, it can be expressed as in Eq. (13). In Eq. (13), the measured wavefront aberration expressed by the Zernike polynomial is denoted by z, and the variable x represents the state of the compensator. The change matrix for the sensitivities is denoted by $\boldsymbol{H}$. We must find the optimal solution x of the compensator so that each Zernike component is zero. Such a calculation can often be performed using the least-squares method to obtain the optimal solution [6].

$$min_x \left\| \boldsymbol{H}\boldsymbol{x} - \boldsymbol{z} \right\|^2 \tag{13}$$

Microscope objectives require high aberration performance over the entire field of view. More than ten lenses are used in the same parfocal distance of only 60 mm to correct axial chromatic aberration over a wide wavelength band. Therefore, the components of the compensator's variation matrix H, which indicates the sensitivity to aberration components, are hardly independent. For example, if the components of this variation matrix are not independent, compensating for the aberration component z1 using one compensator x1 increases another aberration component z2. In reality, the compensator has a finite range of motion, and the compensator has errors. Hence, it cannot be expressed in a simple expression like Eq. (13) and becomes a more complex constrained optimization problem. Alternatively, the complex constrained optimization problem must be solved and optimized for each objective lens measured by wavefront aberration. Before the advent of wavefront aberration optimization systems, microscope lens operators had to be adjusted by hand. In particular, high magnification, high-NA objectives have extremely high sensitivity, and spherical and eccentricity-coma aberrations are required to the resolution limit. These requirements make the manufacture of these objectives extremely difficult.

Even before recent AI technology became widely adopted, Nikon had developed its own optical design software and continued research and development over many years in the optimization field along with evaluation calculations for optical systems.

We applied our proprietary optimization engine to solve the complex constrained optimization problem during the assembly and adjustment of microscope objectives. As the simulation results of the optimization system, Fig. 7A and Fig. 7B show the wavefront aberration of the objective lens before adjustment and after optimization using the wavefront aberration optimization system, respectively. The wavefront aberration of the ideal optical system has a flatter shape. In other words, the optical system is approaching aberration-free image formation (Fig. 7B).

These wavefront aberration measurement and optimization technologies bring each microscope's objective lens as close as possible to the optical design value. This manufacturing system is the ideal system for manufacturing objective lenses.

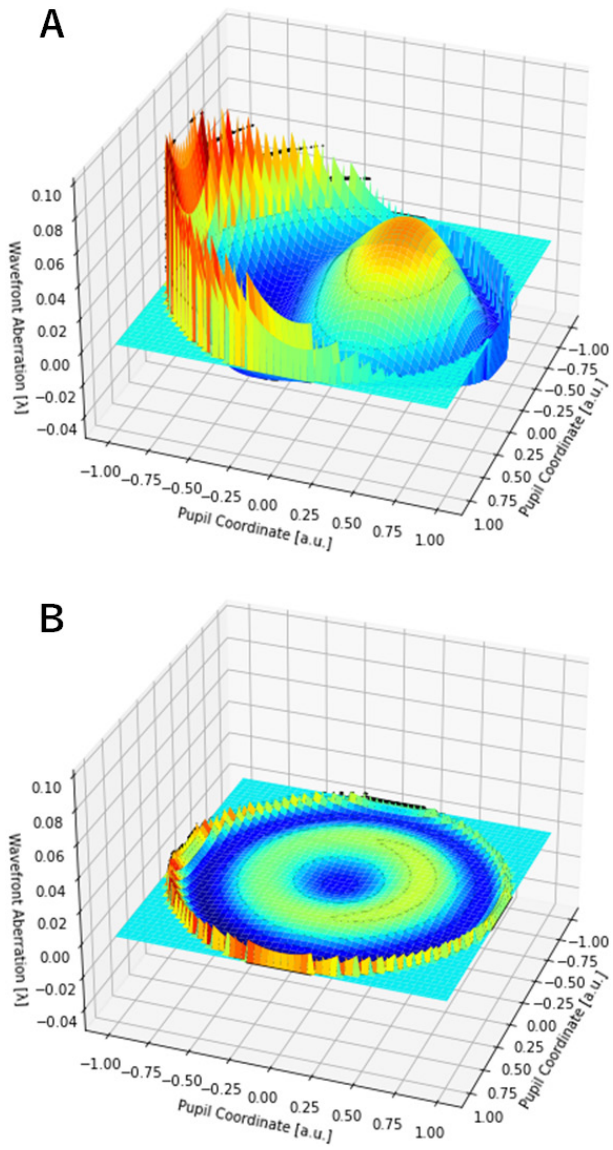

Fig. 7 Simulation of the wavefront aberration optimization system

7 Conclusion

The CFI plan apochromat λD series is a microscope objective lens series that integrates the λ series and VC series to achieve NA, WD, flatness, and field of view. This objective lens series is suitable for the heart of Nikon microscope systems with high aberration performance in the wide and peripheral fields of view, which are the essential features of the Nikon microscope systems, and with chromatic aberration correction over a wide wavelength band.

Nikon's optical design and manufacturing technologies are combined to make this objective lens series significantly contribute to developing scientific and industrial technologies, including bioimaging.

Though I have taken the lead in writing this article, it represents the work of many dedicated individuals who have contributed to this development. I want to take this opportunity to express my deepest gratitude to them.

References

[1] A. E. Conrady, *Applied Optics and Optical design*, Part 1. Dover Publications, 1929.
[2] H. Gross, H. Zugge, M. Peschka, F. Blechinger, *Handbook of Optical Systems*, Vol. 3. Wiley-VCH, 2007.
[3] Zyun Koana, *Geometric Optics*, (in Japanese), New Technology Communications, 1986.
[4] Kazuo Ushida, "New Microscope Optical System," *Kogaku*, (in Japanese), vol. 10, no. 5, pp. 22–29, 1981.
[5] Masato Shibuya, Hiroshi Ohki, *Optics of diffraction and imaging*, (in Japanese), Asakura Publishing Co., Ltd., 2005.
[6] Tomowaki Takahashi, *Lens Design-From aberration coefficient to automatic design*, (in Japanese), Tokai University Press, 1994.

高木英嗣　Hidetsugu TAKAGI
光学本部 第一設計部
1st Designing Department
Optical Engineering Division

高木英嗣
Hidetsugu TAKAGI

AI 画像処理技術を活用したミトコンドリアの詳細解析

門井宏平，武居俊輔

Detailed Analysis of Mitochondria using AI Image Processing Technology

Kohei KADOI and Shunsuke TAKEI

ミトコンドリアは主要な細胞内小器官の一つであり，エネルギー代謝を司るため基礎研究分野のみならず創薬開発等の応用分野で幅広く研究されている．ミトコンドリアの研究では，ミトコンドリアを蛍光分子で標識し解析する手法が主流であり，動態の解析にはタイムラプス撮影が不可欠である．しかし，蛍光観察では蛍光分子の励起を行うことにより，光毒性によるミトコンドリア活性や形態への影響，蛍光の褪色が生じ得る．また，ミトコンドリアは微細な構造であるため，定量解析を行う場合には鮮明な画像を用意する必要がある．このため，可能な限り低い励起光強度や短時間露光の条件で，細胞へのダメージや蛍光褪色を回避し，鮮明な画像を得る技術が求められている．

顕微鏡画像統合ソフトウェア NIS-Elements は artificial intelligence（AI）の一種である深層学習技術を用いた画像処理機能（NIS.ai）を搭載している．本稿では，低い励起光強度で取得した不明瞭な画像から明瞭な画像を生成する機能（Enhance.ai）を用いることで，ミトコンドリア解析における光毒性を回避できる効果を確認した．さらに，焦点面外から発せられる蛍光シグナルを除去する機能（Clarify.ai）もミトコンドリアの定量解析に有用であることを示した．これらの技術により，従来よりも正確かつ詳細なミトコンドリア動態解析が可能になり，現象解明への寄与が期待される．

Mitochondria, which are one of the major organelles for controlling energy metabolism, have been extensively studied in the fields of basic and applied research of biology, drug discovery research, and so on. Mitochondrial studies generally utilize the method of staining with fluorescent molecules while time-lapse imaging is indispensable for analyzing mitochondrial dynamics. However, in fluorescence experiments, the excitation of fluorescent molecules may affect mitochondrial activity and morphology owing to phototoxicity and fluorescence photo bleaching. In addition, owing to the fine structure of mitochondria, it is necessary to prepare a clear image when performing quantitative analysis. Therefore, a technique for obtaining clear images which avoids damage to cells and fluorescence photo bleaching under the conditions of excitation light intensity and short exposure as low as possible is desired.

The NIS-Elements imaging software for microscope, is implemented with an image processing function using deep learning technology (NIS.ai). In this study, we confirmed the effect of avoiding phototoxicity in mitochondrial analysis by using the function (Enhance.ai) to generate a clear image from an unclear image acquired using low excitation light intensity. Furthermore, it was shown that the function for removing blurred light from outside the focal plane (Clarify.ai) is also useful for the quantitative analysis of mitochondria. These technologies enable more accurate and detailed mitochondrial dynamics analysis than before, and are expected to contribute to the elucidation of phenomena.

Key words ライフサイエンス，顕微鏡，画像処理，深層学習，ミトコンドリア
life science, microscopy, image analysis, deep learning, mitochondria

1 Introduction

In the life sciences, digital image processing is commonly used for specimen images acquired using biological microscopy.

Recently, various image processing techniques that use deep learning technology have been investigated. These techniques have been proposed to improve the image quality of the acquired images and are expected to be applied to various research fields because these can facilitate imaging under conditions that are less toxicity to biological specimens. Additionally, these techniques are likely to improve the efficiency of quantitative analysis.

NIS-Elements is an imaging software for microscope systems. It provides microscope and camera control, image processing, analysis, and reporting functions. Nikon implemented NIS.ai modules as image-processing function based on deep learning technology in NIS-Elements. In this paper,

we focused on mitochondrial research and introduce several effective applications of NIS.ai functions along with Enhance.ai, a function that generates a clear image from a blurred image taken under conditions that minimize the effects of staining and other treatments on biological specimens.

2 Importance and Challenges of Mitochondrial Research

Mitochondria, which are intracellular organelles, play an important role as sites for producing the energy used by living organisms. Accordingly, mitochondrial activity and quality maintenance mechanisms are implicated in various diseases. Hence, these mechanisms have attracted considerable attention in areas ranging from basic research to drug discovery and applied research [1].

Time-lapse observation using a microscope enables the real-time visualization of biological phenomena. Therefore, microscopic time-lapse imaging is an indispensable technique for mitochondrial research, where changes in morphology and behavior over time are indices for analysis [2]. However, fluorescence staining is used to visualize mitochondria, and a high excitation light intensity and long exposure time are required to obtain clear fluorescence images for quantitative analysis. In time-lapse imaging, repeated exposure to excitation light inevitably causes photobleaching and phototoxicity owing to the production of reactive oxygen species [3]. This can decrease the accuracy of structure detection and quantification owing to photobleaching or damage the cells, which may affect the biological phenomena under observation [4]. By contrast, if the excitation light intensity is suppressed and the exposure time is shortened to avoid phototoxicity and photobleaching, obtaining clear images with a detectable mitochondrial morphology becomes difficult. Hence, a technique is needed to obtain clear images under the lowest possible excitation light intensity and a short exposure time while avoiding damage to cells and the photobleaching of fluorescence.

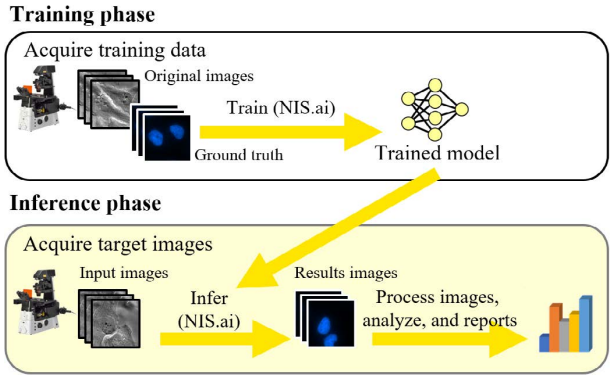

Fig. 1 Training and inference workflow using NIS.ai

3 AI Image-Processing Technology and Time-lapse Morphological Analysis of Mitochondria

NIS.ai uses convolutional neural networks, a type of deep learning, and employs supervised learning, which requires training data. Notably, Enhance.ai can be trained by users. Specifically, processing with Enhance.ai requires training, which consists of two phases: a training phase, where a trained model is further trained using training data prepared by the user, and an inference phase, where target images are output from the target data (input image) using the result of the training (Fig. 1).

The training data is a pair of fluorescence images. One image has an undesirably low signal/noise ratio (S/N) and a small difference in fluorescence intensity between the background and signal regions, whereas the other image has a high-S/N and is clear. The resulting training model is applied to the low-S/N fluorescence image, which is processed to obtain a high-S/N fluorescence image. The left fluorescence image in Fig. 2 is a low-S/N fluorescence image of the labeled mitochondria, which was enhanced by contrast adjustment, resulting in a blurred image with significant noise. When Enhance.ai is applied to the image, a high-S/N

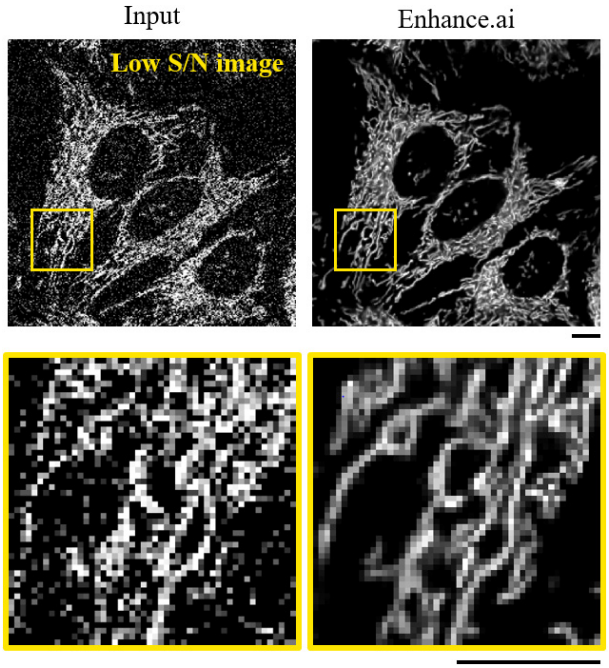

Fig. 2 Improved image S/N using Enhance.ai
Input: Low-S/N fluorescence image input to Enhance.ai. Enhance.ai: Inference results using Enhance.ai. The lower panel shows the enlarged image of the yellow rectangle in the upper panel. Scale bars are 10 μm.

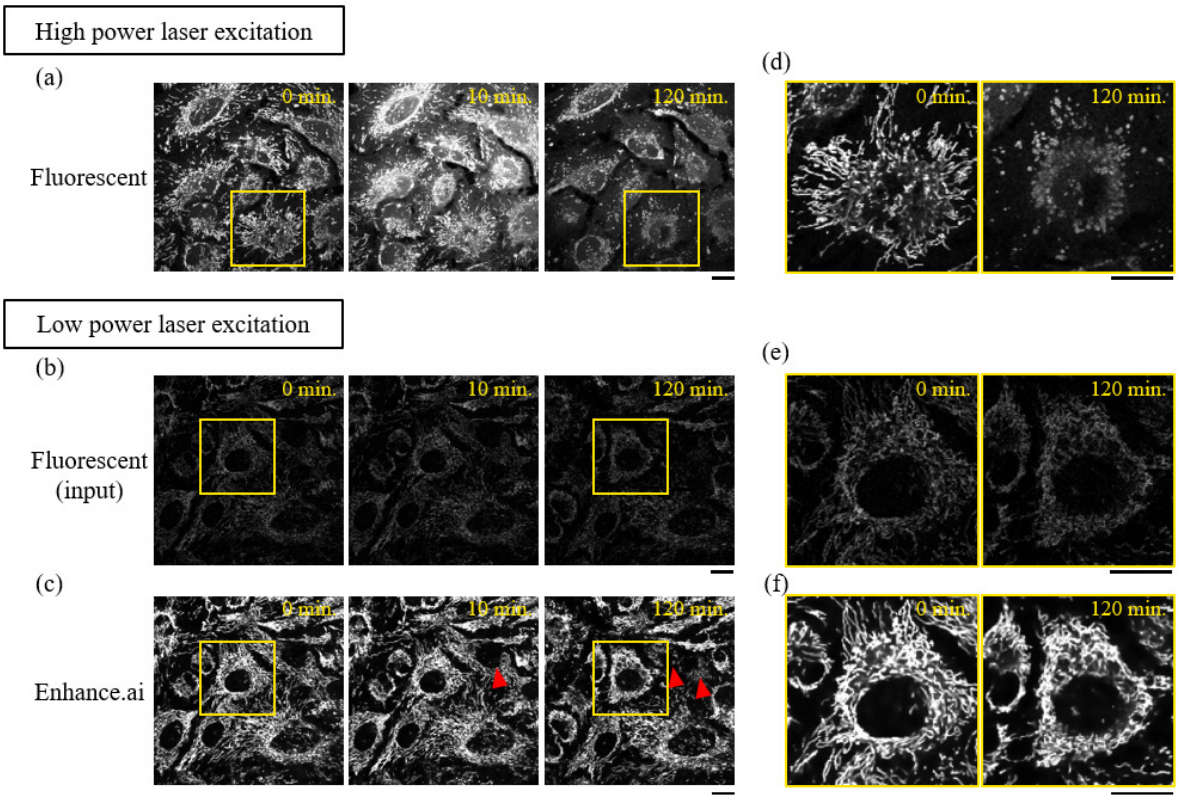

Fig. 3 Comparison of mitochondrial morphology under fluorescent excitation and Enhance.ai output

(a-c) Time-lapse images at 0 min (left), 10 min (center), and 120 min (right) acquired every 10 s. Scale bars are 20 μm.

(a) Fluorescence image of MitoTracker Red CMXRos (Thermo Fisher Scientific, Waltham, US) excited by a high-power laser.

(b) MitoTracker Red CMXRos fluorescence image excited by a low-power laser, used as input image to Enhance.ai. The image contrast setting was increased up to 4-times compared to (a).

(c) Output image using Enhance.ai with (b) as input image. Contrast is adjusted with (a). Red arrowheads indicate cells undergoing division.

(d-f) Magnified images of the yellow rectangle in (a-c), respectively. Scale bars are 20 μm.

image, in which individual mitochondria can be observed, is obtained, as shown in the right image in Fig. 2.

To verify the effects of using Enhance.ai combined with a low excitation-light intensity for fluorescence to study mitochondrial morphology, a confocal microscope was used to acquire two types of time-lapse images every 10 s for 120 min. High-S/N images were obtained by adjusting the intensity of the laser, which served as the excitation light, and low-S/N images were obtained by setting the laser intensity to the minimum. Enhance.ai was applied to the low-S/N images.

When the laser intensity was set to obtain high-S/N images, mitochondrial phototoxicity appeared approximately 10 min after the observation started, and fragmentation progressed to complete destruction after 120 min (Fig. 3(a), (d)). This is understood to be due to the phototoxic effect of the excitation light on the mitochondria and their fundamental cellular function. However, when fluorescence images were obtained with the laser intensity set to the minimum, the images were indistinct (Fig. 3(b), (e)), but Enhance.ai made individual mitochondria very clear (Fig. 3(c), (f)). No changes in image quality due to mitochondrial fragmentation or photobleaching occurred even 120 min after the observation started. Additionally, cell division progressed during the 120 min of observation (Fig. 3(c), red arrowheads), suggesting that the cells maintained their normal functions.

Next, the changes in mitochondrial morphology over time were evaluated quantitatively (Fig. 4). For quantitative analysis, the image processing and measurement functions of NIS-Elements, i.e., General Analysis 3, were used. By using the images enhanced by Enhance.ai for image analysis, mitochondrial morphology could be accurately identified and measured (Fig. 5). As measurement items, we calculated the total length of mitochondria, within the image field in which the mitochondrial region was detected, along with the rate of change in the total length of mitochondria per cell. Additionally, the changes were observed over time. The number of cells in the field of view was quantified by detecting the cell nucleus region in the fluorescent image of mitochondria using the Convert.ai function, which is an NIS.ai functions.

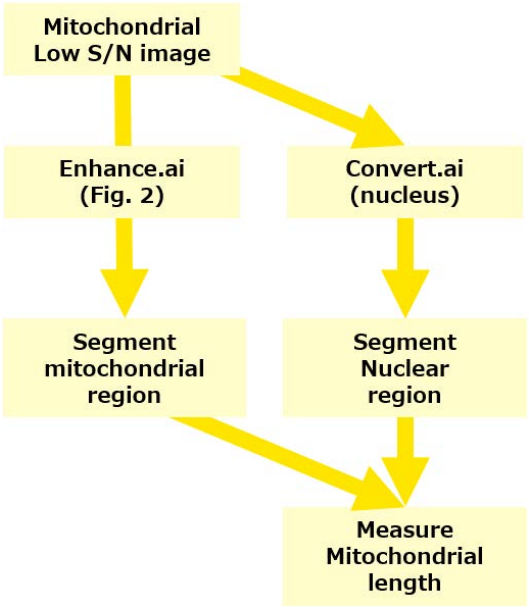

Fig. 4 Flow of mitochondrial analysis using Enhance.ai

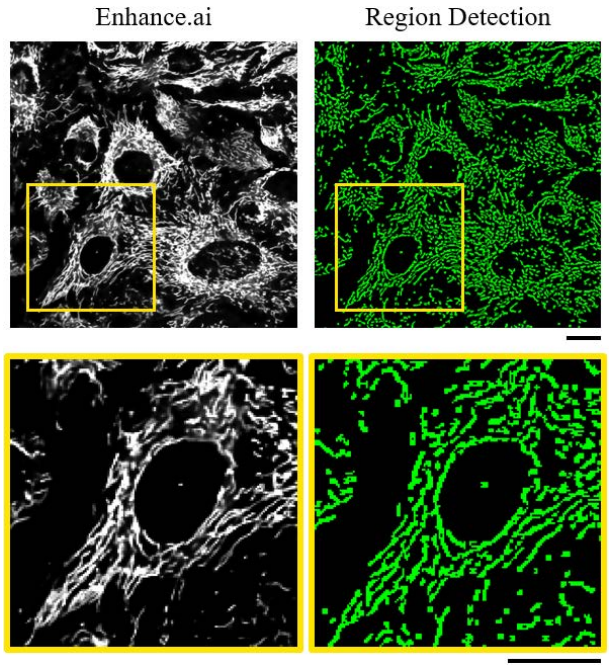

Fig. 5 Mitochondrial region detection using Enhance.ai output image

Enhance.ai: Enhance.ai output results. Region detection: Mitochondrial regions detected using the General Analysis function. The bottom image is a magnified image of the yellow rectangle in the upper panel. Scale bars are 20 μm.

The results showed that when the laser intensity was high, mitochondrial morphology began to change approximately 10 min after the observation started, quantitatively indicating the effect of phototoxicity. By contrast, when the images were acquired with minimal laser intensity and Enhance.ai was used, mitochondria length remained constant throughout the 120 min of observation (Fig. 6).

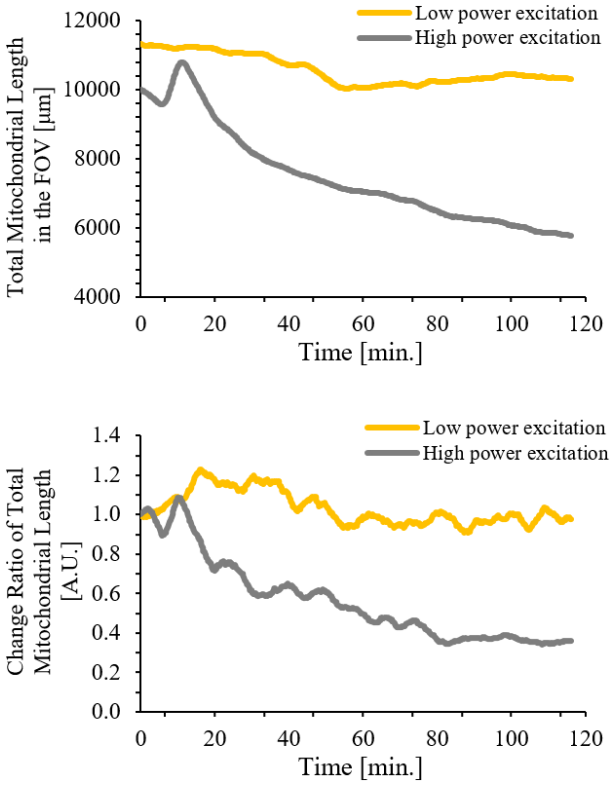

Fig. 6 Quantification of changes in mitochondrial morphology over time

Graph showing the change in total mitochondrial length [μm] (top) and the rate of change of the total mitochondrial length [A.U.] in the field of view. Enhance.ai was used for the images acquired with low-power fluorescence excitation (yellow) and high-power fluorescence excitation (gray). The time interval is 10 s.

These results show that the Enhance.ai function can be used to avoid the effects of phototoxicity on mitochondria and to analyze their morphology quantitatively.

Overall, Enhance.ai is an effective tool for assessing mitochondrial quality over extended periods of time and for analyzing the detailed dynamics of mitochondria and related molecules. We expect it to be used in basic research on mitochondria and drug discovery.

4 Other Examples of Application of AI Functions to Mitochondrial Analysis

Clarify.ai, a function of NIS.ai, is an image quality improvement function that removes out-of-focus fluorescence without training.

Compared to the images captured with a confocal microscope, images acquired with a CMOS camera using a conventional epifluorescence microscope may blur owing to the leakage of fluorescence from outside the focus. Mitochondria are extended and distributed not only in the XY direction but also in the Z direction in the cell, which can cause

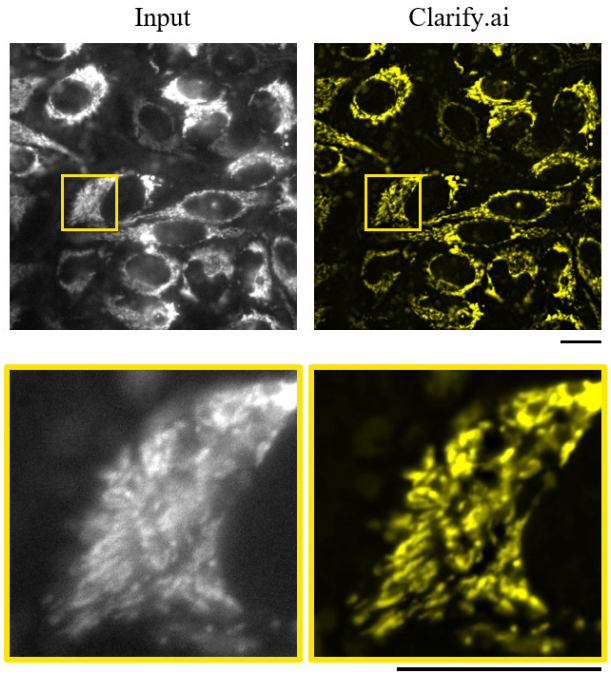

Fig. 7 Mitochondrial fluorescence image sharpening using Clarify.ai
Input: An image with severe out-of-focus light leakage.
Clarify.ai: Inference results using Clarify.ai. The lower panel shows the enlarged image of the yellow rectangle in the upper panel. Scale bars are 20 μm.

leakage of fluorescence from outside the focus. When mitochondria images containing multiple out-of-focus fluorescent components are acquired, it is difficult to accurately detect mitochondria regions through image processing. By inputting such images to Clarify.ai, clear, in-focus images can be obtained (Fig. 7). This makes it possible to detect and quantify mitochondrial regions without using microscopic observation methods with high Z-resolution, such as confocal microscopy.

Additionally, NIS.ai has a Segment.ai function that directly extracts target regions from image input and a Convert.ai function that can be used to output fluorescent images from unstained image input.

By training from fluorescent images and hand-drawn extraction regions, e.g., Segment.ai enables the extraction of complex morphological structures, such as mitochondria, without utilizing advanced image analysis techniques (Fig. 8). Additionally, by training Convert.ai with a set of bright-field images and fluorescence images, it is possible to generate fluorescence images from bright-field images of label-free specimens (Fig. 9). Although such digital staining techniques are not suitable for all specimens and target intracellular structures [5], they can reduce phototoxicity and eliminate toxicity caused by staining reagents in applicable specimens completely.

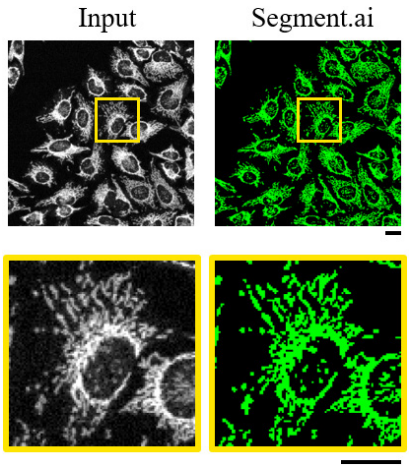

Fig. 8 Detection of mitochondrial regions using Segment.ai
Input: Fluorescence image input to Segment.ai
Segment.ai: Mitochondrial regions detected by Segment.ai.
The lower panel is a magnified image of the yellow square region in the upper panel. Scale bars are 20 μm.

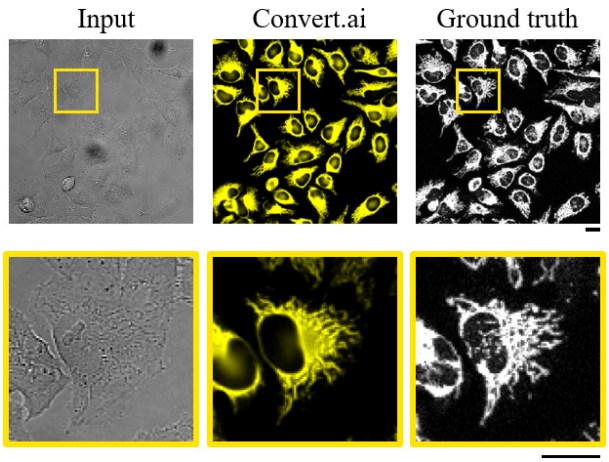

Fig. 9 Mitochondrial fluorescence images generated from transmitted-light images using Convert.ai
Input: Transmitted bright-field image input to Convert.ai. Convert.ai: Mitochondrial fluorescence image generated by Convert.ai. Ground truth: Ground truth fluorescence image. The lower panel is a magnified image of the yellow rectangle in the upper panel. Scale bars are 20 μm.

5 Overview of Materials

The cells, microscopes, and NIS.ai functions used in the experiments described above are summarized in Table 1.

Table 1　Summary of experimental materials

	Fig. 2, 3	Fig. 7	Fig. 8	Fig. 9
Cell	HeLa cells			
Microscope	Eclipse Ti2-E			
Image acquisition	Confocal microscopy (A1R)	Epifluorescence microscopy (CMOS)	Confocal microscopy (A1R)	Confocal microscopy (A1R)
Objective magnification	60x	100x	20x	20x
NIS.ai	Enhance.ai	Clarify.ai	Segment.ai	Convert.ai
Iterations	1000	Without training	1000	1000
Input	Fluorescence	Fluorescence	Fluorescence	Bright-field
Output	Fluorescence	Fluorescence	Detected region	Fluorescence

6 Conclusion

NIS.ai enables high-S/N images to be obtained without strong excitation light irradiation or long exposures. This simplifies performing time-lapse observations and analyses, which would have been difficult using traditional methods over short intervals or extended periods of time. In addition to the example of mitochondria, we expect this technique to be applied to research that requires capturing high-speed phenomena, such as intracellular vesicular transport [6], [7]. Furthermore, as this system can remove light blur from the area beyond the focus area, a problem that has hindered the detection of fine structures, we expect it to help improve the efficiency of the analysis.

References

[1] J. Nunnari and A. Suomalainen, “Mitochondria: in sickness and in health,” *Cell*, vol. 148, pp. 1145–1159, 2012.

[2] K. Mehta, L. A. Chacko, M. K. Chug, S. J. Jhunjhunwala, and V. Ananthanarayanan, “Association of mitochondria with microtubules inhibits mitochondrial fision by precluding assembly of the fission protein Dnm1,” *J. Biol. Chem.*, vol. 294, no. 10, pp. 3385–3396, 2019.

[3] P. P. Laissue, R. A. Alghamdi, P. Tomancak, E. G. Reynaud, and H. Shroff, “Assessing phototoxicity in live fluorescence imaging,” *Nature methods*, vol. 14, no. 7, pp. 657–661, 2017.

[4] M. M. Knight, S. R. Roberts, D. A. Lee, and D. L. Bader, “Live cell imaging using confocal microscopy inducing intracellular calcium transients and cell death,” *Am. J. Physiol. Cell Physiol.*, vol. 284, pp. 1083–1089, 2003.

[5] C. Ounkomol, S. Seshamani, M. M. Maleclar, F. Collman, and G. R. Johnson, “Label-free prediction of three-dimensional fluorescence images from transmitted-light microscopy,” *Nature methods*, vol. 15, pp. 917–920, 2018.

[6] T. Tojima, Y. Suda, M. Ishii, K. Kurokawa, and A. Nakano, “Spatiotemporal dissection of the *trans*-Goldi network in budding yeast,” *J. of Cell Science*, vol. 132, no. 15, jcs231159, 2019.

[7] M. Rosendale and D. Perrais, “Imaging in focus: Imaging the dynamics of endocytosis,” *Int. J. of Biochem. and Cell Biol.*, vol. 93, pp. 41–45, 2017.

門井宏平　Kohei KADOI
ヘルスケア事業部 技術統括部 システム開発部
System Development Department
Technology Solution Sector
Healthcare Business Unit

武居俊輔　Shunsuke TAKEI
ヘルスケア事業部 技術統括部 システム開発部
System Development Department
Technology Solution Sector
Healthcare Business Unit

研究開発論文

Research and Development Reports

発電用ガスタービン実験機の翼への最適リブレット効果予測と，そのレーザー加工によるリブレット性能評価†

白石雅之，土橋晋太郎，Peter A. Leitl，Andreas Flanschger，Stefan Schreck，
Richard Benauer，Simon Pramstrahler，Andreas Marn

Numerical and Experimental Investigation of Laser Processed Riblets on Turbine Exit Guide Vanes of Gas Turbine Test Rig and the Impact on the Performance

Masayuki SHIRAISHI, Shintaro TSUCHIHASHI, Peter A. LEITL, Andreas FLANSCHGER,
Stefan SCHRECK, Richard BENAUER, Simon PRAMSTRAHLER and Andreas MARN

リブレットは，流体機器の表面に設けられたサメ肌状の構造で流線に沿った溝により乱流境界層の粘性抵抗を低減することが知られている．低圧の発電用ガスタービンを模した実験評価機において，タービン出口案内翼（TEGV）の負圧面にリブレットを施した場合の圧損や wake の低減を流体解析により求め，流体力学上最適なリブレットデザインを算出した．実際に鉄系ブレードである出口案内翼に直接レーザー加工でデザインを忠実に再現したリブレットを形成し，実験評価機に設置してリブレットの効果や流れへの影響を実測した．出口案内翼で6.3%の圧損低減が得られた．レーザー加工は金属に直接リブレットを加工できるので，発電用ガスタービンのような高温環境でもリブレットを適用でき，発電効率向上などに寄与することができる．

The reduction of pressure loss and wake in a low-pressure turbine test rig containing turbine exit guide vanes (TEGVs) with laser-processed riblet surface were numerically and experimentally investigated. Riblets are streamwise grooved surfaces which reduce the viscous drag in a turbulent boundary layer, similar to shark-skin. An optimized riblet design was calculated by computational fluid dynamics (CFD), and the designed riblets were laser-processed directly onto the suction side of steel TEGVs. The TEGVs with and without riblets were installed on the test rig, and the effect of the riblets on the flow were measured. Pressure loss around the TEGVs was reduced by 6.3%. This result shows the benefit of laser-processed riblets directly fabricated on 3-dimensionally curved parts, such as gas turbine blades, which operate at high temperature.

Key words リブレット，レーザー加工，流体解析，粘性抵抗低減，発電効率
riblet, laser processing, CFD, drag reduction, power generation efficiency

1 はじめに

発電用ガスタービンをはじめとする流体機器が受ける流体抵抗は，圧力抵抗（慣性抵抗）と摩擦抵抗（粘性抵抗）に大別される．特に高レイノルズ数の乱流領域においては，壁面境界層に強いヘアピン渦が発生し，それに伴って壁面ごく近傍に低速ストリークとよばれる構造によって連続的に縦渦が生じ，層流に比べて大きな壁面乱流摩擦抵抗が発生する［2］．摩擦抵抗は流体機器の損失の一因であり，これを低減することは流体機器の効率を向上させる大きな課題の１つである．

一方，速く泳ぐ種のサメにおいて鱗の１つ１つの表面に35～100 μm 程度の微小な縦溝があることが知られていた［3］，［4］．流れに沿ったこの縦溝はリブレット（riblet）と呼ばれ，平滑面に対して８～10%程度の乱流摩擦抵抗低減を引き起こすことが実験的にも明らかにされている［5］．リブレットは，縦渦が壁面から離れて壁面との相互作用が抑制される効果を持つ［6］．Fig. 1 にリブレットと縦渦の

† 本稿は，自著の引用文献［１］に対して実測と解析の乖離の要因，および実用条件を想定した場合の影響に考察を加えたものである．

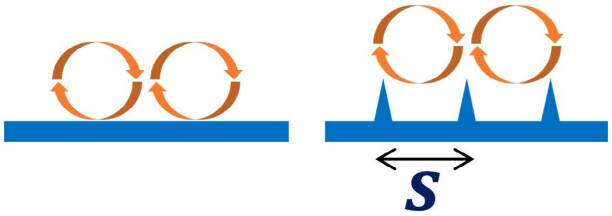

Fig. 1　Eddy-wall interaction without and with riblets. The flow is in the depth direction of the paper.

相互作用の模式図を表す．壁面近傍の縦渦の寸法は壁剪断応力に依存するため，最適なリブレットピッチ（リブレットの嶺トップの間隔）も各所の壁剪断応力に依存し，壁剪断応力が大きいほど最適なリブレットピッチは小さくなる．リブレットによる摩擦抵抗の低減量は縦渦の寸法，すなわち流速によって変化する．リブレットピッチ s を次の式のように無次元化した s^+ という尺度においては，$s^+=17$付近で摩擦抵抗の低減効果が最大となる．

$$s^+ = \frac{s\sqrt{\frac{\tau_w}{\rho}}}{\nu} \tag{1}$$

ここで，τ_w は壁剪断応力，ρ は流体の密度，ν は流体の動粘度である．これより流速が相対的に遅く，もしくはリブレットピッチが小さくなると摩擦抵抗の低減効果はゼロに漸減する．一方，流速が相対的に速く，もしくはリブレットピッチが大きくなると摩擦抵抗の低減効果はゼロを超えて逆に摩擦抵抗が増大する．この挙動を表したものがFig. 2である［7］．とりわけ表面積が大きく高レイノルズ数領域で乱流摩擦抵抗の寄与が大きな航空機や風力タービン翼の分野でリブレットの研究が進んでおり［8］，［9］，産業用コンプレッサーやジェットエンジンなどターボ機械にも有効と考えられている［10］，［11］．

リブレットピッチは数 μm ～100 μm 程度の微小寸法となることから，機械加工によるリブレットの実現は困難であり，従来は金型による樹脂フィルム（リブレットフィルム）が用いられた［12］．しかし，対象物の形状や流線が複雑な場合や使用環境が高温である場合にはフィルムは適用が難しく，特に商用ガスタービンにおいてはフィルムでのリブレットの実用化は不可能であった．

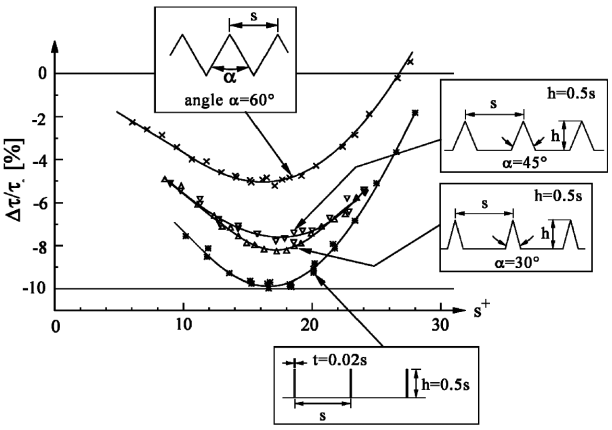

Fig. 2　Drag reduction effect by riblets with various cross section. The number s^+ is a dimensionless riblet size.

そこで我々はレーザーアブレーション加工により所定の形状のリブレットを形成する技術を開発した．レーザーアブレーション（laser ablation）とは，ナノ秒，ピコ秒，フェムト秒のパルス幅を持つ極短パルスレーザーによって非熱的に材料表面の物質を除去する技術である［13］，［14］．この技術と，リブレットの最適寸法を導出し流体への効果を予測する技術［15］とを組み合わせることで，従来リブレットの実現が難しかった複雑形状で高温環境のタービン翼に対して直接リブレットの形成を行うことができる．我々は実際にこうした環境下で運転される金属製のタービン翼に直接，流体解析（CFD）に基づいて設計したリブレットをレーザー加工で形成しており，これまでにタービン実験評価系における出口案内翼（静翼）にリブレットを形成した場合の圧損や流れの変化の評価［1］や，超小型エンジンにおける圧縮機インペラー（動翼），ディフューザー（静翼）およびタービンブレード（動翼）にリブレットを形成した場合の推力や燃料効率のエンジン性能の変化の評価［16］を行い，高温環境におけるタービン部品へのリブレット加工の優位性を示してきた．本稿では，筆者らの評価結果［1］に対して，実測と解析の乖離の要因，および実用条件を想定した場合の影響に考察を加えた．

2　タービン実験評価系概要

リブレットの効果を検証した実験評価系は，オーストリア・グラーツ工科大学（Graz University of Technology, Graz, Austria）の亜音速テストタービン設備（Subsonic Test Turbine Facility for Aerodynamic, Aeroacoustic, and Aeroelastic Investigations; STTF-AAAI）である．Fig. 3 に設備概略を示す［17］．共通コンプレッサー設備より最高温度 100℃，流量 2.5～15 kg/s のエアが供給でき，入口案内翼（IGV）を経て 1 段の低圧タービンステージおよびタービン出口案内翼（TEGV）を通って排気される．タービン動翼の最大回転数は 6300 rpm である．本設備では全圧，全温，静圧，静温，流速，流量，音響の各項目が測定可能である．

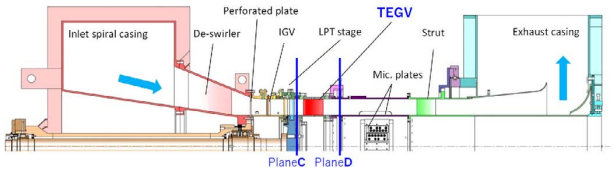

Fig. 3　Experimental turbine test-rig facility of STTF-AAAI and its TEGV section.

今回は，翼が個々に取外し可能でレーザー加工が容易なTEGVをリブレットの効果検証の対象とした．TEGV部は15枚の翼で構成され，翼1枚の概略寸法は翼弦長100 mm×スパン80 mmで材質は一般構造用圧延鋼材SS400である．

3 数値的解析

3.1. 解析の概要

リブレット設計および効果予測はCFDにより導いた[15]．Fig. 4にリブレット設計プロセスの概略を示す．まず，過去の実測評価とコリレーションを取りながら，全ての物体表面にリブレットの無いベースライン解析をmoving mesh（MM）による非定常LES[*1]で行い，これをmixing plane model（MPM）による定常RANS[*2]と比較して妥当性を確認した．リブレット有の解析は，リブレットの微小な形状自体はモデル化せず，別途ミクロな非定常解析によって境界層に与える影響を求めた結果を定常RANSにおける壁表面特性として与えることでリブレットを再現し，乱流モデルにはSST-kωを用いた．

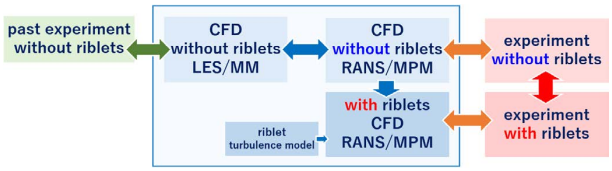

Fig. 4 Scheme of riblet design process and correlation between simulation and experiment.

3.2. 解析条件

解析空間をFig. 5に示す．解析セル数は約680万である．リブレット断面形状はFig. 6に示すような最大8 %の摩擦抵抗低減効果を持つ三角形状のリブレットを仮定し，リブレットの適用箇所はTEGVの負圧面とした．

タービンの運転条件は，動翼の回転数4600 rpm，動作圧95.5 kPa（ゲージ圧），密度は圧縮性流体として扱い，動粘度は温度依存のSutherland則に従うとした．入口では全圧17.9 kPa，全温100℃，流入角度46.25°，出口では静圧0 Paとした．

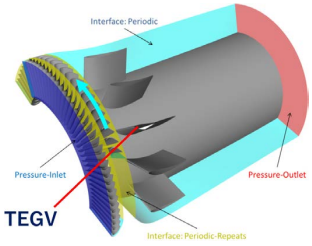

Fig. 5 CFD domain.

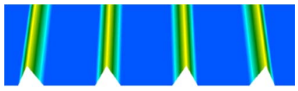

Fig. 6 Assumed riblet cross-section in CFD.

TEGV部の表面積のうち翼面は25.3%を占めており，そのうちリブレットを適用する対象面積は12.4%である．

3.3. ベースライン解析

解析および実測の分布表示はFig. 7のようにTEGV部全周の1/15にあたる一区画の後方視野の扇形で表す．

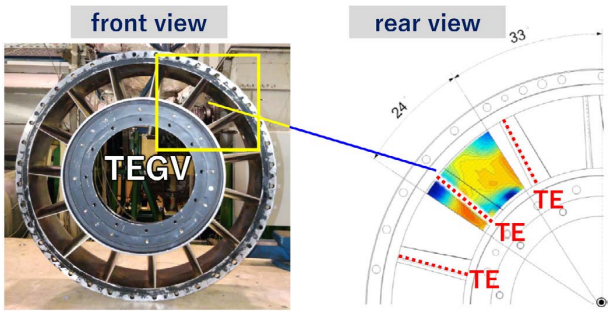

Fig. 7 Display of distribution of physical quantities by a single section of TEGVs. TE is a trailing edge of TEGV.

リブレット無しにおける過去実測値およびベースライン解析（非定常LESおよび定常RANS）の結果をFig. 8に示す．TEGV部前のPlane C位置での全圧分布は過去実測値と非定常LESとは良く似ており，動翼のwakeの影響が明確に分かる．定常RANSは平均化の影響を受けて動翼の影響は消えている．TEGV部後のPlane D位置での全圧分布は，過去実測値，非定常LES，定常RANSいずれもTEGVの翼の後縁部からのwakeの影響が見られ，多少形状は異なるものの同等なwakeが再現された．

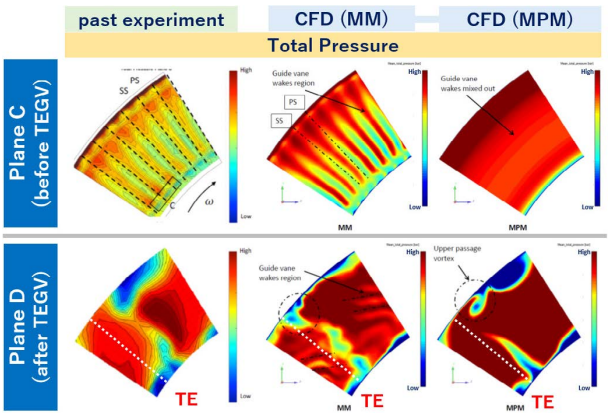

Fig. 8 Comparison of the past experiment and the baseline simulation results without riblets by unsteady-state LES（MM）and steady-state RANS（MPM）.

また，Fig. 9に示すように，全圧，流速，流れのヨー角の径方向分布について定常RANSの結果は過去実測値と絶対値として同等な値が得られた．なお，流れのヨー角は，動翼回転方向（Fig. 5の矢印）に向かう流れの向きを正と

[*1] Large-Eddy Simulation.
[*2] Reynolds-Averaged Navier-Stokes.

した．これらの比較を踏まえ，定常 RANS 結果はリブレット無しのベースラインとして妥当である．

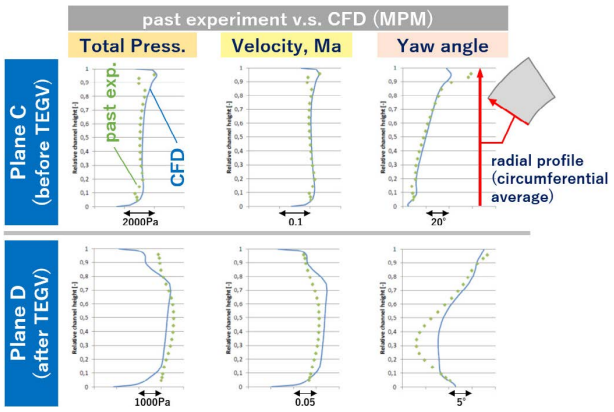

Fig. 9　Validity of the steady-state RANS（MPM）simulation（solid lines）compared to the past experiment（dotted lines）.

3.4. リブレット解析

定常 RANS によるリブレット有無の比較結果を Fig. 10 に示す．径方向分布では，リブレット無しに比べてリブレット有の方が流速については Plane C，Plane D ともに増大しており，全圧については Plane C で減少，Plane D で増大した．リブレット有無での差は僅かではあるが，リブレット有の方が TEGV 部前後の圧損が低減し，流れやすくなることが予測された．

また，TEGV 後の全圧の周方向分布についてリブレット有無を比較すると，Fig. 11 に示すようにリブレット有のほうが wake の幅が減少することが予測された．

これらの解析結果からは，TEGV 部前後の圧損はリブレットにより1.2%低減すると予測された．

3.5. リブレット最適寸法

Fig. 12 に CFD によって導出されたリブレット最適寸法

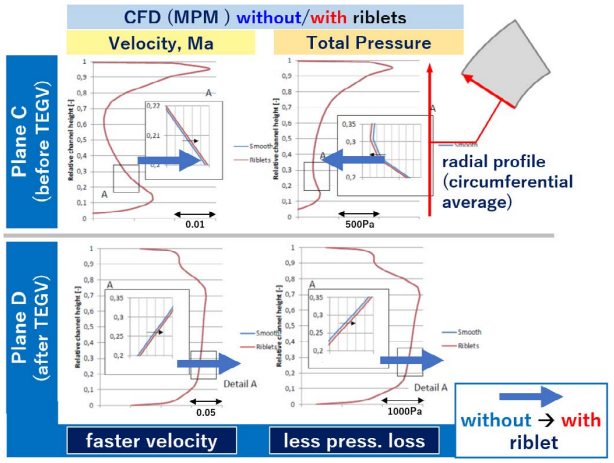

Fig. 10　Comparison of the simulation results without and with riblets by steady-state RANS（MPM）.

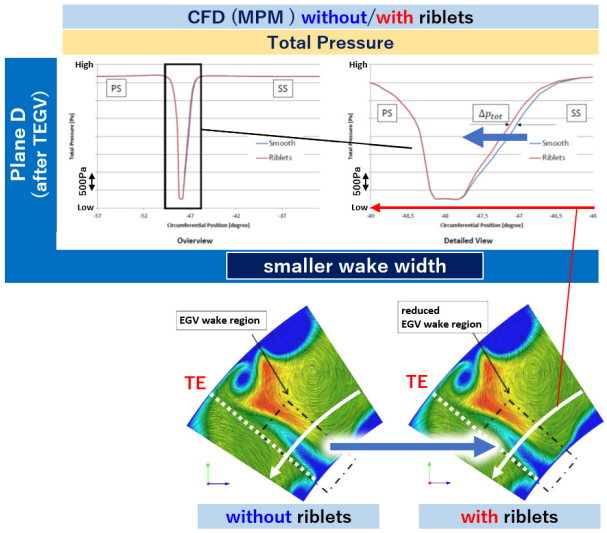

Fig. 11　Simulated wake width without and with riblets.

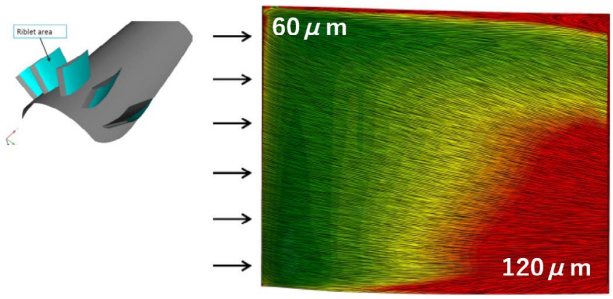

Fig. 12　Riblet design（suction side）obtained by CFD.

を示す．コンターは赤がリブレットピッチが大きく，緑がリブレットピッチが小さい．リブレットピッチは 60～120 μm 程度でゆるやかに分布しており，流線も一様ではない．

4　リブレットのレーザー加工

リブレットの加工にはレーザーアブレーション加工の開発機を用いた．このレーザー加工機は，波長 532 nm（緑色），パルス幅約 15 ps，最大繰返し周波数 4 MHz，最大出力 50 W の短パルスレーザーを持つ．レーザー光は照射ヘッドに導かれ，ガルバノミラーによって同期してスキャンされる．レーザー光は f θ レンズによって所定の位置に集光されるが，湾曲した翼表面に沿って焦点を追随させることができる．照射ヘッドは，3 軸ステージによって所定の XYZ 位置に駆動できる．また，加工対象物は 2 軸の傾斜ステージ上で所定の姿勢を示現できる．レーザー光が集光した対象物の表面はアブレーションにより除去され，これを連続的にスキャンすることでリブレットの溝が形成される．

前節で述べた CFD によるリブレット最適寸法を忠実に再現するため，解析ノードごとのリブレットのピッチと方向の情報から流線に沿ったリブレットのパスを生成した．

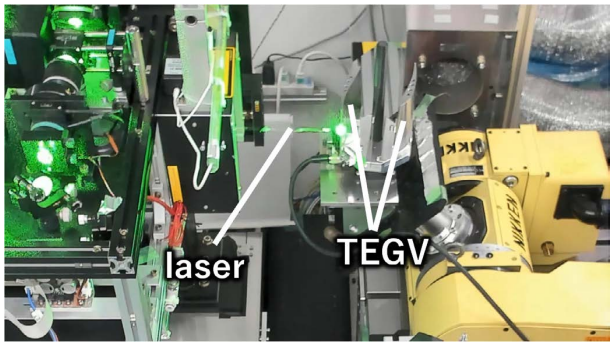

Fig. 13　Laser processing on the surface of TEGV using a development tool with green pulsed laser beam.

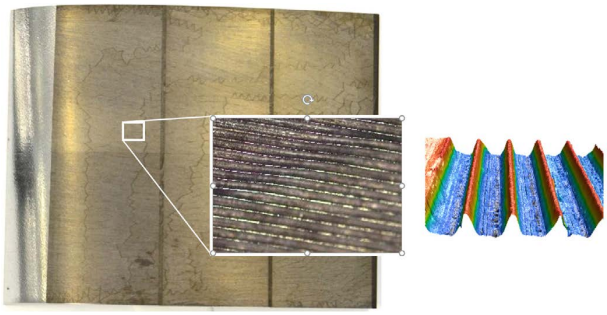

Fig. 14　(left) TEGV (suction side) with lasered riblet. (right) A microscopic profile of lasered riblet sample.

これにより，一様でないリブレットピッチを持つ領域内で，3次元的に計算された流線に沿った曲線上にリブレットを形成できる．Fig. 13 にTEGV の翼へのレーザー加工中の様子を示す．

最終的に15枚の TEGV の負圧面にレーザー加工でリブレットを施した．Fig. 14 にリブレットを施したTEGV の翼の1枚を示す（Fig. 12 のリブレット最適寸法の図と対応する）．TEGV のやや暗い領域にリブレットが加工されている．

5 実測評価

5.1. 評価概要

実験評価機にリブレット無しの翼15枚を設けたテストと，リブレット有の翼15枚を設けたテストとで各々別に測定を実施した．タービンの運転条件は，入口温度97℃，動翼の修正回転数 4042 rpm（CFD における回転数 4600 rpm に相当する），修正流量 6.81 kg/s で，レイノルズ数は約34万である．

流れの評価は5孔プローブによる TEGV 部前後の圧力，温度，流速測定および後縁プローブによる TEGV 後の圧力と流速の測定で行った．Fig. 15 と Fig. 16 に5孔プローブと後縁プローブの配置を，Table 1 に5孔プローブと後縁プローブの測定不確かさを示す．

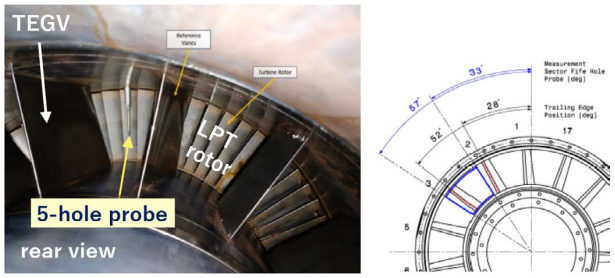

Fig. 15　Configuration of the five-hole probe.

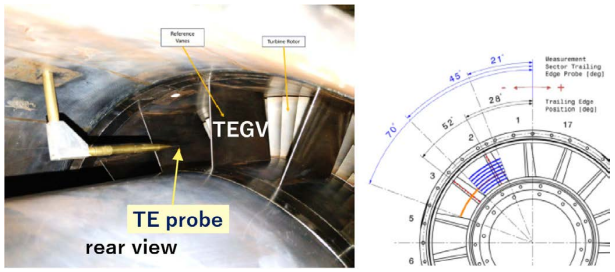

Fig. 16　Configuration of the trailing-edge probe.

Table 1　Measurement uncertainties of the five-hole probe (left) and the trailing-edge probe (right).

Flow variable		Uncertainty, ±
Mach number		0.002
Pressure	total	35 [Pa]
	static	63 [Pa]
Temperature	total	60 [K]
	static	80 [K]
Flow angle	pitch	0.70 [deg]
	yaw	0.70 [deg]
Velocity	absolute	0.90 [m/s]
	axial	0.90 [m/s]
	radial	0.90 [m/s]
	circumferential	0.90 [m/s]

Flow variable		Uncertainty, ±
Pressure	total	28 [Pa]
	static	28 [Pa]
Velocity	absolute	0.60 [m/s]

5.2. 5孔プローブによる流れ評価

TEGV 部前の Plane C および TEGV 部後の Plane D における全圧と流れのヨー角について周方向平均の径プロファイルの測定結果を Fig. 17 に示す．リブレット有の方が TEGV 部前で全圧が低下，TEGV 部後で全圧が上昇したことから，圧損が低減したことが分かった．また，リブレット有の方が TEGV 部前後とも流れのヨー角がゼロに近づいていることが分かった．また，扇形領域内の分布におけるリブレット有無の差異からは，リブレットによって全体的に圧損が減り，流れが軸方向に沿うガイド性が向上したことが分かった．

5.3. 後縁プローブによる Wake 評価

後縁プローブは，所定の径位置において周方向に移動させながら分布を取り，wake の幅を評価できる．Fig. 18 に後縁プローブによる50%スパンでの周方向流速プロファイルの測定結果を示す．リブレット有の方が wake の幅が減少するとともに，より TEGV の翼に沿った流れとなることが分かった．他の径位置においても同様な傾向が測定された．

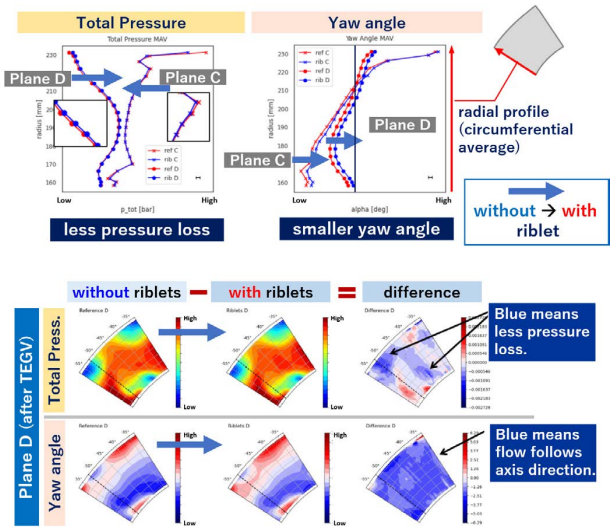

Fig. 17 Difference in total pressure and yaw angle between without and with riblets measured with the five-hole probe.
(top) Radial profile (circumferential average).
(bottom) 2D cross-sectional profile.

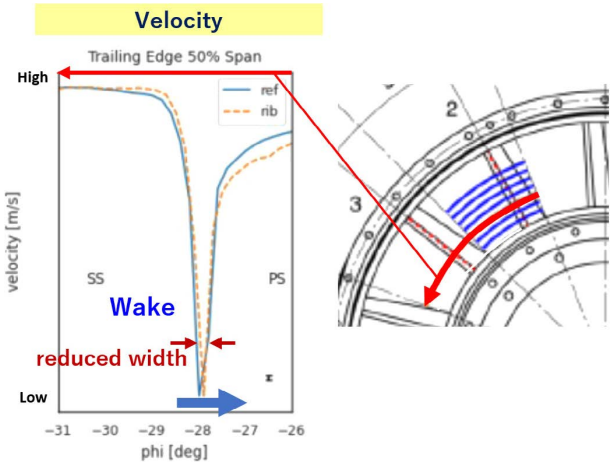

Fig. 18 Difference in velocity profile (wake) between without riblets and with riblets measured by trailing-edge probe.

このことは，負圧面に施したリブレットにより摩擦抵抗が低減して負圧面側の流速が上がることで，Fig. 19 に模式的に示すように後縁で合流した流れにおいて翼後方の流れのヨー角が小さくなって流れを軸方向に向かわせるガイド性が向上したと考えられる．すなわち，リブレットは単に摩擦抵抗を低減させる本質的な効果だけでなく，その結果リブレット適用面に接する流れの流速を増大させ，後流のコントロールをすることも可能ということができる．

5.4. リブレットによる圧損低減効果

これらの測定結果から，TEGV 部前後の圧損を求めた．Table 2 に TEGV 部前後の全圧および圧力損失のリブレット有無での比較を示す．全圧の算出には面積加重平均と質量加重平均がよく用いられ［18］，全圧等流速に関係した物

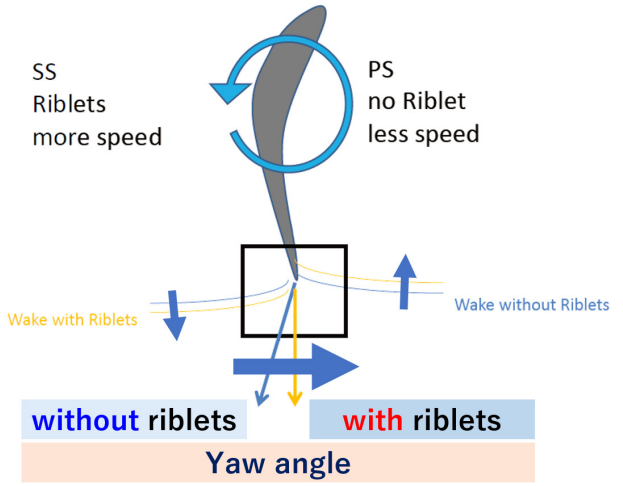

Fig. 19 Schematic concept of assumed effect on the flow velocity and direction by riblets on SS (suction side).

Table 2 Reduction of pressure loss between Plane C (before TEGV) and Plane D (after TEGV) by riblet: (top) Area-weighted, (bottom) Mass-weighted.

Total pressure loss ΔP (PlaneC − PlaneD) [Pa]		reduction of pressure loss
without riblets	677.1	ref
with riblets	634.2	−6.3%

without riblets	640.8	ref
with riblets	595.1	−7.1%

理量では質量加重平均が適するとされるが，圧損低減量は，少なくとも面積加重平均の場合であっても6.3%は低減効果があることが求められた．

6 まとめ

タービン実験評価機の TEGV にリブレットを適用した場合の TEGV 部前後の圧損低減効果および最適なリブレット設計を CFD により求めた．TEGV の負圧面にリブレットを適用することで，圧損は1.2%低減すると効果予測された．リブレット設計に従ってレーザー加工によりリブレットを施した TEGV の翼を実験評価機に設置し，リブレット有無の圧損を実測評価した結果，TEGV 部前後の圧損はリブレットを施すことで6.3%低減された．また，リブレットにより流速向上，ガイド性向上の効果が確認できた．これらにより，リブレットによる流れ制御特性を持った翼として，ガスタービンなどのターボ機器等の翼設計に有用であると考えられる．

一方，TEGV 部前後の圧損低減が CFD 予測よりも実測の方が大きかったのは，リブレット有の場合の CFD 予測が定常 RANS 解析に拠っており，特に TEGV 正圧面側の非定

常な流れにおける剥離が定常 RANS 解析では再現し難いことからリブレットが剥離に与える効果が過少見積となったことが要因の１つとして考えられる．現時点では非定常計算によるリブレット効果予測は計算負荷上の課題があるが，計算能力向上，アルゴリズム改善により，非定常におけるリブレット効果予測精度の向上が図られると考えられる．また，今回評価を行った実験評価機はオフデザインポイントでのタービンの挙動の評価が主眼の設備のため，運転条件において翼上に剥離が発生しており，実測と定常 RANS 解析結果に差異が生じた要因と考えているが，通常，タービンはデザインポイントにおいて剥離が生じない翼形状であるため，実用的なタービンに適用した場合は剥離に起因した実測と解析結果の差異は小さくなり，予測精度は向上すると考えられる．実際，超小型エンジンのブレードにリブレットを形成した評価においては，デザインポイントでの運転で実測と解析はよく一致した［16］．すなわち，発電用ガスタービンを対象としてリブレットを適用した場合には，実用的な予測精度でリブレットによる効率向上を予測し，また実際にリブレットを形成して効率を向上することができる．

引　用　文　献

［1］白石雅之，土橋晋太郎，一ノ瀬剛，柴崎祐一，P. A. Leitl, A. Flanschger, S. Schreck, R. Benauer, S. Pramstrahler and A. Marn,“タービンテストリグ出口案内翼への最適リブレット効果予測と，そのレーザー加工によるリブレット性能評価，”第49回日本ガスタービン学会定期講演会，A-24, 2021.

［2］三宅裕，“壁乱流の渦，”*ながれ*，vol. 22, no. 1, pp. 29–34, 2003.

［3］鈴木雄二，笠木伸英，“壁面乱流の知的能動制御，”セーブメーション・レビュー　マイクロフローセンサ特集号（2001），pp. 50–57, 2001.

［4］D. W. Bechert, G. Hoppe and W.-E. Reif, “On the drag reduction of shark skin,” in *Proc. 23rd Aerospace Sciences Meeting*, 1985, doi: 10.2514/6.1985–546.

［5］D. W. Bechert, M. Bartenwerfer, G. Hoppe and W.-E. Reif, “Drag reduction mechanisms derived from shark skin,” in *Proc. 15th Congr. ICAS*, Sep.1986, pp. 1044–1068.

［6］B. Dean and B. Bhushan, “Shark-skin surfaces for fluid-drag reduction in turbulent flow: A Review,” *Phil. Trans. Roy. Soc. A*, vol. 368, no. 1929, pp. 4775–4806, 2010.

［7］D. W. Bechert, M. Bruse, W. Hage, J. G. T. van der Hoeven and G. Hoppe, “Experiments on drag-reducing surfaces and their optimization with an adjustable geometry,” *J. Fluid Mech*., vol. 338, pp. 59–87, 1997.

［8］“戦略的省エネルギー技術革新プログラム　省エネルギー技術開発事業の重要技術に係る周辺技術・関連課題の研究　革新的リブレットによる高速移動体の省エネルギー化技術の調査研究，”成果報告書　2018年３月，NEDO，https://www.nedo.go.jp/library/seika/shosai_201803/20180000000035.html, 2018.

［9］P. A. Leitl, V. Stenzel, A. Flanschger, H. Kordy, C. Feichtinger, Y. Kowalik, S. Schreck and D. Stübing, “Riblet surfaces for improvement of efficiency of wind turbines,” in *Proc. AIAA Scitech 2020 Forum*, 2020, doi: 10.2514/6.2020–0308.

［10］P. A. Leitl, E. Göttlich, A. Flanschger, A. Peters, C. Feichtinger, A. Marn and B. Reschenhofer, “Numerical investigation of optimal riblet size for TCF strut flow and their impact on the performance”, in *Proc. AIAA Scitech 2020 Forum*, 2020, doi: 10.2514/6.2020–0307.

［11］P. A. Leitl, M. L. Garcia De Albeniz and A. Flanschger, “Nano- and microstructured riblet surfaces for centrifugal industrial compressors,” in *Proc. Conf. SUstainable PolyEnergy Generation and HaRvesting*（*SUPEHR*）, 2019, pp. 32–38.

［12］A. Sareen, R. W. Deters, S. P. Henry and M. S. Selig, “Drag reduction using riblet film applied to airfoils for wind turbines,” in *Proc. 49th AIAA Aerospace Sciences Meeting including the New Horizons Forum and Aerospace Exposition*, 2011, doi: 10.2514/6.2011–558.

［13］B. N. Chichkov, C. Momma, S. Nolte, F. von Alvensleben and A. Tünnermann, “Femtosecond, picosecond, and nanosecond laser ablation of solids,” *Appl. Phys. A*, vol. 63, no. 2, pp. 109–115, 1996.

［14］M. C. Richardson, “New opportunities with intense ultrashort-pulse lasers,” in *Proc. of SPIE*, vol. 1410, 1991.

［15］P. A. Leitl, S. Kuntzagk, A. Flanschger and K. Pfingsten, “Experimental and numerical investigation of the reduction in skin friction due to riblets applied on the surface of a Taylor-Couette cell,” in *Proc. of AIAA SciTech Forum*, 2018.

［16］稲崎慎也，佐藤真路，一ノ瀬剛，P. A. Leitl，A. Flanschger，S. Schreck and R. Benauer，“超小型ジェットエンジンの最適リブレット計算とそのレーザ加工，およびエンジン性能での効果検証，”第49回日本ガスタービン学会定期講演会，A-25, 2021.

［17］M. Zenz, A. Hafizovic, L. Simonassi, P. A. Leitl, R. Benauer, F. Heitmeir and A. Marn, “Aerodynamical and aeroelastic investigations of a riblet design applied on the surface of turbine exit guide vanes of a low pressure turbine,” in *Proc. of 13th European Conference on Turbomachinery Fluid Dynamics and Thermodynamics*, 2019.

［18］N. A. Cumpsty and J. H. Horlock, “Averaging nonuniform flow for a purpose,” *J. Turbomach.*, vol. 128, no. 1. pp. 12–129, 2006.

白石雅之　Masayuki SHIRAISHI
次世代プロジェクト本部 第二開発部
2nd Development Department
Next Generation Project Division

土橋晋太郎　Shintaro TSUCHIHASHI
次世代プロジェクト本部 第二開発部
2nd Development Department
Next Generation Project Division

Peter A. LEITL
Bionic Surface Technologies 社
Bionic Surface Technologies, GmbH

Andreas FLANSCHGER
Bionic Surface Technologies 社
Bionic Surface Technologies, GmbH

Stefan SCHRECK
Bionic Surface Technologies 社
Bionic Surface Technologies, GmbH

Richard BENAUER
Bionic Surface Technologies 社
Bionic Surface Technologies, GmbH

Simon PRAMSTRAHLER
グラーツ工科大学
Graz University of Technology

Andreas MARN
グラーツ工科大学
Graz University of Technology


白石雅之
Masayuki SHIRAISHI


土橋晋太郎
Shintaro TSUCHIHASHI


Peter A. LEITL


Andreas FLANSCHGER


Stefan SCHRECK


Richard BENAUER


Simon PRAMSTRAHLER


Andreas MARN

超小型ジェットエンジンの最適リブレット計算とそのレーザー加工，およびエンジン性能での効果検証†

稲崎慎也，Peter A. Leitl，Andreas Flanschger，Stefan Schreck，Richard Benauer

Numerical and Experimental Investigation of Laser Processed Riblets on Ultra-small Jet Engines and the Impact on the Performance

Shinya INASAKI, Peter A. LEITL, Andreas FLANSCHGER, Stefan SCHRECK and Richard BENAUER

リブレットとは，乱流境界層における粘性抵抗を低減する，サメ肌状の流線形の溝面である．超小型ジェットエンジンのコンプレッサー，ディフューザー，タービンブレードにリブレットを形成し，エンジン性能の向上を実験的に確認した．まず，エンジンの３次元モデルを用いた数値流体力学（CFD）により，エンジン性能向上に最適なリブレットデザインを算出し，その性能向上量はエンジン推力で1.81%向上を予測した．算出したリブレットデザインを，直接のレーザー加工によってデザインを忠実に再現するようにエンジン部品に形成した．この部品をエンジンに組み込み，エンジン性能を実測し，レーザー加工されたリブレットはエンジン推力を1.44%向上させるとの結果が得られた．本研究は，高温・高速回転する部品にレーザー加工リブレットを適用し，ターボ機械の性能を向上させた世界初の実験的実証となる．

Riblets are streamwise grooved surfaces which reduce the viscous drag in a turbulent boundary layer, similar to shark skin. We experimentally confirmed improved engine performance by forming riblets on the compressor, diffuser, and turbine blades of an ultra-small jet engine. The optimum riblet design was calculated by computational fluid dynamics (CFD) using a 3D model of the engine, and the improvement was predicted to be 1.81% in engine thrust. The calculated riblet design was formed on the actual parts by laser ablation. It was experimentally confirmed that the laser processed riblets improved engine thrust by 1.44%. This work is the world's first experimental demonstration of improved turbomachinery performance through the application of laser processed riblets on parts exposed to high temperatures and rotating at high speed.

Key words 超小型ジェットエンジン，コンプレッサー，ディフューザー，タービン，推力，効率，リブレット，レーザー加工，粘性抵抗低減，流体解析
ultra-small jet engine, compressors, diffuser, turbine, thrust, efficiency, riblet, laser processing, drag reduction, CFD

1 はじめに

ガスタービンやジェットエンジンなどターボ機器の燃料消費削減や温室効果ガス排出抑制といった経済性や環境性に対する要求が高まっており，ターボ機器の効率改善は社会的にも重要になっている．効率改善手段として，我々は流体抵抗の低減に着目した．流体抵抗は，圧力抵抗（慣性抵抗）と摩擦抵抗（粘性抵抗）に大別される．壁近傍層では，縦渦と呼ばれる乱流要素渦があり，特に高レイノルズ数の乱流領域においては，渦が壁に向かう強い衝撃流を作り，層流に比べて大きな壁面乱流摩擦抵抗が発生する［2］．摩擦抵抗は流体機器の効率低下の一因であり，これを低減することは流体機器の効率を向上させる重要な課題のひとつである．

一方，サメの中でも早く泳ぐ種類においては，鱗１つ１つの表面に 35～100 μm 程度の微小な縦溝があることが知られている［3］，［4］．このサメの鱗の溝はリブレット（riblet）と呼ばれ，平滑面に対して最大８～10%程度の乱流摩擦抵抗低減を引き起こすことが実験的にも明らかにされている［5］．

実用に向けた研究としては，とりわけ表面積が大きく高レイノルズ数領域で乱流摩擦抵抗の寄与が大きな航空機や

† 本稿は，著者らの引用文献［1］に対し，タービン翼のエンジン稼働時温度や稼働時間の結果，および金属疲労についての考察を加えたものである．

風力タービン翼の分野でリブレットの研究が進んでおり［6］，［7］，産業用コンプレッサーやジェットエンジンなどターボ機械にも有効と考えられている［8］，［9］．ただ，これらの機器の最適リブレットは，ピッチが数 μm ～100 μm の微小寸法となることから，機械加工による壁面へ直接のリブレット付与は実現困難であり，従来は金型による樹脂フィルム（リブレットフィルム）が用いられた［10］．しかし，対象物の形状や流線が複雑であったり使用環境が高温である場合，また高速で回転する動体である場合にはフィルムの適用が難しく，商用ガスタービンやジェットエンジンなどにおいてはリブレットの実用化は困難であった．

そこで我々はレーザーアブレーション加工により所定の形状のリブレットを形成する技術を開発した．レーザーアブレーション（laser ablation）とは，ナノ秒，ピコ秒，フェムト秒のパルス幅を持つ極短パルスレーザーによって非熱的に材料表面の物質を除去する技術である［11］，［12］．この技術と，リブレットの最適寸法を導出し流体への効果を予測する技術［13］とを組み合わせることで，従来リブレットの実現が難しかった複雑な形状で高温環境，高速で回転するタービン翼に対して直接リブレットの形成を行うことが可能である．我々は実際に，超小型ジェットエンジンのタービン翼（動翼）に加えて，同様に複雑な形状で高速動体のコンプレッサー（動翼），ディフューザー（静翼）の 3 部品にリブレットを施し，その効果をエンジン性能の改善，効率の改善として示してきた［1］．

一方，材料表面にリブレットのような切欠きを形成すると，材料の強度特性の低下が懸念される．これに対し我々は，圧縮機の部材に直接リブレット加工を施した試験片を準備し，引張試験，クリープ試験を実施し，部材への直接のリブレット加工が，金属の強度特性に影響が無いことを示してきた［14］．本稿は，著者らの評価結果［1］に対し，タービン翼のエンジン稼働時温度や稼働時間の結果，および金属疲労についての考察を加えたものである．

2 評価系概要

2.1. 超小型ジェットエンジン JB220

リブレットの効果を検証した超小型ジェットエンジンは，JB220（Behotec, Dahau, Germany）である Fig. 1 に形状の概略を示す．エアインテークから吸気し，遠心型動翼のコンプレッサー，静翼のディフューザー，燃焼室，静翼の Nozzle guide Vane を経て，動翼のタービン，テールコーンから排気される．動翼部の最大回転数は 12万 rpm で，最大推力は 220 N である．

燃焼機部の外形直径は約 11.3 cm で，全長は 31.3 cm である．コンプレッサーの羽根車径は約 8 cm で，回転軸方向厚みは約 3 cm，羽根は14枚．ディフューザーの直径は約 11 cm で，回転軸方向厚みは約 2 cm．タービンの羽根車径は約 7 cm で，軸方向厚みは約 1 cm，羽根は23枚である．材質は，コンプレッサー，ディフューザーがアルミ系合金で，タービンのみインコネルである．

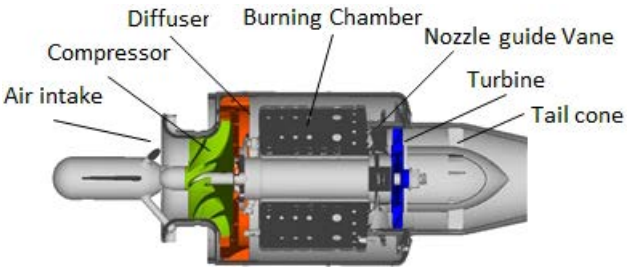

Fig. 1　Ultra-small Jet engine configuration

2.2. エンジン評価ベンチ

エンジン性能評価および，リブレット最適化計算に必要なデータ取得のため，エンジン評価ベンチをフォックスコーポレーション，日本と共同で作成した．評価ベンチの概要模式図を Fig. 2 に示す．

本評価ベンチは，エンジン本体，エンジン性能計測部，エンジン内部温度・圧力計測部，外部環境計測部から構成されている．エンジン本体と性能計測部および内部温度・圧力計測部は室内に設置され，吸入空気は，外部環境空気をそのまま使用している．外部環境計測部は，この外部環境の温度および気圧を計測するものである．

エンジン本体は，前節の JB220である．エンジン性能計測部として推力計，回転計，燃料流量計，風速計を配置している．吸気流量管理のため，エンジンのエアインテーク前に内径 11.4 cm の筒を配置し，この筒を通じてエンジンに吸気するよう接続している．推力計測のため，エンジン

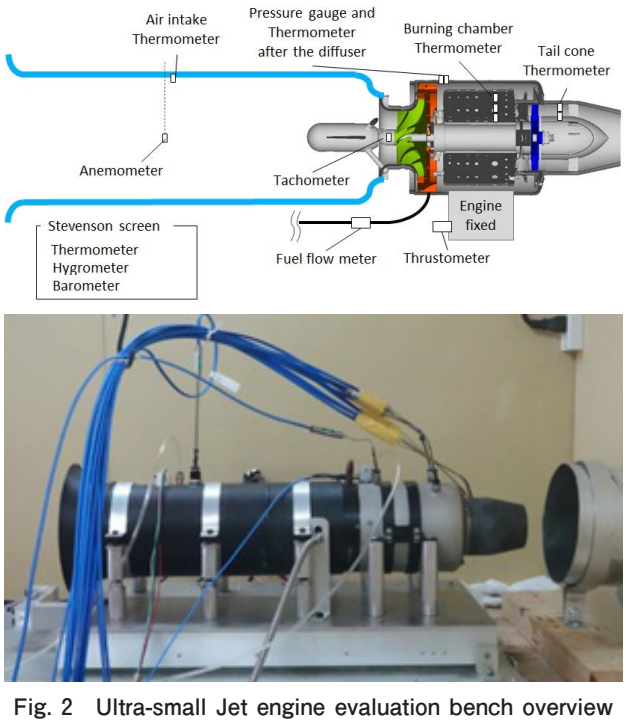

Fig. 2　Ultra-small Jet engine evaluation bench overview

は2本の円径マウンターで固定されている．エンジン内部温度・圧力計測部は，吸入空気の温度，コンプレッサー後の温度・圧力，燃焼室内温度，テールコーン部温度を計測しており，エンジン内部に各センサを配置している．外部環境計測部は，温度，湿度，気圧を百葉箱内で計測している．これらの計測器はすべて1つのデータロガーに接続し，サンプリング周期0.5秒で値を記録している．

3 数値的解析

3.1. 解析の概要

リブレット設計および効果予測は流体解析（CFD）により導いた．Fig. 3 にリブレット設計プロセスの概略を示す．まず，実測評価とコリレーションを取りながら，全ての物体表面にリブレットの無いベースライン解析を moving mesh（MM）による非定常 LES（Large-Eddy Simulation）で行い，次いで mixing plane model（MPM）による定常 RANS（Reynolds-Averaged Navier-Stokes）と比較して妥当性を確認した．リブレットが有る解析は，リブレットの微小な形状自体はモデル化せず，別途ミクロな非定常解析によって境界層に与える影響を求めた結果を，定常 RANS における壁表面特性として与えることでリブレットを再現した．リブレット有無の比較と効果予測は，定常 RANS の範囲内で行った．

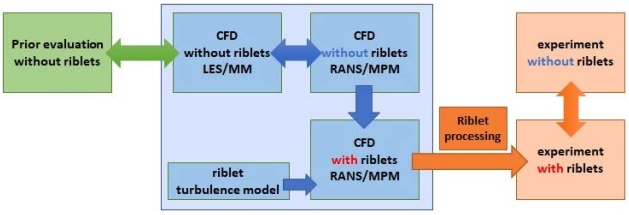

Fig. 3 Scheme of riblet design process and correlation between simulation and experiment

3.2. 解析条件

解析メッシュは約950万である．リブレット断面形状は Fig. 4 に示すような最大 8 %の摩擦抵抗低減効果を持つ三角形状のリブレットを仮定し，リブレットの適用箇所はコンプレッサー，ディフューザー，タービン翼，およびタービンのプラットフォームとし，3部品ともにシュラウド部には未適用とした．

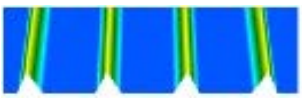

Fig. 4 Assumed riblet cross-section in CFD

エンジンの運転条件は，事前評価の取得条件，実測結果に即しており，回転数 80,624 rpm，密度は圧縮性流体として扱い，動粘度は温度依存の Sutherland 則に従うとした．それ以外の主要な解析条件は，エンジン空気流入量 0.21853 kg/s，同全温 299.45 K，同全圧 1018.10 hPa，タービン動翼への Gas 流入量 0.22368 kg/s，同全温 985.4 K，同流入角度34.54°，エンジン出口側の全温 299.45 K，同全圧 1018.10 hPa とした．

3.3. ベースライン解析

前節の解析条件を用いた非定常 LES が，実測結果と一致しているかを確認した．ディフューザー後の温度は，実測 382.15 K，シミュレーション 377.86 K となっており，良く一致している．また，タービン後の温度についても，実測の平均値 912.66 K と計測バラつき ±13.19 K の範囲にシミュレーション値は分布しており，こちらも良く一致している．これらのことから，実測結果と非定常 LES は良く一致していると言える．

次に，非定常 LES と定常 RANS の結果が一致するか確認した結果を Fig. 5 に示す．エンジンパフォーマンスで最大約 6 %の差，空力性能で最大約 3 %の差が出ているが，全体としては良く一致している．定常 RANS 結果はリブレット無しのベースラインとして妥当である．

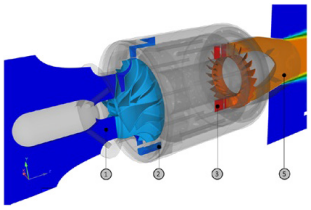

	LES / MM	RANS / MPM	Delta
Power Compressor [kW]	17.752	16.673	- 6.07%
Power Turbine [kW]	18.777	18.318	- 2.44%
BC Efficiency [%]	94.8	97.8	+ 3.16%
Mass flow rate 5[kg/s]	0.22368	0.22368	
Thrust [N]	56.92	58.79	+ 3.28%
Total temperature 2 [K]	377.86	374.78	- 0.82%
Total temperature 5 [K]	917.25	915.99	- 0.14%
Total pressure 2 [Pa]	185186	179469	- 3.09%
Total pressure 3 [Pa]	175608	175569	- 0.02%
η_{ts} [%]	71.0	69.7	- 1.82%
η_{ts} [%]	73.4	75.1	+ 2.33%

Fig. 5 Baseline simulation results without riblets by unsteady LES（MM）and steady RANS（MPM）

3.4. リブレット最適寸法とリブレットの効果予測

Fig. 6 に CFD によって導出されたリブレット最適寸法のコンターを示す．コンターは赤がリブレットピッチが広く，青がリブレットピッチが狭い．

コンプレッサーとディフューザーのリブレットピッチは 10～100 μm 程度で，15～30 μm のピッチが半数以上を占める．ブレード内の分布としては，周速度の早いエッジ付近のリブレットピッチが狭い傾向がある．

タービンのリブレットピッチは，35～120 μm 程度である．翼腹側（正圧面，燃焼器側）は 40～60 μm のピッチが半数以上を占めるが，背側（負圧面，テールコーン側）はブレード根元に広いピッチが多く分布しており，45～120 μm 程度でほぼ均一に分布している．

これらのリブレットを適用した際のエンジン性能の改善は，回転数 80,624 rpm，エンジン吸気量不変の条件において，3部品ともリブレットを付与した場合，推力が1.81%改善，燃料消費量はほぼ変化無しとの予測を得た．

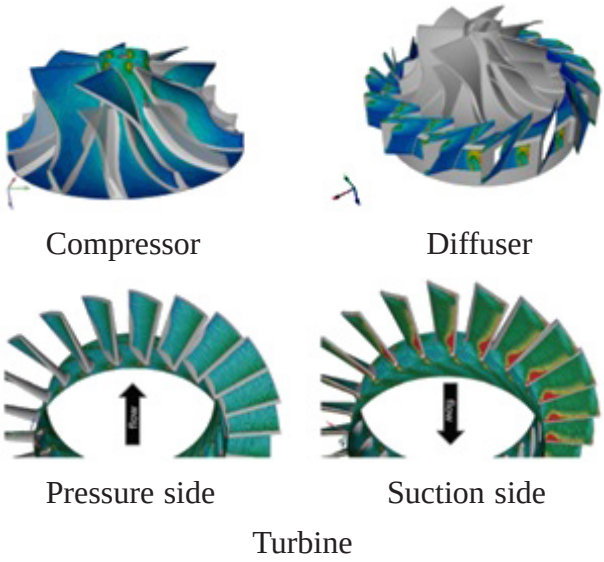

Fig. 6　Riblet design obtained by CFD

4　リブレットのレーザー加工

4.1. レーザー加工の概要

リブレットの加工にはレーザーアブレーション加工の開発機を用いた．この模式図を Fig. 7 に示す．このレーザー加工機は，波長 532 nm（緑色），パルス幅約 15 ps，最大繰返し周波数 4 MHz，最大出力 50 W の短パルスレーザーを持つ．レーザー光は照射ヘッドに導かれ，ガルバノミラーによって同期してスキャンされる．レーザー光は $f\theta$ レンズによって所定の位置に集光されるが，湾曲した翼表面に沿って焦点を追随させることができる．照射ヘッドは 3 軸ステージによって所定の XYZ 位置に駆動でき，また加工対象物は 2 軸の傾斜ステージ上で所定の姿勢を示現できる．レーザー光が集光した対象物の表面はアブレーションにより除去され，これを連続的にスキャンすることでリブレットの溝が形成される．

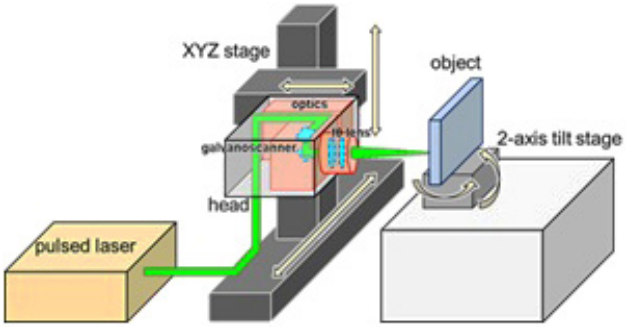

Fig. 7　Overview of riblet processing machine

前節で述べた CFD によるリブレット最適寸法を忠実に再現するため，解析ノードごとのリブレットのピッチと方向の情報から流線に沿ったリブレットのパスを生成した．これにより，一様でないリブレットピッチを持つ領域内で，3 次元的に計算された流線に沿った曲線上にリブレットを形成できる．

4.2. リブレットの加工結果

最終的にコンプレッサー，ディフューザー，タービンの 3 部品にリブレットのレーザー加工を施した．CFD 条件と同様に，3 部品とも共通して部品外側のシュラウド部は未加工である．

コンプレッサーはブレードの負圧面と正圧面の一部とハブ面の一部に加工を行った．Fig. 8 にリブレットの加工済みのコンプレッサーを示す．見た目の色の濃淡は，リブレットピッチの変化による物である．ブレード間では共通のリブレットデザインを適用しているため，結果として，すべてのブレードで同じ濃淡が描かれている．コンプレッサーブレードはお互いが接近しており，レーザーが照射できない部分があるが，コンプレッサーを傾けるなど可能な限り広い面積に加工を行った．コンプレッサーの空気流路に対するリブレットの加工面積率は約50.3%である．なお，前節の CFD による推力改善予測量1.81%は，上記加工面積にリブレットを付与した場合の予測となっている．

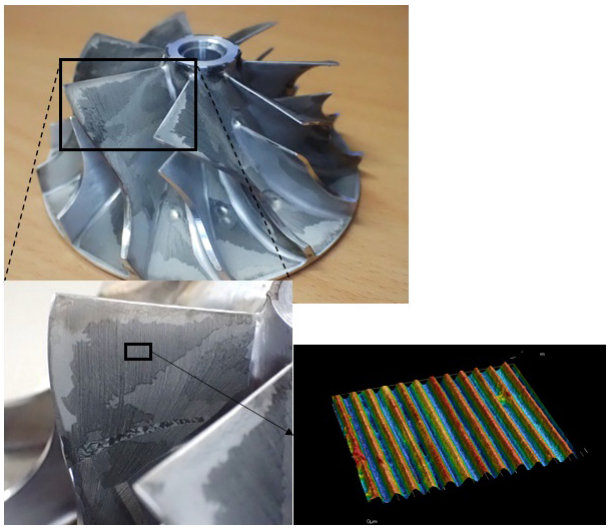

Fig. 8　Compressor with lasered riblet

ディフューザーは15箇所有る空気流路内側に加工を行った．Fig. 9 にリブレットの加工済みのディフューザーを示す．同様に色の濃淡はリブレットピッチの変化によるものであり，同じ濃淡が各流路内に描かれている．ディフューザーの羽根にいくつか存在する穴は，エンジン組み立て用のネジ穴で有り，このネジ部にはリブレットの加工は行ってない．

タービンは，ブレードの腹側（正圧面），背側（負圧面）の両面と，プラットフォームに加工を行った．Fig. 10 にリブレットの加工済みタービンを示す．表面に模様があるように見えているが，模様の入り方はピッチの変化と良く一致しており，これが見えているものと考えられる．前 2 部品と見え方が異なるのは，材質が異なるためと考えられる（前 2 部品はアルミ系合金，タービンはインコネル）．

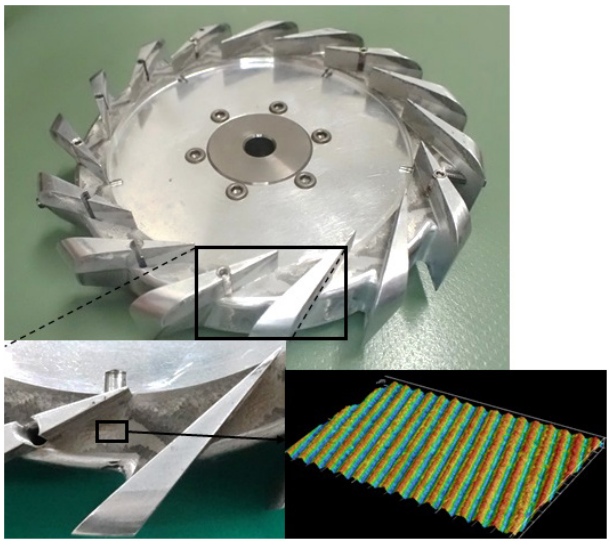

Fig. 9　Diffuser with lasered riblet

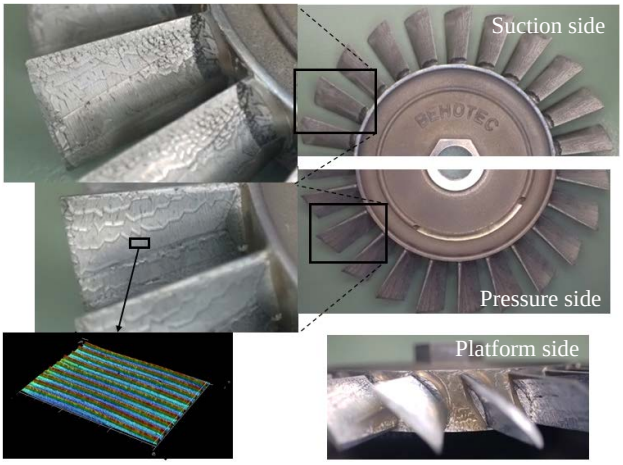

Fig. 10　Turbine with lasered riblet

5 超小型ジェットエンジン実測評価

5.1. 評価方法の概要

エンジン性能の評価は，コンプレッサー，ディフューザー，タービンの 3 部品にリブレットが無い部品とリブレットが有る部品を用意し，同じ日に部品を入れ替える方法で評価を行った．上記 3 部品とタービンに付いているシャフト以外の部品は，燃焼室も含め共通で使用している．なお，これらの交換部品によるエンジン性能の差は，推力，燃料消費量ともに計測再現性以下であることを確認している．また，リブレット有りの評価は，上記 3 部品すべてリブレット有りとする場合のみを評価した．

エンジンの運転条件は CFD 解析条件と同様で，回転数 80,624 rpm，燃料は灯油（JIS K 2203 1号灯油）にシャフトベアリング向け潤滑剤を約 6 %配合した物を使用した．吸入空気は外気をそのまま使用しているため，吸気温度，気圧は時間経過により変動してしまうが，リブレット有り／無しの比較検証実施時の平均値は吸気温度 305.53 k（32.38℃），大気圧 1011.48 hPa であった．

5.2. 温度・気圧変動補正

前節にあるように，吸気は外気をそのまま使用しているため，気温変動，気圧変動によりエンジン性能が変化して計測されてしまう．

そこで，気温，気圧の変動を，標準気温，標準気圧相当に換算可能な以下の計算式を使用し，エンジン性能を比較することにした．エンジン運転時の大気状態を気圧：P，温度：T とし，標準の大気状態を P_0，T_0とし，$\delta = P/P_0$，$\theta = T/T_0$とすると，

$$\text{修正回転数}\quad N_0 = \frac{N}{\sqrt{\theta}} \tag{1}$$

$$\text{修正推力}\quad F_0 = \frac{F}{\delta} \tag{2}$$

$$\text{修正燃料流量}\quad mf_0 = \frac{mf}{\delta\sqrt{\theta}} \tag{3}$$

と表すことが出来る［15］，［16］．

回転数についても，気温，気圧により修正後の回転数は基準回転数では無い回転数となってしまう．これを基準回転数の 80,624 rpm にそろえるため，別途 70,000 rpm と 90,000 rpm の計測データを取得し，推力と回転数の相関から，常に 80,624 rpm 相当に換算する補正を行った．

これらの内容を適用，計算した修正推力と，計測した生データの推力との結果の比較を Fig. 11 に示す．修正前の推力値は約2.8%バラついているが，修正推力の計算後は 0.7%のバラつきに収まっており，修正計算が良く機能していることが解る．

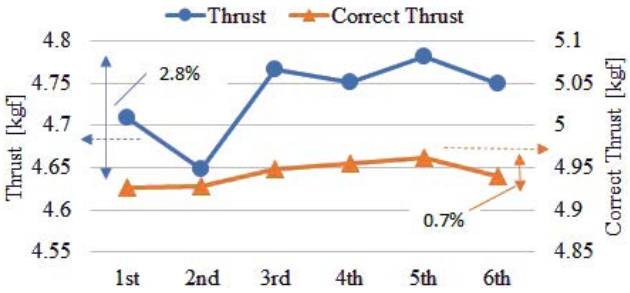

Fig. 11　Verification result of correction calculation

5.3. リブレット付与によるエンジン性能比較

エンジン性能は，修正推力，修正燃料流量，修正燃料効率（＝修正燃料流量／修正推力）の 3 性能で比較を行った．計測再現性確保のため，リブレット有り／無し共に，7 回計測を行っている．

リブレット有り／無しのエンジン性能の比較検証結果を Fig. 12 に示す．修正推力は，7 回計測の平均値で比較すると，リブレット有りが平均1.44%上昇との結果であった．このときの計測再現性は，7 回平均時には3σ 率で0.42%が

期待でき，計測再現性上も優位な差と言える．次に修正燃料流量は，リブレット有りが平均で0.20%消費量が多いとの結果であったが，計測再現性は3σ率で0.34%であり，こちらは優位差無しと判断した．これらから計算した修正燃料効率は，リブレット有りが平均で1.22%効率が良いとの結果で，同様に計測再現性は，3σ率で0.59%が期待でき，こちらは優位差と言える．

上記の値と，CFD 予測を比較した結果を Table 1 に示す．実測値と CFD 予測との差は，修正推力で0.37%，修正燃料効率で0.59%である．修正燃料流量は，実測値が優位差では無く，CFD 予想の“変化無し”との差は無いものと判断した．修正推力および修正燃料効率における，実測値と CFD 予想との差の原因は，リブレットの加工結果が完全な理想形状には成っていないことが考えられる．リブレットの深さや，リブレットの峰頂点のとがり具合など加工形状のさらなる改善を行えば，さらにエンジン性能が改善する可能性もある．全体としては，実測値は CFD 予測と近い結果と考えられる．以上のように，比較検証を行った３性能において，リブレットがエンジン性能，効率を改善しているとの検証結果を得た．

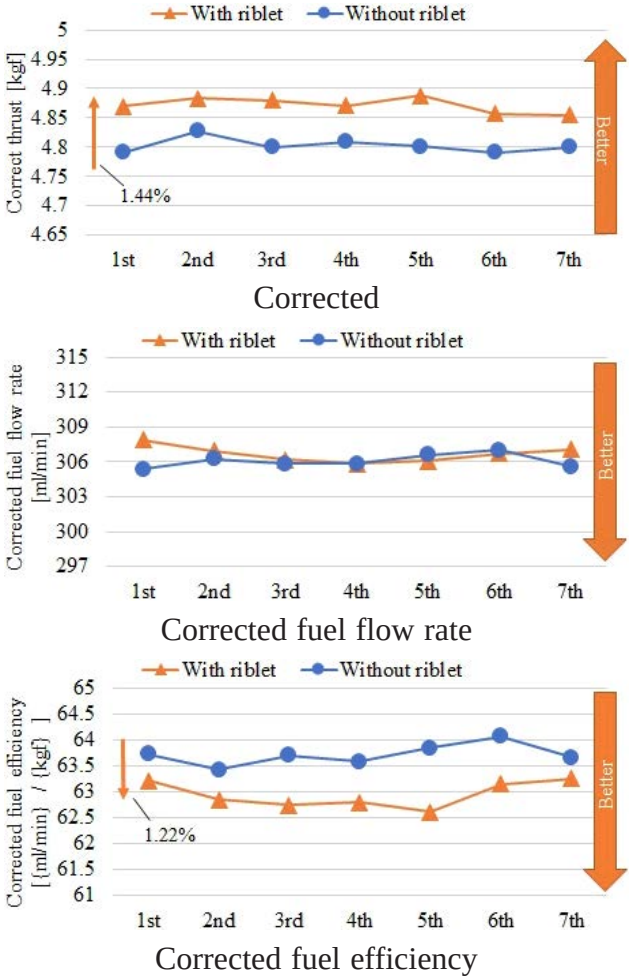

Fig. 12　Results of verification of riblet effect by actual measurement

Table 1　Riblet improvement effect (experimental value, measurement reproducibility, CFD forecast)

	Corrected	Corrected fuel flow rate	Corrected fuel efficiency
CFD	1.81%	0 %	1.81%
Measured value	1.44%	−0.20%	1.22%
Measurement reproducibility 3σ	0.42%	0.34%	0.59%
CFD - Measured value	0.37%	0%	0.59%

6　まとめ

超小型ジェットエンジンのコンプレッサー，ディフューザー，タービンにリブレットを適用した場合の，エンジン推力の改善効果および，最適なリブレット設計を CFD により求めた．上記３部品ともにリブレットを適用した場合には，推力は1.81%上昇すると予測された．リブレット設計に従ってレーザー加工によりリブレットを施したコンプレッサー，ディフューザー，タービンを超小型ジェットエンジンに搭載し，リブレット有無のエンジン性能を実測評価した結果，修正推力は1.44%上昇，修正燃料流量は優位差無し，修正燃料効率は1.22%効率が改善した．これらにより，複雑な形状で高温環境，高速に回転するターボ機器内の部品へ，レーザー加工によりリブレットを形成し，その効果をターボ機器性能の改善として示すことに世界で初めて成功した．

また，本評価の稼働時タービン温度は約800-900℃であり，本稿の効率改善結果は，リブレット付与後トータル８時間以上稼働後の評価結果である．本評価後のリブレットは形状が問題無く維持されていることを確認しており，またこれまで示したように，効率改善も十分確認出来ている．我々が行った母材の強度特性試験では，600℃条件の引張試験，クリープ試験において，リブレット有無では強度特性に差が無いことが確認されており［14］，本稿評価のタービンとは材質，温度，負荷時間などが異なるものの，直接加工のリブレットに強度的な問題がないことは同様の傾向となっている．

これらのことから，高温，回転系の空力部品にリブレットを付与し，ターボ機器の効率を改善する事は，確実に実用化に近づいていると考えられる．

7　謝　辞

本研究の評価データ取りには，（有）フォックスコーポレーション 橋本様，遠藤科学（株）馬塚様に多大なるご協力を頂きました．ここに感謝の意を表します．

引 用 文 献

［1］稲崎慎也，佐藤真路，一ノ瀬剛，P. A. Leitl，A. Flanschger，S. Schreck and R. Benauer，“超小型ジェットエンジンの最適リブレット計算とそのレーザ加工，およびエンジン性能での効果検証，”*第49回日本ガスタービン学会定期講演会*，A-25, 2021.

［2］三宅裕，“壁乱流の渦，”*ながれ*，vol. 22, pp. 29–34, 2003

［3］鈴木雄二，笠木伸英，“壁面乱流の知的能動制御，”セーブメーション・レビュー，マイクロフローセンサ特集号，pp. 50–57, 2001.

［4］D. W. Bechert, G. Hoppe and W.-E. Reif, “On the drag reduction of shark skin,” in *Proc. 23rd Aerospace Sciences Meeting*, 1985, doi: 10.2514/6.1985–546.

［5］D. W. Bechert, M. Bartenwerfer, G. Hoppe and W.-E. Reif, “Drag reduction mechanisms derived from shark skin,” in *Proc. 15th Congr. ICAS*, vol. 2, pp. 1044–1068, 1986.

［6］“戦略的省エネルギー技術革新プログラム　省エネルギー技術開発事業の重要技術に係る周辺技術・関連課題の研究革新的リブレットによる高速移動体の省エネルギー化技術の調査研究，”成果報告書 2018年 3 月，NEDO, https://www.nedo.go.jp/library/seika/shosai_201803/20180000000035.html, 2018.

［7］P. A. Leitl, V. Stenzel, A. Flanschger, H. Kordy, C. Feichtinger, Y. Kowalik, S. Schreck and D. Stübing, “Riblet surfaces for improvement of efficiency of wind turbines,” in *Proc. AIAA Scitech 2020 Forum*, 2020, doi: 10.2514/6.2020–0308.

［8］P. A. Leitl, E. Göttlich, A. Flanschger, A. Peters, C. Feichtinger, A. Marn and B. Reschenhofer, “Numerical investigation of optimal riblet size for TCF strut flow and their impact on the performance,” in *Proc. AIAA Scitech 2020 Forum*, 2020, doi: 10.2514/6.2020–0307.

［9］P. A. Leitl, M. L. Garcia De Albeniz and A. Flanschger, “Nano- and microstructured riblet surfaces for centrifugal industrial compressors,” in *Proc. Conf. SUstainable PolyEnergy Generation and HaRvesting*（*SUPEHR*）, 2019, pp. 32–38.

［10］A. Sareen, R. W. Deters, S. P. Henry and M. S. Selig, “Drag reduction using riblet film applied to airfoils for wind turbines,” in *Proc. 49th AIAA Aerospace Sciences Meeting including the New Horizons Forum and Aerospace Exposition*, 2011, doi: 10.2514/6.2011–558.

［11］B. N. Chichkov, C. Momma, S. Nolte, F. von Alvensleben and A. Tünnermann, “Femtosecond, picosecond, and nanosecond laser ablation of solids,” *Appl. Phys. A*, vol. 63, pp. 109–115, 1996.

［12］M. C. Richardson, “New opportunities with intense ultrashort-pulse lasers,” in *Proc. OPTICS, ELECTRO-OPTICS, AND LASER APPLICATIONS IN SCIENCE AND ENGINEERING*, 1991, doi: 10.1117/12.43608.

［13］P. A. Leitl, S. Kuntzagk, A. Flanschger and K. Pfingsten, “Experimental and numerical investigation of the reduction in skin friction due to riblets applied on the surface of a Taylor-Couette cell,” in *Proc. of AIAA SciTech 2019Forum*, 2019, doi: 10.2514/6.2019–1625.

［14］綿引健二，蘆田憲一，土橋晋太郎，土橋広和，佐藤真路，一ノ瀬剛，“ガスタービン圧縮機部材へのレーザー加工による，リブレット形成と機械特性評価結果，”*第49回日本ガスタービン学会定期講演会*，B-27, 2021.

［15］日本ガスタービン学会，*ガスタービン工学*，改訂第一版，日本ガスタービン学会，2017.

［16］中村佳朗，鈴木弘一，*ジェットエンジン*，森北出版，2004.

稲崎慎也　Shinya INASAKI
次世代プロジェクト本部 第二開発部
2nd Development Department
Next Generation Project Division

Peter A. LEITL
Bionic Surface Technologies 社
Bionic Surface Technologies

Andreas FLANSCHGER
Bionic Surface Technologies 社
Bionic Surface Technologies

Stefan SCHRECK
Bionic Surface Technologies 社
Bionic Surface Technologies

Richard BENAUER
Bionic Surface Technologies 社
Bionic Surface Technologies


稲崎慎也
Shinya INASAKI


Peter A. LEITL


Andreas FLANSCHGER


Stefan SCHRECK


Richard BENAUER

ガスタービン圧縮機部材へのレーザー加工によるリブレット形成と機械的特性評価†

綿引健二，蘆田憲一，土橋晋太郎，土橋広和

Riblet Formation by Laser Ablation on Gas Turbine Compressor Materials and Evaluation Results of Mechanical Properties

Kenji WATAHIKI, Kenichi ASHIDA, Shintaro TSUCHIHASHI and Hirokazu TSUCHIHASHI

圧縮機翼やタービン翼表面にリブレット形状を形成する事は，ガスタービンの効果率改善の可能性があるが，機械的な強度特性への影響が懸念される．我々はレーザーアブレーション加工で，表面にリブレット形状を施した材料の強度試験を実施した．引張強度およびクリープ特性への影響は見られなかったが，疲労強度の低下を確認した．その対策として，コーティング施工とリブレット加工を組み合わせる手法の検討を行った．我々は，アルミ系の耐食コーティングや TiAlN 系の硬質コーティングを用いて作成したサンプルで評価を行い，疲労強度低減を抑制できる事を実験的に確認した．適切なコーティングの選択と施工を行う事で，疲労強度低下を抑制して，リブレット形状を形成できると考えられる．

Forming riblets on the surface of a compressor blade or turbine blade can improve a gas turbine's performance, but there is concern about detrimental effects on mechanical strength characteristics. We conducted strength tests on a material with riblets formed on the surface by laser ablation. No effect on tensile and creep properties was seen, but fatigue strength was decreased by riblet processing. To prevent fatigue strength reduction, we examined a method that combines coating and riblet processing. We evaluated samples prepared with either an aluminum-based corrosion-resistant coating or a TiAlN-based hard coating, and experimentally confirmed that the effect on fatigue strength can be reduced. It is proposed that selecting an appropriate coating, optimizing the coating method, and optimizing the process of riblet formation can yield performance improvements without sacrificing tensile, creep, or fatigue strength.

Key words ガスタービン，リブレット，レーザー加工，高サイクル疲労試験，コーティング
gas turbine, riblet, laser processing, high cycle fatigue test, coating

1 はじめに

ガスタービンをはじめとする流体機器の効率の向上は大きな課題の一つである．流体抵抗は圧力抵抗（慣性抵抗）と摩擦抵抗（粘性抵抗）に大別され，特に高レイノルズ数の乱流領域においては，層流に比べて大きな壁面乱流摩擦抵抗が発生する［2］．乱流摩擦抵抗を低減させるために，流体機器表面に微小な縦溝を施工する手法がある．リブレット（riblet）と呼ばれる，サメの鱗［3］，［4］のような 35～100 μm 程度の微小な縦溝が表面に存在すると，平滑面に対して，8～10%程度の乱流摩擦抵抗低減を引き起こすことが実験的にも明らかにされている［5］．また，産業界への応用に関して，風力タービン向けに金型を用いた樹脂フィルムでリブレット形状を作成した事例がある［6］．

我々は，上記のリブレット形状をレーザーアブレーション加工により形成する技術を開発し，ガスタービンの圧縮機やタービン翼への適用を検討している．レーザーアブレーション（laser ablation）とは，ナノ秒，ピコ秒，フェムト秒のパルス幅を持つ極短パルスレーザーによって非熱的に材料表面の物質を除去する技術である［7］，［8］．この技術を用いて，任意の形状を材料表面に形成する事ができる．また，ガスタービンの圧縮機やタービン翼には，各種合金の他，金属・セラミックの様々なコーティングが用いられる［9］，［10］．レーザーアブレーション技術を用いれば，それら部材表面にも任意の微細形状のリブレットの直接加工を行う事が可能である．我々は，これまでにリブ

† 本稿は，自著の引用文献［1］に対して実測と解析の乖離の要因，および実用条件を想定した場合の影響に考察を加えたものである．

レットの優位性の検証のため，金属性のタービン翼に直接，流体解析（CFD）に基づいて設計したリブレットをレーザー加工で形成し，その実測を行った．タービンテスト設備の出口案内翼（静翼）にリブレットを形成した評価で，リブレットによる圧損低減効果の実測を行った［11］．また，超小型ジェットエンジンの各翼にリブレット加工を行い，推力や燃料効率の向上を確認した［12］．

一方，材料表面にリブレットのような切欠きを形成すると，材料の強度特性の低下が懸念される．特に疲労強度は，一般に表面の微小な切り欠き形状により影響を受ける事が知られている［13］．そこで，我々は圧縮機部材に直接リブレット加工を施した試験片を準備し，引張・クリープ・疲労試験を実施して，その特性を評価した．また，母材の疲労強度低減の防止策として，コーティングにリブレットを形成する手法を検討し，その加工の適用性と疲労強度特性を評価した．本稿では，筆者らの評価結果［1］に対して，リブレット形状による応力集中について追加評価結果と解釈を加えたものである．

2 リブレット加工

リブレットの加工にはレーザー加工の開発機を用いた．Fig. 1 にその模式図を示す．このレーザー加工機は，波長 532 nm（緑色），パルス幅約 15 ps，最大繰返し周波数 4 MHz，最大出力 50 W の短パルスレーザーを持つ．レーザー光は照射ヘッドに導かれ，ガルバノミラーによって同期してスキャンされる．レーザー光は f θ レンズによって所定の位置に集光される．加工対象物は 3 軸ステージによって所定の XYZ 位置に駆動できる．レーザー光が集光した対象物の表面はアブレーションにより除去され，これを連続的にスキャンすることでリブレットの溝が形成される．条件を制御する事でピッチや深さ，リブレット形状を制御する事が可能である．

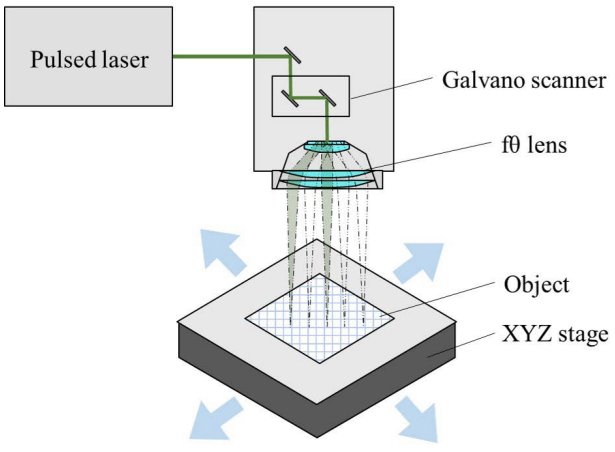

Fig. 1　Schematic diagram of a laser processing machine for forming riblets on the surface of an object

3 実験方法

3.1. 試験片

試験片は，各強度試験に合わせた形状の平板を用意して，そこにリブレット加工を施した．材質は圧縮機の前段側の翼で用いられる SUS630［9］を用いた．コーティングと組み合わせた試験片には SUS304を用いた．試験片形状，加工領域の模式図を Fig. 2 に示す．リブレット加工は，平行部の 25 mm の領域に行い，ピッチと深さは，それぞれ 50 μm，25 μm を目標値として加工を行った．この寸法は，流体低減効果を確認しているものの中で，代表的なサイズである．また，1 本の試験片でリブレット加工の影響の有無を評価するため，リブレット加工は片面にのみ行った．

リブレット形成後の疲労強度の低下対策として，Fig. 3 に示す 2 種類のコーティングを検討した．リブレットのサイズに対して十分に厚い膜のコーティングと，薄いタイプである．薄いタイプはリブレット加工後にコーティングを施工した．

厚膜のタイプは圧縮機翼のコーティングとして用いられるものを用いた．母材に Al 粒子を含んだ中間コーティングを塗布，中間コーティングにリブレット加工を実施し，その上からトップコーティング（～5 μm）を施工した．

薄膜のタイプは TiAlN 膜を用いた．一般に工具や刃物に用いられる非常に高硬度のものである．Ti 合金へ施工し，ガスタービン向けへの検討例もある［14］．母材にリブレット加工を行ったあとに，PVD でコーティング（～3 μm）を行った．リブレット加工した上に高硬度のコーティングを施工する事で，表面のクラック生成を防ぎ，疲労強度を改善できると考えた．なお，コーティングの施工条件によっては良好な疲労強度を示す結果が得られている［13］．

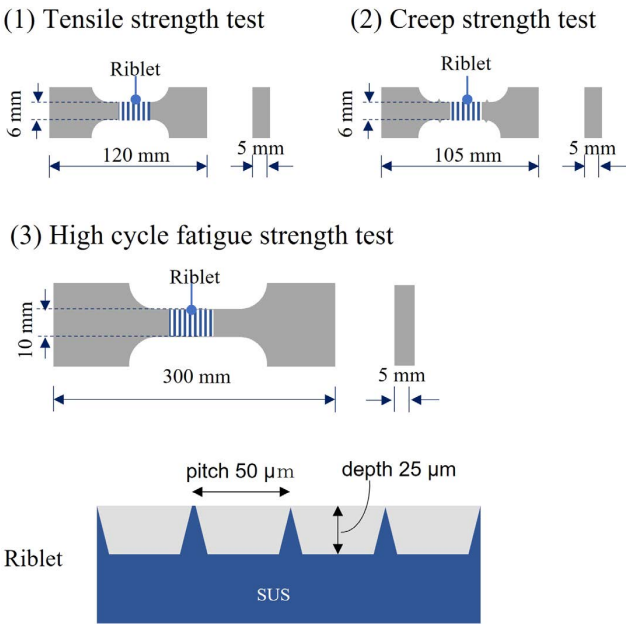

Fig. 2　Dimensions of each strength test sample and riblet

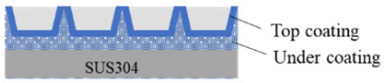

(a) Riblet the under coating and then apply the top coat

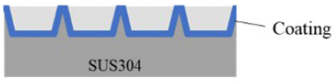

(b) Riblet the base material and then apply a coating

Fig. 3　Coating methods for test samples

3.2. 機械試験の条件

Table 1 に今回実施した機械試験項目と条件を示す．各試験は試験機関にて JIS Z2241，2271，2273に則り実施した．圧縮機へのリブレット加工の適用を想定し，引張試験は室温と600℃の 2 条件で実施した．クリープ試験は600℃，200 MPa の条件で実施した．高サイクル疲労試験の試験モードは軸方向荷重制御で，応力比は 0，波形は sim 波である．

Table 1　Strength test condition

Test item	Test condition	Sample
Tensile strength test	(1) RT	SUS630
	(2) 600℃	
Creep strength test	600℃, 200 MPa	
High cycle fatigue test	RT.pulsating tension (Tensile)	(1) SUS630
		(2) SUS304 without coatmg
		(3) SUS304 with Al including coating
		(4) SUS304 with TiAIN coating

また，破壊メカニズム等の調査のため，試験後に光学顕微鏡，走査型電子顕微鏡（SEM）等を用いて破面の表面および断面観察を行った．試験片は，引張試験とクリープ試験は SUS630で実施し，高サイクル疲労試験は SUS630と SUS304，SUS304にコーティングを施工した試験片を用意し，計 4 条件で実施した．なお，各試験片で，リブレット加工が有るものと無いものをそれぞれ用意して，試験を実施した．

4 実験結果および考察

4.1. リブレット加工の適用性

Fig. 4 に SUS630にリブレット加工を行い，その形状をレーザー顕微鏡で評価した結果を示す．目標値に対して，深さがやや大きいが，ピッチ 50 μm で周期的な溝構造が形成出来ている事が分かる．

同様に Fig. 5 にコーティングとリブレット加工を組み合わせた試験片のリブレット形状を評価した結果を示す．コーティング前後の結果も載せている．いずれの試験片でも，周期的な溝構造が作成できており，コーティングの上からでもリブレット加工が出来ている事が分かる．また，コーティング前後の結果を見ると，２種類とも形状の差異がほとんど見られず，リブレット加工後に薄膜をコーティングする手法でも，リブレットを形成する事が可能である事が分かる．なお，試験片で，リブレット形状にバラつきがあるが，加工条件を調整する事で，このバラつきは小さくする事ができる．

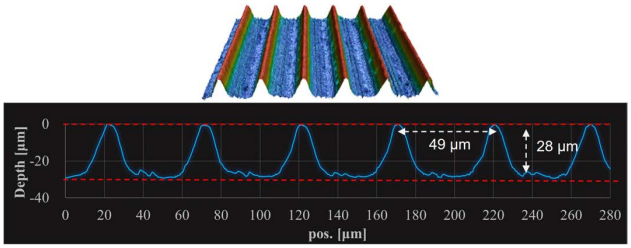

Fig. 4　Microscopic profiles of lasered riblet SUS630 sample

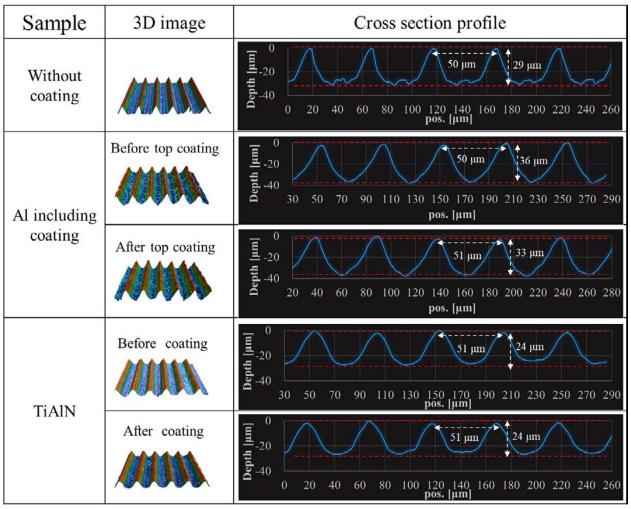

Fig. 5　Microscopic profiles of lasered riblet SUS304 with and without coating sample

リブレット加工前後の断面を光学顕微鏡で観察した結果を Fig. 6 に示す．室温にて高サイクル疲労試験を実施した後の破断部から離れた位置での観察結果である．リブレット加工面の直下での金属組織の変化や，加工変質層などは見られなかった．レーザーによる溶接や切断等，熱影響が生じる加工では，強度が低下する事例が知られているが，リブレットの形成はアブレーション加工であるため，熱影響が小さいことが伺える．

4.2. リブレット加工材の機械的特性

Fig. 7，Fig. 8 にリブレット加工有無の引張試験およびクリープ試験の結果を示す．各試験とも N 数 3 で実施し，そ

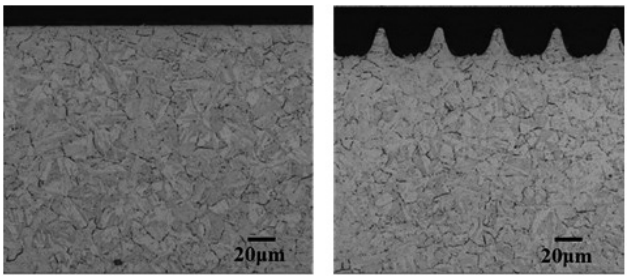

(a) Before (b) After

Fig. 6 Metallographic observation of SUS630 stainless steel before and after riblet processing

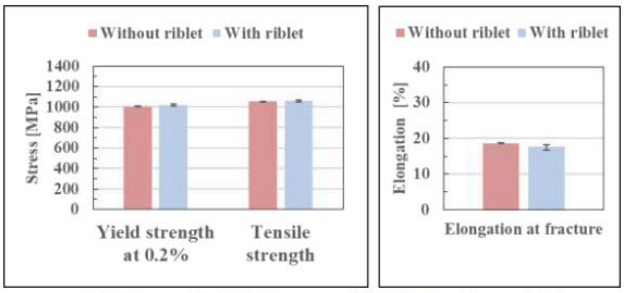

(a) Strength (RT) (b) Elongation (RT)

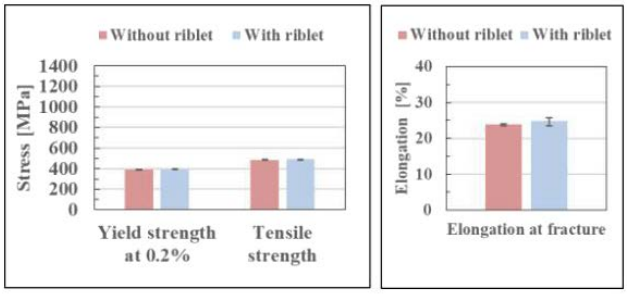

(c) Strength (600°C) (d) Elongation (600°C)

Fig. 7 Tensile strength and elongation for with and without riblet

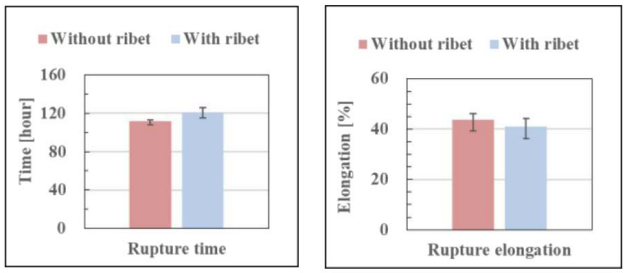

(a) Rupture time (b) Rupture elongation

Fig. 8 Creep rupture time and rupture elongation for with and without riblet

の平均値でグラフをプロットした．引張強さ，0.2%耐力，伸びともにリブレット加工の有無で有意差は見られず，リブレット加工により引張特性の低下は見られなかった．

クリープ試験の結果を Fig. 8 に示す．破断時間および伸びともほぼ同等の値を示し，リブレット加工によりクリープ特性の低下は見られなかった．

リブレット加工による疲労強度への影響は負荷応力を変えて，破断までの繰り返し数を求め，S-N 曲線を作成し，10^7 サイクル以上の疲労限を求めた．その結果を Fig. 9 に示す．リブレット加工により，強度低下している事が分かる．なお，リブレット加工が有る試験片の試験応力の算出は，試験片の厚みからリブレット加工深さ（約 25 μm）分を除いた値で算出した．

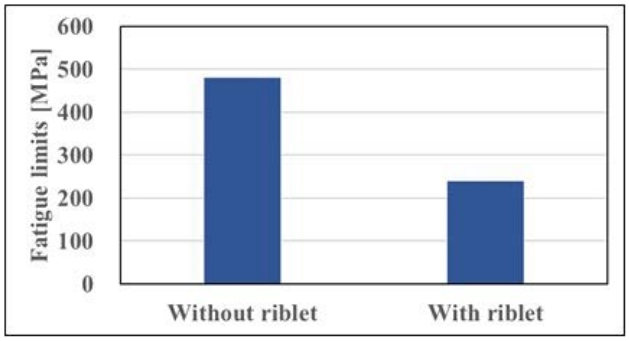

Fig. 9 Fatigue limits for with and without riblet SUS630 sample

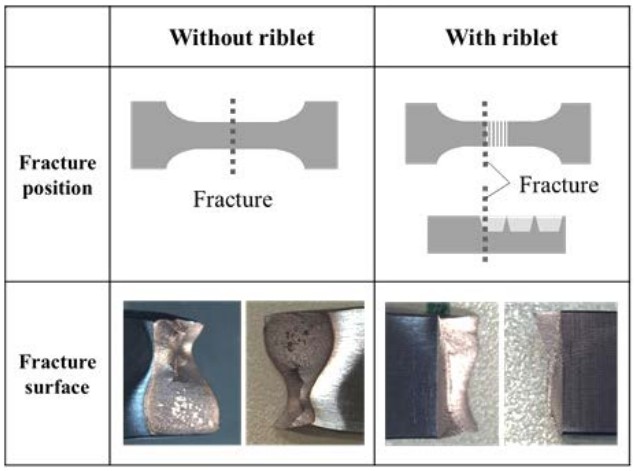

Fig. 10 Fracture surface observation result of SUS630 samples

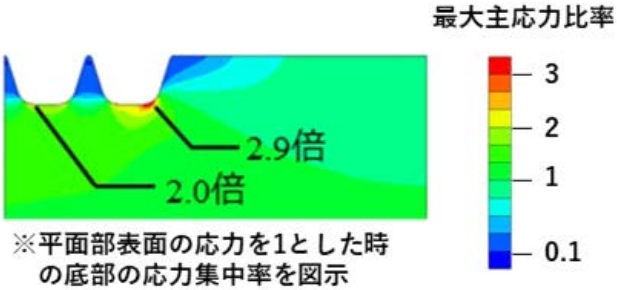

Fig. 11 Stress distribution analysis result of riblet

リブレット加工による疲労限が減少した要因を考察するため，破面観察と応力解析を行った．結果をそれぞれ破断 Fig. 10，Fig. 11 に示す．リブレット加工がない試験片の破

面は，内部に平坦な脆性破壊部がわずかに認められ，それ以外は大きく塑性変形が生じており，ほとんどが延性破壊を呈していた．内部の介在物を起点として，クラックが発生，成長して疲労破壊が生じ，その後，塑性変形を伴って破断したと推測される．一方，リブレット加工が有る試験片では，リブレット加工部と非加工部の境界で破断が生じていた．破断の形態は直線的で，リブレットの溝に沿って脆性的に破壊，その後は塑性変形を伴って破壊している事を確認できた．次に応力解析から，リブレットの各底部で応力が集中する事が分かった．また，最も応力が集中する部分は加工の際部分であり，実験での破断位置と一致した．以上の事から，リブレット形状による切り欠きにより，溝部で応力集中が生じ，クラックが発生し，進展したと推測される．

4.3. コーティングとリブレット加工材の高サイクル疲労特性

コーティングとリブレット加工を組み合わせた材料の疲労強度を調べた．その結果を Fig. 12 に示す．試験応力を算出するための試験片の厚みは，コーティング皮膜の厚さを考慮せず，母材の値とした．また，SUS304試験片は，SUS630の場合と異なり，リブレット加工深さは未考慮とした．同条件で複数の試験片で試験を行った結果は，平均値でグラフをプロットしている．コーティングを付与する事で，疲労強度に違いが見られた一方で，リブレット有り・なしの差は見られなくなった．

コーティングがない試験片の観察結果を Fig. 13 に示す．リブレット加工なしの試験片では，角部が起点となり，クラックが進展，その後，塑性変形を伴って破断している．一方，リブレット加工が有る試験片では，破断位置は加工部の境界で，リブレット溝部が起点となり，クラックが進展，その後，塑性変形を伴って破断したと考えられる．応力集中により，リブレット加工なしと比較して，早期にクラックが発生，進展したため破断までの繰り返し数が低下したと考えられる．

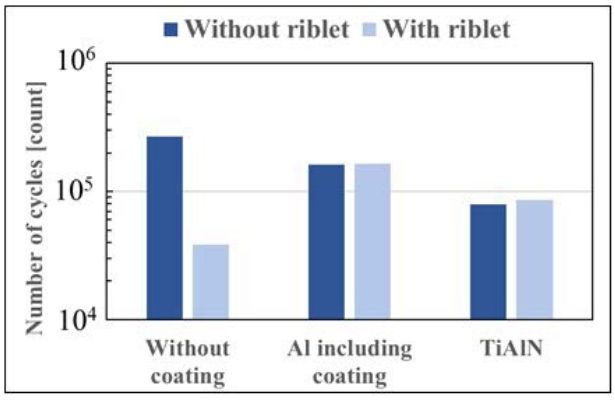

Fig. 12　Comparison of the number of cycles to fracture at 225 MPa stress amplitude of SUS304 samples

Fig. 14 に厚膜のタイプのコーティングを施工した試験片の観察結果を示す．リブレット加工有り・なし共に，破断位置は試験片の中心付近であった．この形態はコーティングなし・リブレット加工なしの結果と同様である．破断部付近はコーティングの剥離が生じていた．SEM 観察で，表面に無数のクラックが生じていたが，そのクラックが母材に進展している様子は見られなかった．

以上の事から，試験初期にコーティングにクラックが生じて，クラックが母材に進展することなく，コーティングの剥離が生じ，母材表面が露出，その後，破断したと推測される．クラックの進展特性は，コーティングの種類や母材との密着性で変化し，ヤング率の低いコーティングは進展しにくいとされる［15］，［16］．今回，用いたコーティン

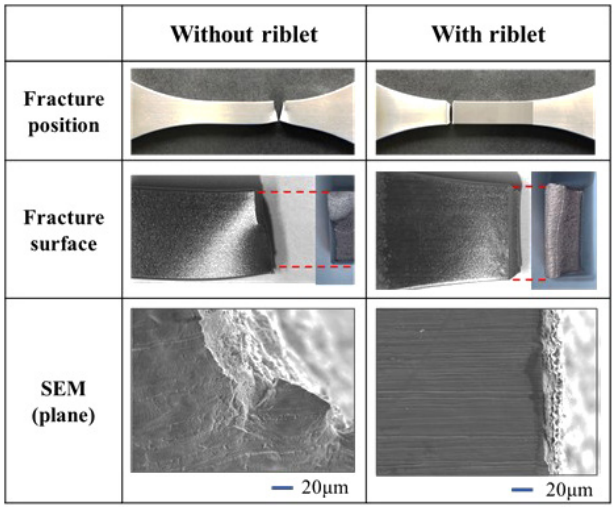

Fig. 13　Fracture surface observation result of SUS304 without coating

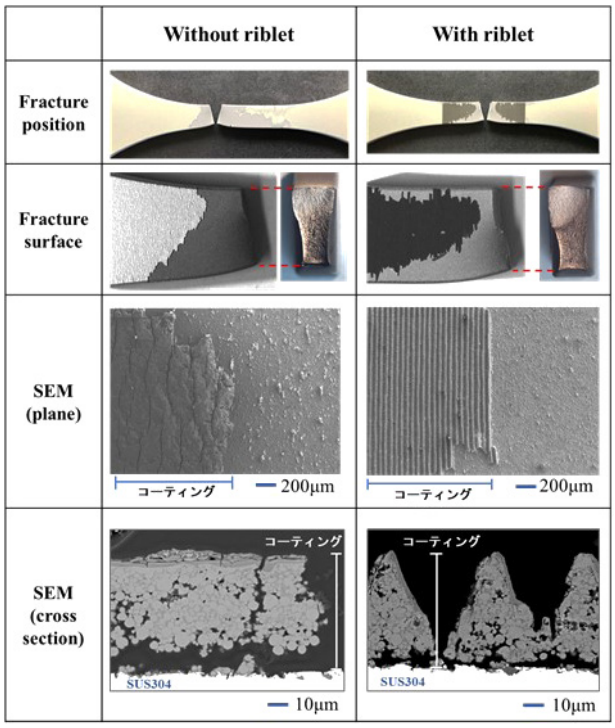

Fig. 14　Fracture surface observation result of SUS304 with Al including coating

グは，表面にクラックが生じやすいが，母材との密着力が比較的小さく，母材へのクラックの進展が生じなかったと考えられる．なお，リブレット加工がない試験片で，コーティング施工有り・なしを比較すると，コーティング施工で疲労強度が若干低下している．同様の例は古くから知られている［17］．表面残留応力の変化，クラックの発生しやすいコーティングを付加した時など複数の要因が考えられる．今回のケースでは，コーティング施工過程内で残留応力の変化もしくは界面の粗さの変化によるものと考える．今回実施している疲労試験では引張応力を負荷しているため，あらかじめ引張の残留応力が生じていると，その分，疲労強度が低下する事が考えられる．後者は，粗さの変化により，クラックの生成がしやすくなった事が考えられる．これらの要因を調査し，コーティング施工方法を適正にする事で，疲労強度を維持し，リブレット加工を行う事が可能であると考えられる．

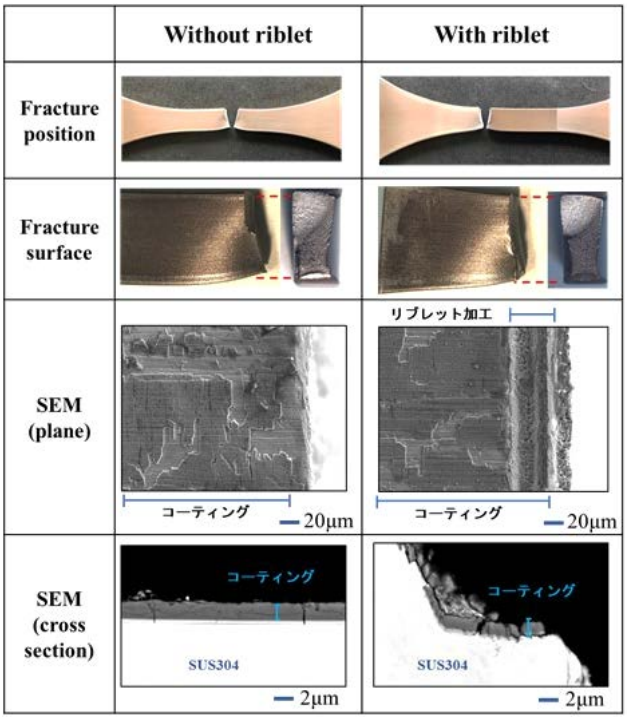

Fig. 15　Fracture surface observation result of SUS304 with TiAlN coating

Fig. 15 に薄膜タイプのコーティングを施した試験片の観察結果を示す．破断位置はリブレット有り・なしで異なり，リブレット加工がない試験片は中心付近，リブレットが有る試験片は加工部の境界であった．SEM 観察より，リブレット加工なしでは，コーティング部において，応力方向に垂直な無数のクラックが観察され，一部は母材にまで進展しているクラックも見られた．リブレット加工が有る試験片では，リブレット溝部を中心にコーティングが剥離している様子が見られた．

コーティングを施工していなく，リブレット加工もない試験片と比較すると，疲労強度が低下している．無垢の母材表面よりも TiAlN コーティングは非常に硬く，延性が低いため，母材の大きな変形に追従せず，クラックが生じ，その後，一部のクラックが母材に進展し易くなったと考えられる．延性が異なるコーティングや，他の母材に適用する事で疲労強度が改善する可能性があると考えられる．リブレット加工しても疲労強度がさらに低下しないのは，応力集中部を含め，リブレット加工部の表面が硬質膜で保護されたためと考える．

5　まとめ

レーザーアブレーション加工でリブレット形状を施した材料の加工の適用性および強度評価を実施した．金属表面の他，アルミ系の耐食コーティングや TiAlN 系の硬質コーティングにもリブレット加工が適用できることを確認した．

機械的特性に及ぼすリブレット加工の影響について，引張およびクリープ特性への影響は認められなかったが，高サイクル疲労強度は，リブレット形状により，応力集中部が生じて低下した．その対策として，コーティング施工とリブレット加工を組み合わせる手法の検討を行った．その結果，母材までクラックが進展しにくいコーティングにリブレット加工する手法，またはリブレット加工後にクラックが母材まで入りにくい薄いコーティングを付加する手法により，疲労強度の低下を抑制できると考えられる．母材との組み合わせを含む，最適なコーティングの施工方法の開発を引き続き行っていく予定である．

引　用　文　献

［1］綿引健二，蘆田憲一，土橋晋太郎，土橋広和，佐藤真路一ノ瀬剛，“ガスタービン圧縮機部材へのレーザ加工による，リブレット形成と機械特性評価結果，”*第49回日本ガスタービン学会定期講演会*，B-27, 2021.

［2］三宅裕，“壁乱流の渦，”*ながれ*，vol. 22, no. 1, pp. 29–34, 2003.

［3］鈴木雄二，笠木伸英，“壁面乱流の知的能動制御，”セーブメーション・レビュー　マイクロフローセンサ特集号（2001），pp. 50–57, 2001.

［4］D. W. Bechert, G. Hoppe, W.-E. Reif, “On the drag reduction of shark skin,” in *Proc. 23rd Aerospace Sciences Meeting*, 1985, doi: 10.2514/6.1985-546.

［5］D. W. Bechert, M. Bartenwerfer, G. Hoppe, W.-E. Reif, “Drag reduction mechanisms derived from shark skin,” in *Proc. 15th Congr. ICAS*, Sep. 1986, pp. 1044–1068.

［6］A. Sareen, R. W. Deters, S. P. Henry, M. S. Selig, “Drag Reduction Using Riblet Film Applied to Airfoils for Wind Turbines,” in *Proc. 49th AIAA Aerospace Sciences Meeting including the New Horizons Forum and Aerospace*, doi:10.2514/6.2011-

558.
［7］B. N. Chichkov, C. Momma, S. Nolte, F. von Alvensleben, A. Tünnermann, “Femtosecond, Picosecond, and Nanosecond Laser Ablation of Solids,” *Appl. Phys. A*, vol. 63, no. 2, pp. 109–115, 1996.
［8］M. C. Richardson, “New Opportunities with Intense Ultra-Short-Pulse Lasers,” in *Proc.of SPIE*, vol. 1410, 1991.
［9］吉岡洋明，土井裕之，武田淳一郎，難波浩一，岡田郁生，武浩司，伊藤健之，“発電用ガスタービンの材料技術，” *日本ガスタービン学会誌*，vol. 32, no. 3, pp. 4–47, 2004.
［10］R. Rajendran, “Gas turbine coatings - An overview,” *Engineering Failure Analysis*, vol. 26, pp. 355–369, 2012, doi:10.1016/j.engfailanal.2012.07.007.
［11］白石雅之，土橋晋太郎，一ノ瀬剛，柴崎祐一，P. A. Leitl, A. Flanschger, S. Schreck, R. Benauer, S. Pramstrahler, A. Marn,“タービンテストリグ出口案内翼への最適リブレット効果予測と，そのレーザー加工によるリブレット性能評価，” *第49回日本ガスタービン学会定期講演会*，A-24, 2021.
［12］稲崎慎也，佐藤真路，一ノ瀬剛，P. A. Leitl, A. Flanschger, S. Schreck, R. Benauer,“超小型ジェットエンジンの最適リブレット計算とそのレーザ加工，およびエンジン性能での効果検証，” *第49回日本ガスタービン学会定期講演会*，A-25, 2021.
［13］日本機械学会，*金属材料 疲労強度の設計資料1*，改訂第２版，東京：日本機械学会，1982.
［14］N. P. Sivagnanam Chandra, Y. Otsuka, Y. Mutoh, K, Yamamono, “Effect of coating thickness on fatigue behavior of TiAlN coated Ti-alloys,” *International Journal of Fatigue*. vol 140, pp. 105767, 2020. doi:10.1016/j.ijfatigue.2020.105767.
［15］伊藤義康，斉藤正弘，石渡裕，“MCrAlY 合金コーティング部材の高サイクル疲労寿命特性，” *溶接学会論文集*，vol. 15, no. 2, pp. 359–364, 1997.
［16］伊藤義康，斎藤正弘，宮崎松生，“減圧プラズマ溶射皮膜の機械特性とき裂進展特性，” *日本機械学会論文集［A編］*，vol. 60, no. 579, pp. 2538–2543, 1994.
［17］日本機械学会，*金属材料 疲労強度の設計資料2*，改訂第２版，東京：日本機械学会，1984.

綿引健二　Kenji WATAHIKI
次世代プロジェクト本部 第二開発部
2nd Development Department
Next Generation Project Division

蘆田憲一　Kenichi ASHIDA
次世代プロジェクト本部 第二開発部
2nd Development Department
Next Generation Project Division

土橋晋太郎　Shintaro TSUCHIHASHI
次世代プロジェクト本部 第二開発部
2nd Development Department
Next Generation Project Division

土橋広和　Hirokazu TSUCHIHASHI
次世代プロジェクト本部 第二開発部
2nd Development Department
Next Generation Project Division


綿引健二
Kenji WATAHIKI


蘆田憲一
Kenichi ASHIDA


土橋晋太郎
Shintaro TSUCHIHASHI


土橋広和
Hirokazu TSUCHIHASHI

仮想環境におけるレイキャスティングを用いたインタラクティブ・サーフィスの設計と没入型フォトブラウザへの応用

高階知巳，伊藤　充，長浦　仁，若林英佑

Design of Curved Raycasting-based Interactive Surfaces in Virtual Environments and Its Application to an Immersive Photo Browser†

Tomomi TAKASHINA, Mitsuru ITO, Hitoshi NAGAURA and Eisuke WAKABAYASHI

3 次元ユーザインタフェースが一般的になると，素早く操作でき信頼性の高い選択方法・操作方法が必要とされる．我々は仮想空間の中でレイキャスティングを用いて操作する仮想ディスプレイ（インタラクティブ・サーフィス）が曲率を制御できる曲面を持っているとして，その操作性を評価する．ユーザはヘッドマウントディスプレイを装着し，その中に見えるインラクティブ・サーフィスをハンドコントローラにより操作する．我々は操作にかかる時間と操作の精度を様々な条件の曲面に対して調査した．異なる曲面の条件に対してのユーザの操作能力を調べるために，完全な平面を含む異なる曲率を持った曲面を用いて実験を行った．実験結果から，表示面の曲率を変えることで，最も効果的な場合には，完全な平面に対して28%精度が良く，15%高速にポインティングできることがわかった．この結果を応用し，我々は，曲面に写真を配置する没入型写真ブラウザを設計・実装した．これらの結果は，一般的な 2 次元スタイルのアプリケーションにおいて，空中ポインティング機能を持った，曲面のインタラクティブ・サーフィスに適用することが可能である．

As three-dimensional user interfaces become more popular, quick and reliable aerial selection and manipulation are desired. We evaluated a virtual curved display (interactive surface) with controllable curvature based on raycasting. The user operates the surface by pointing using a head-mounted display and grip-type controller. We investigated the operation speed and accuracy of curved interactive surfaces under various presentation conditions. To investigate the users' operation ability for different curved conditions, we experimented with multiple surface curvature radii, including completely flat conditions. The experimental results showed that varying the curvature of the display improved the pointing accuracy by 28% and the speed by 15% over the flat surface in the most effective cases. By utilizing the analysis results, we designed and implemented an immersive photo browser in which photos are placed on a curved surface. These findings can be applied to curved interactive surfaces with mid-air pointing for generic two-dimensional-style applications.

Key words 仮想空間，インタラクティブ・サーフィス，仮想ディスプレイ，空中ポインティング，レイキャスト，写真ブラウザ
virtual reality, interactive surface, virtual display, mid-air pointing, raycasting, photo browser

1 Introduction

Displays in a virtual environment (VE) provide a fully programmable workspace without the need for large physical spaces. The advantage of such virtual workspaces is that they allow us to adopt findings regarding operational efficiency from physical large screen display design [4]. Large workspaces display a large amount of information, however manipulation through the pointing interface is difficult. One of the solutions to these problems is to design a curved workspace [1], [2].

Although such large displays are difficult to operate, the raycasting technique can be used to interact with objects in a virtual world, which is advantageous compared to pointing in the real world [3], [6]. Therefore, we compared the operational efficiencies of flat and curved surfaces assuming that raycasting was used in VEs.

In this study, we evaluated curved virtual interactive sur-

† This paper is based on [5] and includes a new section for an application of the proposed method.

faces and investigated the effects of curvature, size, and presentation distance on operational efficiency. The operation was performed using ray casting to point away from the user. The design parameters were analyzed based on Fitts' law, which accounts for the amount of ray travel.

The remainder of this paper is organized as follows. First, we present a theoretical analysis of the operation time for flat and curved surfaces. Next, we describe experiments to evaluate the operational efficiency of the interactive surface with respect to pointing and clicking on position and size. We then introduce our implementation of an immersive photo browser based on the results of the experiments. Finally, we conclude this paper.

2 Operation Time Analysis by Fitts's Law

Shupp investigated the curvature of a real large display and found that users could operate it 30% faster than flat displays [4]. In a virtual world, a display shape can be designed without any physical restrictions.

We compared the operational efficiencies of flat and curved surfaces. We conducted a theoretical analysis of the time required to point to the leftmost and rightmost selective targets using Fitts's law: $T = a + b\log_2(1+ D/W)$. For the analysis of pointing via raycasting, the ray is controlled by changing the angle of the hand. Thus, we used W and D as the values converted into angles. Let T^f and T^c be the times required to point to the edge targets on a flat panel and curved panel, respectively. Fig. 1(a) and (b) show the schematics of flat and curved surfaces and the operations based on the assumption of one-dimensional movements. If we assume $a = 0$, the speedup of a curved surface can be expressed as

$$S^* = (T^f - T^c)/T^f = 1 - \log(1 + D/W)/\log(1 + D/W).$$

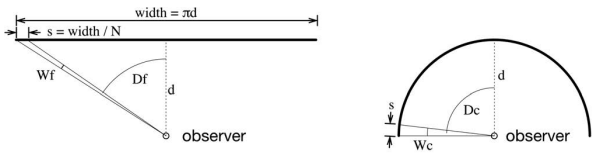

Fig. 1 Models for Interactive Surfaces. The user's operation angle is controlled by the curvature radius of the virtual surface.

3 Experiment

To evaluate the suitability of different shapes for an immersive interactive surface, we conducted within-subject experiments to investigate the effects of display size and curvature radius on the selection of a grid of visual objects.

The participants were required to perform pointing tasks in a virtual space, as shown in Fig. 2. A virtual interactive surface with a grid was shown to each participant at a time (Fig. 3). The shape of the surface is defined by a combination of several parameters (Fig. 4). The grid had the same pitch in both the horizontal and vertical directions. The width was calculated from the height such that the aspect ratio tended to be 16:9. We employed grids of different sizes to vary the pointing difficulty.

The surfaces have the same arc length (corresponding to the width w of a flat surface) for different curvature radii r_c when the height is fixed. The viewing distance was also varied (Fig. 4(a)). To investigate the percentage of correct responses and the operation time for the user's average operation angle, the length of the presentation distance was varied to be longer and shorter than the minimum radius of curvature.

The participant sat on a chair, put on an Oculus Rift S, and held two Oculus Touch controllers, as shown in Fig. 2(b). The software for this experiment was implemented in Unity. Stimuli were provided to the participants as colored squares for each surface condition. Eight healthy adults (age, 38 ± 10 years; gender, male) participated in the experiment.

The number of surface conditions is 90 ($3 \times 5 \times 2 \times 3$). A surface was chosen in order from the combination table of the four attributes. Because the first factors vary the fastest (refer to Fig. 4(c)) in the combination table and flat conditions scatter in the surface sequence, a counterbalance on the factor of curvature radius was achieved. The stimuli were provided as defined in each experiment. We measured

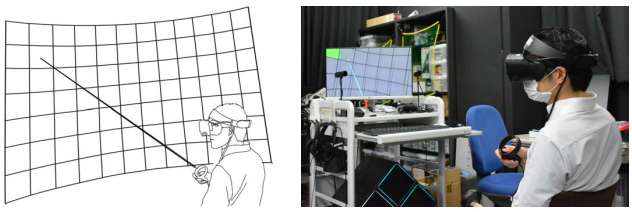

(a) (b)

Fig. 2 Interactive Surface: (a) Concept (b) Photograph of Experimental Setting.

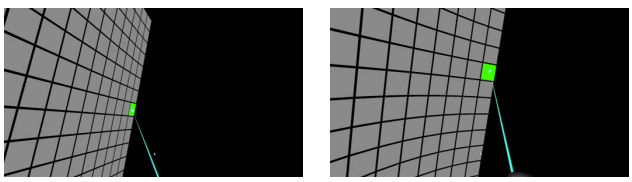

(a) (b)

Fig. 3 Participant's Perspective of Marginal Areas on the Interactive Surface: (a) Flat screen (b) Curved screen. The green target is the selective target.

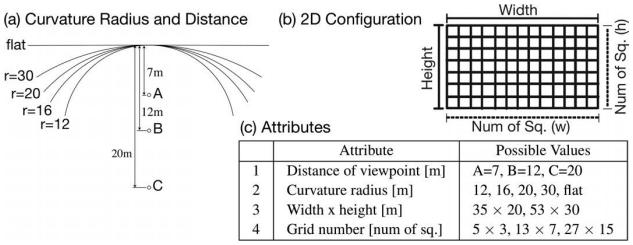

(c) Attributes

	Attribute	Possible Values
1	Distance of viewpoint [m]	A=7, B=12, C=20
2	Curvature radius [m]	12, 16, 20, 30, flat
3	Width x height [m]	35 × 20, 53 × 30
4	Grid number [num of sq.]	5 × 3, 13 × 7, 27 × 15

Fig. 4 Surface Conditions for Experiments. (a) Curvature radii and distance are presented in all combinations. (b) The number of squares, width, and height vary as shown in the table (c).

the time from the appearance of the stimulus until the participant pressed the trigger button. If a participant pressed the trigger button while aiming the ray at a wrong square, we counted it as an error.

3.1. Experiment 1: Target Pointing without Search

The target squares repeatedly appeared at three fixed locations (left end, right end, and center as a reset position) of the center row. In this experiment, we measured the basic sensorimotor response for raycasting on a virtual surface. There were 540 trials (90 surface conditions × 6 stimuli without centers) for each participant.

Fig. 5 shows the plots of the percentage of correct answers vs. curvature radius (r), and Table 2 shows the error ratios of Experiment 1. The larger the radius of the curvature, the larger the error ratio. For small squares (27 × 15 grid), the worst percentage of correct answers was 70% when the flat surface was operated from viewpoint A. This percentage could be improved to 98% using curved conditions (r = 12 or 16), which was an improvement of 28%. One reason for this is that the squares contain large perspective distortions in the edges when a flat screen is used (Fig. 3).

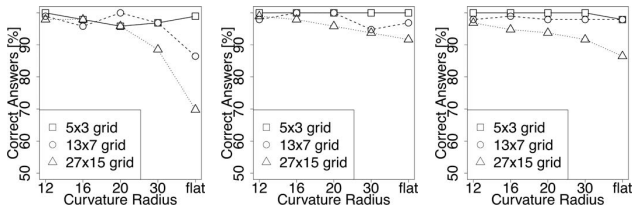

(a) Viewpoint A (d = 7 m) (b) Viewpoint B (d = 12 m) (c) Viewpoint C (d = 20 m)

Fig. 5 Percentage of Correct Answers in Experiment 1

Table 1 Speedup by Curved Surface (27 × 15 grid)

Viewpoint	Time by Curved Surface [sec]	Time by Flat Surface [sec]	Speedup Measured [%]	Speedup Predicted [%]
A	1.05 ± 0.24 (r = 20)	1.20 ± 0.47	12.8*	33.6
B	0.95 ± 0.18 (r = 16)	1.00 ± 0.30	4.9	23.7
C	0.87 ± 0.20 (r = 16)	1.02 ± 0.46	14.6*	14.0

a ± *b* denotes that *a* is a mean and *b* is a standard deviation.

*denotes that it is significant at 5% level of significance by T-test.

Table 2 Average Error Ratios Obtained in Experiments 1 and 2 [%]

	r = 12	r = 16	r = 20	r = 30	flat
Experiment 1 (without Search)	1.2	1.8	2.3	4.3	8.2
Experiment 2 (with Search)	3.7	5.0	5.1	5.5	5.7

For the response time, the curvature radii of the shortest operation time were 20 (A), 16 (B), and 16 (C) for the smallest target size. We summarize the speedup from the flat surface along with the predicted speedup obtained by Fitts's law (S^*_c) in Table 1. Using a t-test, we confirmed that curved surfaces enable speedup in pointing operations. Fitts' law fitted well with the measured data from viewpoint C. Although the learning effect was included in the result by repeated actions, it is considered that the effect occurred on all factors equally, and we can regard the observed tendency as reliable.

3.2. Experiment 2: Target Pointing with Search

This experiment incorporates a target-seeking factor in addition to Experiment 1 to prevent the user from remembering the location of the target. For each surface condition, participants had to point to three targets. A target appeared in a position from a position sequence at a time, generated randomly for each surface condition, and was common among all participants. There were 270 trials (90 surface conditions × 3 stimuli) for each participant. No reset was given in this experiment.

Table 2 lists the average error ratios in Experiment 2. The larger the radius of curvature, the larger the error ratio. This trend is consistent with that observed in Experiment 1.

As for the response time, the observed trends were different from those observed in Experiment 1. Although we omitted the details here, the flat condition was the fastest. There are two possible reasons: (a) the effect of seeking time for out-of-sight targets is large, and (b) difficulty varies between factors because each position sequence is generated randomly and short. In the next step, we need to improve the experiments carefully to address these issues.

4 Application: Immersive Photo Browser

The number of photos has been astronomically increasing with the introduction of modern technologies such as mobile devices, cloud photo storage, and high-speed continuous shooting. It is extremely difficult to search for and view photos because of this increase. Virtual reality (VR) can address this issue by providing portable large-screen environments.

Based on the evaluation experiment in the previous sec-

tion, we designed and implemented a prototype immersive photo browser. It is a suitable application for curved raycasting-based interactive surfaces because it provides a large display with quick and accurate operations.

We developed this application using Unity 2018. The users experienced this VR application using Oculus Rift S as the display and two Oculus Touch controllers as the gesture controllers. Representative features are described in this section.

4.1. Thumbnail Wall

A thumbnail wall is the basis of an immersive photo browser and is used to view a large number of photos simultaneously. We designed and employed a curved surface for the thumbnail wall based on the evaluation experiment described in Section 3. Users select photos of the thumbnail wall for various operations.

Fig. 6 shows an example of a thumbnail wall. Thumbnails at the edge of the wall can be observed to be of sufficient size because they include less perspective distortion with the advantage of a curved surface.

Users can move anywhere in this VE. Continuous navigation (i.e., a user continuously moving in a space) is intuitive, but it easily induces VR sickness. Continuous zooming operations, which are popular in smartphones, also induce VR sickness when used in VR environments.

Therefore, warp-type navigation (i.e., a user moving to a location in a discontinuous manner) should be the primary navigation method coupled with continuous navigation to smoothly adjust the viewpoint of the user.

In the warp-type navigation of an immersive photo browser, users can move to the front of a specified photo by pointing and pressing buttons with the right Oculus Touch controller. Fig. 7 illustrates the scene after moving to the front of the specified photo. For continuous navigation, users can move freely using the left Oculus Touch controller.

Fig. 6 Thumbnail Wall: A total of 1500 photos can be arranged on a wall. A user can view the whole wall naturally as they turn their head.

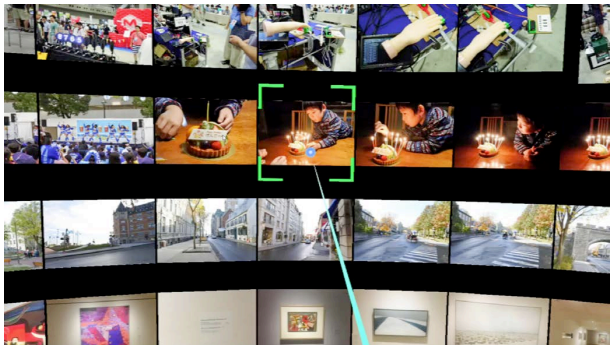

Fig. 7 View after Warping to the Front of a Selected Photo. Green lines show a selection and the cyan line is a ray extended from the user's hand.

Fig. 8 Photo Panel. Photos can be looked at closely in the immersive environment. A user can move photos freely and compare them in the space.

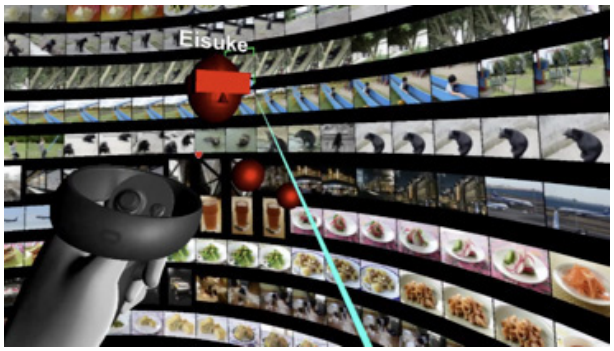

Fig. 9 Collaboration in the Immersive Photo Browser. The avatar of another user can be seen from the viewpoint of the user.

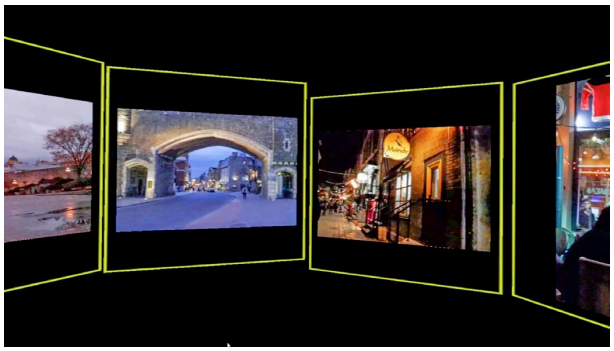

Fig. 10 Virtual Gallery in the Immersive Photo Browser. The photos were selected by pointing to the thumbnail wall and the layout can be adjusted freely.

4.2. Other Features

By pointing at a photo on the thumbnail wall and pressing the trigger button, users can closely view the photo (Fig. 8). Users can quickly move and resize a photo using an Oculus Touch controller.

Fig. 9 shows a scene in which a user collaborates with another user. This collaboration facility is useful in photo-related workflows, such as photo selection for magazine editing, photo galleries, and lectures. Users can also communicate using text chatting and voice chats.

Users can locate photos anywhere they desire to hold personal exhibitions in a virtual gallery (Fig. 10). In addition, users can invite their friends to this gallery.

Among all these features, pointing operations on a thumbnail wall are crucial and a curved interactive surface is considered significantly effective.

5 Conclusion

In this study, we designed experiments to evaluate raycasting-based interactive surfaces and measured the percentage of correct answers and the operation time when surface factors were changed in a VE. The results showed that in the curved surface condition, the percentage of correct answers improved in basic and realistic situations, and the operation time was shortened in situations without target-seeking activities.

These findings can be applied to two-dimensional-style applications, such as photo browsers and GIS. For future work, an experiment should be conducted to clarify the effect of out-of-sight target seeking and normalize the difficulty of the target-seeking task.

References

[1] A. Endert, L. Bradel, J. Zeitz, C. Andrews, and C. North, "Designing large high-resolution display workspaces," in *Proceedings of the International Working Conference on Advanced Visual Interfaces*, AVI '12, pp. 58–65. Association for Computing Machinery, New York, NY, USA, 2012. doi: 10.1145/2254556.2254570

[2] B. Gao, B. Kim, J. I. Kim, and H. Kim, "Amphitheater Layout with Egocentric Distance-Based Item Sizing and Landmarks for Browsing in Virtual Reality," in *International Journal of Human–Computer Interaction*, 35(10), 2018. doi: 10.1080/10447318.2018.1498654

[3] J. Liu, A. Prouzeau, B. Ens, and T. Dwyer, "Design and evaluation of interactive small multiples data visualisation in immersive spaces," in *2020 IEEE Conference on Virtual Reality and 3D User Interfaces (VR)*, pp. 588–597, 2020. doi: 10.1109/VR46266.2020. 00081

[4] L. Shupp, R. Ball, B. Yost, J. Booker, and C. North, "Evaluation of viewport size and curvature of large, high-resolution displays," in *Proceedings of Graphics Interface 2006*, GI '06, pp. 123–130. Canadian Information Processing Society, CAN, 2006.

[5] T. Takashina, M. Ito, H. Nagaura, and E. Wakabayashi, "Evaluation of Curved Raycasting-based Interactive Surfaces in Virtual Environments," in *2021 IEEE Conference on Virtual Reality and 3D User Interfaces Abstracts and Workshops (VRW)*, 2021, pp. 534–535, doi: 10.1109/VRW52623.2021.00149

[6] C. Wingrave and D. A. Bowman, "Baseline factors for raycasting selection," in *Proceedings of Virtual Reality International*, p. 10 pgs, 2005.

高階知巳　Tomomi TAKASHINA
映像ソリューション推進室
Imaging Solution Development Department

伊藤　充　Mitsuru ITO
映像ソリューション推進室
Imaging Solution Development Department

長浦　仁　Hitoshi NAGAURA
株式会社ニコンシステム
Nikon Systems Inc.

若林英佑　Eisuke WAKABAYASHI
株式会社ニコンシステム
Nikon Systems Inc.

高階知巳
Tomomi TAKASHINA

長浦　仁
Hitoshi NAGAURA

若林英佑
Eisuke WAKABAYASHI

領域別に適正露光制御可能な高ダイナミックレンジ1型 17 Mpixel 1000 fps 積層CMOSイメージセンサ

平田友希，村田寛信，有井　卓，松田英明，米持　元，手塚洋二郎，綱井史郎

A 1-inch 17 Mpixel 1000 fps Block-Controlled Coded-Exposure Back-Illuminated Stacked CMOS Image Sensor for Computational Imaging and Adaptive Dynamic Range Control†

Tomoki HIRATA, Hironobu MURATA, Taku ARII, Hideaki MATSUDA, Hajime YONEMOCHI, Yojiro TEZUKA and Shiro TSUNAI

人間の知覚を超えた，広い明暗差に対応かつ，高速高解像で画像取得可能なビジョンシステムを提案する．イメージセンサは観賞用カメラだけではなく，ロボットビジョンなど幅広い分野に使われている．例えば自動運転用途では，暗いトンネル内や真夏の日差しの中で，動きに追従して高精細に，かつ高速に物体を認識する必要がある．

しかしながら，1つのカメラで明暗差のある移動被写体を撮る場合，高精細とフレームレート，画素サイズとダイナミックレンジ（DR）にトレードオフの関係があるため，すべての性能を満たすことは困難であった．我々は，4 K×4 Kの解像度で 1000 fps の読み出し動作が可能で，2.7 μm の微細画素でありながら 110 dB の DR を実現する高速ビジョンシステムを開発した．具体的には，高 DR 手法として画素アレイを複数のブロックに分割して個別に露光時間を制御する機能を採用し，ブロック毎に AD 変換器を並列配置することで高速読み出しを実現し，3次元ウェハ積層技術により回路と画素を高密度に集積することでこれらの課題を克服した．本システムは暗い箇所と明るい箇所が画面内に混在するような高 DR が必要な用途に加えて，符号化露光（Coded Exposure）を用いたコンピューテーショナルイメージングへの応用が期待される．

This study introduces a vision system that can acquire images at high speeds and high resolutions. It can handle wide differences in brightness beyond human perception. Image sensors are not only used in digital still cameras but also in a wide range of fields, such as robot vision. Object recognition and movement tracking at high speeds and high definitions are essential in automated driving systems, especially in dark tunnels or in the mid-summer sunshine. However, capturing a moving subject with a high contrast and achieving a high performance concerning all aspects is challenging because of the tradeoff between high definition and high frame rate, and pixel size and dynamic range (DR). We developed a high-speed vision system capable of 1000-fps readout operation at a resolution of 4K x 4K and achieving a DR of 110 dB and fine pixels of 2.7 μm. These characteristics were achieved simultaneously using coded exposure (CE), which divides the image plane into smaller blocks and controls the exposure time of each block individually. A high-speed readout was achieved by arranging analog to digital converters in parallel for each block. A high resolution was realized by integrating both circuits and pixels at a high density using three-dimensional wafer stacking technology. This system is expected to be applied to computational imaging using CE, in addition to applications that require high DR in which dark and bright areas coexist in a scene.

Key words ビジョンシステム，ブロック並列，積層型 CMOS イメージセンサ，高ダイナミックレンジ，高速撮影，符号化露光
vision system, block parallel, stacked CMOS image sensor, high dynamic range, high-speed imaging, coded exposure

1 Introduction

Image sensors are not only used for taking photos but also increasingly expected to serve as intelligent systems with surrounding configurations. Coded exposure (CE) [1], [2] is a method applied in intelligent system approaches, and

† This paper was modified from reference [11], and results and discussions were added on artifacts and application examples.

thus various functions can be realized by selecting an integration variable in the plenoptic function. High dynamic range (HDR) can be realized when the integration variable is time. Various methods have been proposed to achieve HDR. A method, such as a lateral overflow integration capacitor (LOFIC), was introduced that could provide the plurality of detection capacitors [3]. In addition, another method was presented to prevent the photodiode saturation by adding low-sensitivity pixels [4]. However, various proposed methods require an enlarged pixel size. Alternatively, a high-speed readout, such as an array-parallel analog-to-digital converter (ADC) structure [5], is useful for integrating multiple frames [6] to realize an HDR. However, it increases the noise level and requires a faster readout to reduce motion artifacts. To mitigate these adverse effects, a method was proposed in which a pixel array is divided into multiple blocks, and the signal integration time of each block is individually controlled [7]. In another method, CE was demonstrated using the pixel-level control of the exposure time [8]. However, in these methods, the readout path and control circuitry should be arranged within the same plane because these are unstacked sensors; thus, the pixel size is relatively large and high resolution is difficult to realize. Therefore, we designed a sensor that could simultaneously achieve a 4 K × 4 K resolution and a high-speed readout of 1000 fps. Using a stacked structure, we demonstrated the CE capability by individually controlling the exposure time for each block of the pixels.

2 Sensor Architecture

2.1. Block Diagram

Fig. 1 shows a conceptual diagram of the image sensor. This 1-inch image sensor has two layers: the top chip comprises BSI pixels with a 65-nm process and the bottom chip is used for signal processing; the layers are bonded to each other. The highest-density area consists of two contacts per pixel. The top chip has a pixel array (H4224 × V4224, 2.7-μm pitch), which is divided into H264 × V264 exposure control blocks with a basic unit of H16 × V16 pixels. The bottom chip has ADC circuits, logic circuits, high-speed interfaces (HS-IF), and H264 × V132 readout circuits (readout units), which are arranged directly below the pixels. Each readout unit corresponds to H16 × V32 pixels as a basic unit. Pixel signals are converted into parallel digital data using ADC circuits located in each readout unit. Binary conversion and correlated double sampling (CDS) operations are performed using the readout logic located in the bottom chip. Subsequently, signals are outputted through 48 channels of the HS-IF, which operates at 4.8 Gbps per channel.

2.2. Block Array Structure

Fig. 2 shows a diagram of the readout unit and two exposure blocks. Each pixel comprises a photodiode (PD) and five transistors. The reset transistor (RST) and select transistor (SEL) are controlled by a global pixel driver placed in the periphery of the bottom chip. Both the photoelectron transfer transistor (TX1) and PD reset transistor (TX2) are controlled for each block by the local pixel driver in the readout unit. The readout unit is composed of 16 column ADCs, a data transfer circuit, an integration time controller, and a local pixel driver. Moreover, ADC is a 12-bit single slope type, and the ramp signal and counter are supplied from the peripheral circuitry of the bottom chip. Each ADC is con-

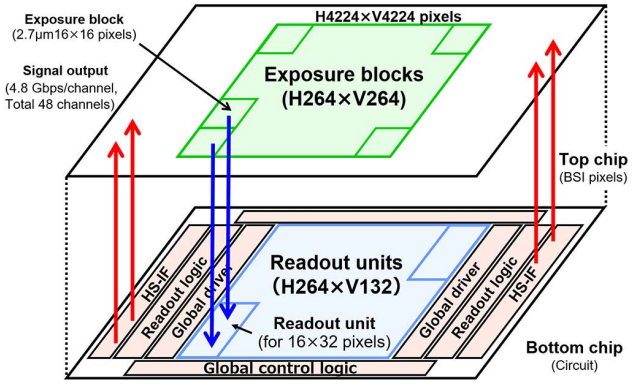

Fig. 1 Device structure

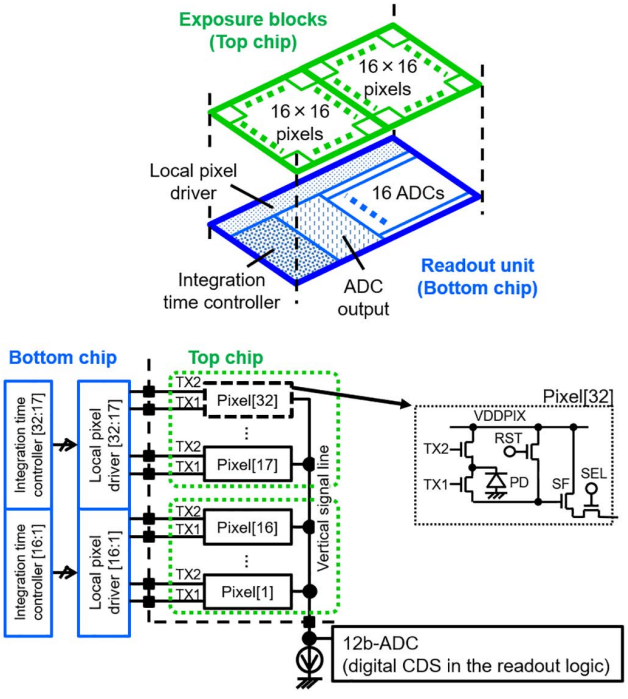

Fig. 2 Exposure block and readout unit

nected to its corresponding pixels (1–32) via a vertical signal line and source followers (SF). The digital signal, converted in ADC, is transferred to the readout logic via the transfer path for each set of 16 columns.

2.3. Exposure Control

The exposure control has two operation modes. One is “No Skip Mode” for short exposure time less than one frame, and the other is “Skip Mode” for long exposure time more than one frame. Fig. 3 shows a simplified block diagram and timing chart of exposure control. The integration time controller comprises a row counter, address decoder, and four flip-flops that hold an exposure time register setting. The register has four bits per block, of which three are used to encode eight different exposure times within one frame. The remaining one bit is a mode select signal, used as a mask signal that skips the reading of photoelectrons. The register can be updated for each frame. TX2 is controlled using the AND logic applied to the eight exposure time settings and timing signal linked with the register. TX1 is controlled using the AND logic of the TX1SEL signal from the global control logic and TX1MASK signal. The local pixel driver, composed of a level shift circuit and driver circuit, scans pixels in a predetermined row based on the decode signal of the integration time controller and SEL signal. Each readout unit is associated with 32 rows of pixels, corresponding to two exposure blocks per frame. In the No Skip Mode, TX1 is sequentially controlled to cross two exposure blocks, and TX2 is independently controlled for each block according to the integration time, as presented by blocks (1,1) and (1,2) in Fig. 3. Short exposure times of one horizontal period or less can be achieved because the controls for TX1 and TX2 are independent. Skip Mode can be realized by skipping the TX1 and TX2 operations using the mask signal, as presented by block (264,263) in Fig. 3. With the above configuration, the exposure time of each block is individually set by the integration time controller, and the rolling shutter reading of 16 × 32 pixels in each unit is performed simultaneously. Each block has an exposure time controller that includes the selection of two operations. The exposure table is changed for each frame. Thus, various exposure patterns can be created in a two-dimensional manner, resulting in HDR imaging.

3 Configuration of the Experimental System

Fig. 4 shows the system configuration. This system comprises a camera head, camera control unit, and host computer (PC). The camera head has a lens unit and image sensor board. The camera control unit is composed of two field programmable gate arrays (FPGA) and a power supply board and functions to control the image sensor, supply power, and receive image data. The PC controls the entire system, processes, and then saves the images.

The image data from the sensor are inputted to each FPGA in the camera control unit via 24 channels at a time. The FPGA adjusts the data rate and data width and transfers data to the PC through the optical fiber.

To calculate the exposure time of each block, we prototyped two types of systems according to the application. The first system is to calculate the exposure time in FPGAs in the camera control unit, assuming that the subject moved at a high speed. The exposure value can be updated in every 8 frames by calculating the exposure value using the pipeline operation without a frame memory. The second system is to

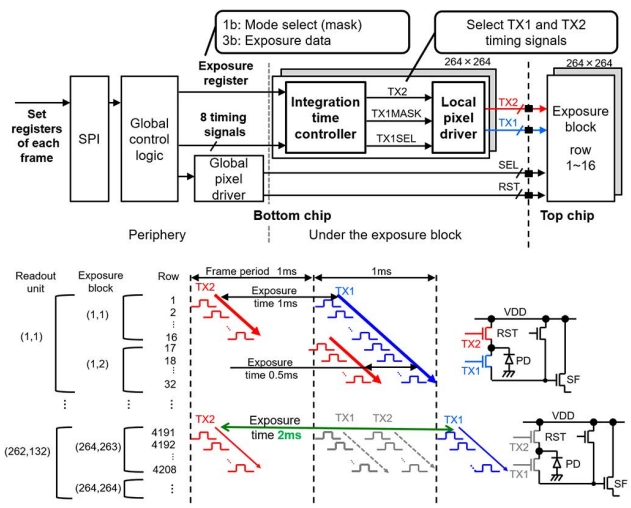

Fig. 3 Block exposure control structure and timing chart

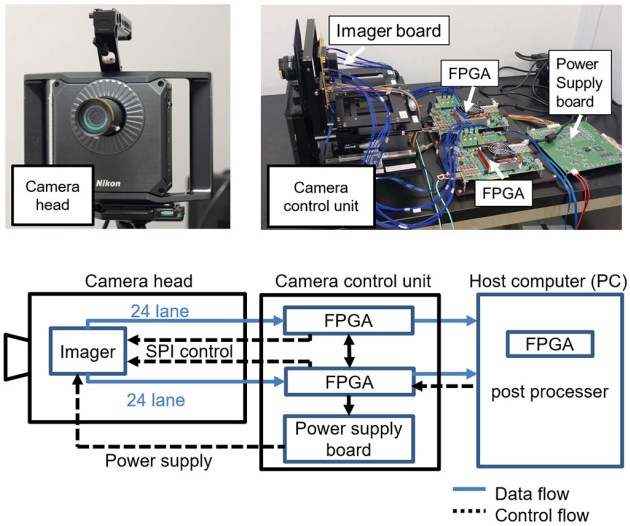

Fig. 4 Camera system architecture

calculate it in PC. More advanced and precise exposure control is possible in case of considering the surrounding blocks or multiple frames.

4 Results and Discussion

4.1. Coded Exposure

Fig. 5 presents the experimental results of CE. To generate an exposure table, the original image was first divided into blocks of 264 × 264, and the average value of each block was converted into 3-bit gradation data. Subsequently, the exposure time was set from 1/128 to 1 ms corresponding to the 3-bit data. The photography was performed on a light box without patterns under a uniform illumination using the exposure table. The block exposure method can produce a coded image in a single shot. Furthermore, setting the exposure time frame-by-frame or across frames yields various coded patterns.

4.2. HDR Imaging

Fig. 6 shows the experimental results for an HDR. The image shown on the left side was obtained by exposure bracketing, which is a conventional technique of taking multiple shots with different exposure times. Moreover, dynamic range (DR) of each image was relatively small where blackouts and whiteouts occurred. Therefore, many images were required, which required a long time to capture. The image on the right side is a HDR image acquired with CE using this sensor and calculated in PC. The sensor was driven at 1000 fps, and the post-processing system and integration

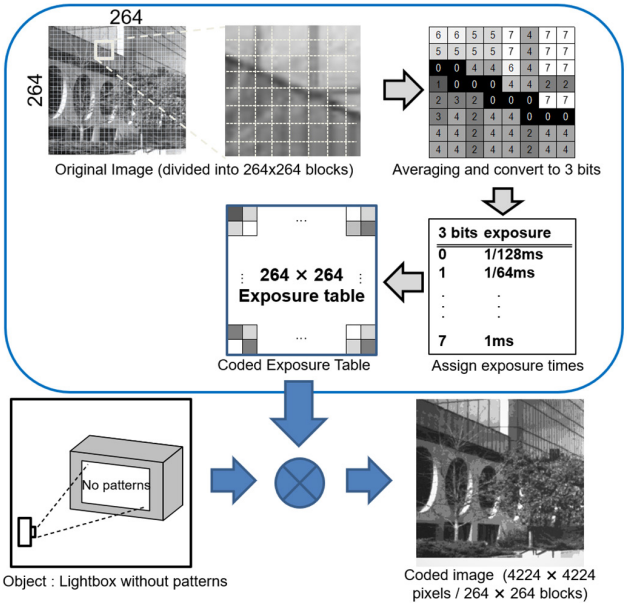

Fig. 5 Experimental results of CE

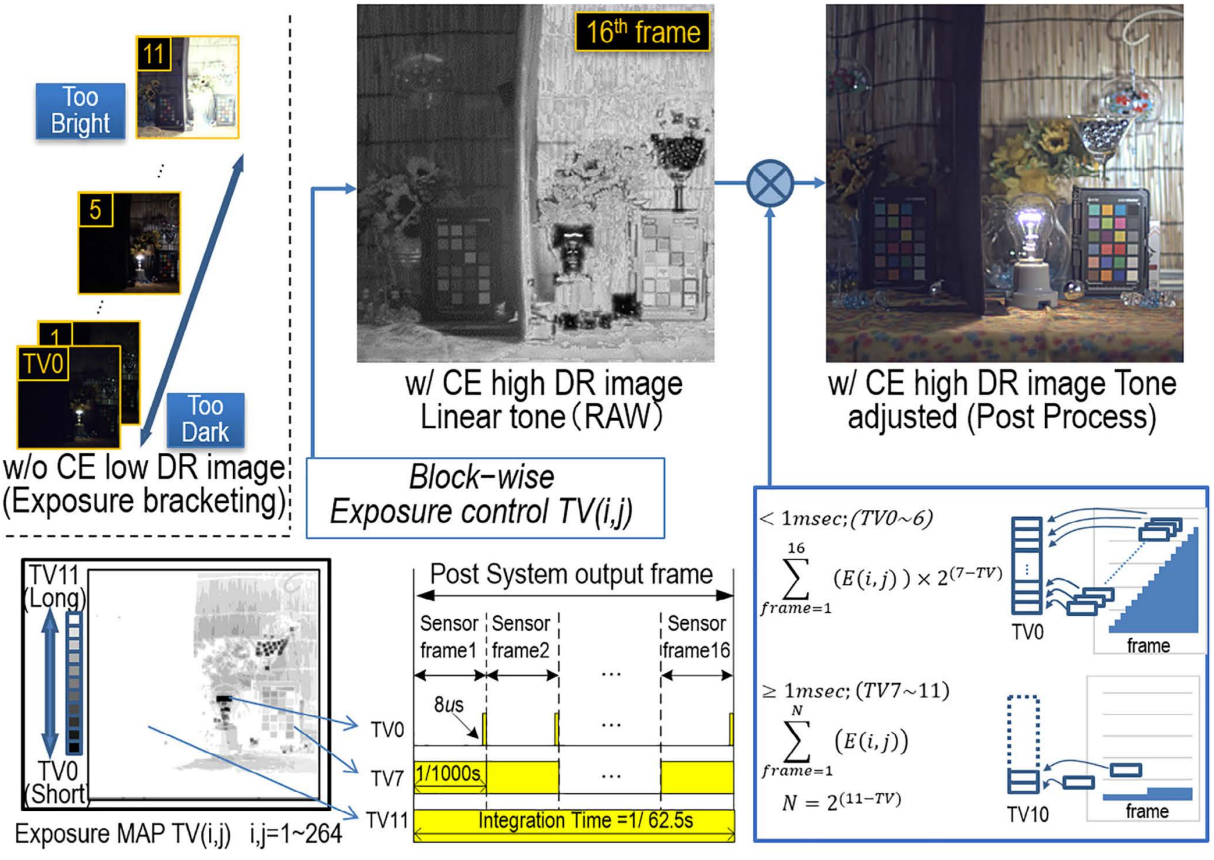

Fig. 6 Experimental results of HDR

time operated in every 16 frames. Image acquisition was performed by changing the exposure time for each block based on the exposure table, indicated by time value (TV), which logarithmically defines the exposure time. The calculation performed multiplication and addition processing of the acquired image according to the TV. Consequently, images with a total of 11 exposure stops can be acquired at a high speed by setting the exposure time for 7 stops within one frame and 4 stops for over a period of 16 frames.

Considering the block steps, if the exposure times of the adjacent blocks are different, the signal-to-noise ratio (SNR) steps occur at the boundary of the blocks. To mitigate the block steps, smoothing the number of stops of the exposure time between adjacent blocks is preferable. In addition, the SNR can be improved by adding multiple frames to the blocks with a short exposure time.

4.3. HDR Tracking for Moving Object

Fig. 7 shows the results of the responsiveness of exposure control to a moving object. The sensor was operated at 1000 fps and an object moved horizontally on the screen. The image on the left was captured without an exposure control. When the object dashes from the dark to bright area of frame #345 with respect to the initial state of frame #1, the characters on the body are oversaturated. The results of dynamic exposure control in every 8 frames are demonstrated on the right side. Updating the exposure table in every 8 frames suppresses the oversaturation of characters on the body and realizes an HDR image.

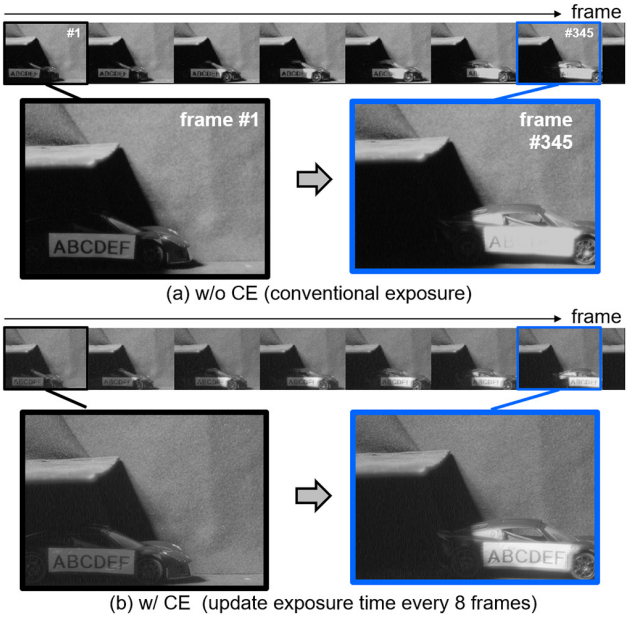

Fig. 7 Experimental results of exposure tracking

4.4. Sensor Specifications

Table 1 presents a comparison between the performance of our sensor with that of other sensors presented in the existing studies. At first, our developed sensor achieves high speed readout with a resolution of 17 Mpixel. In addition, this paper demonstrates HDR with small pixel of 2.7-um pitch. The total power of the sensor was 7.4 W at 1000 fps. The chip micrograph is shown in Fig. 8. Both chips were fabricated using a 65-nm process.

4.5. More Applications Using Coded Exposure

Fig. 9 shows an application that overlays the information

Table 1 Sensor specifications

	This work	IISW2019 [3]	ISSCC2020 [4]	VLSI2017 [5]	IISW2015 [7]	ISSCC2019 [8]
Process	**Stacked BSI Top: 65nm Bottom: 65nm**	BSI 65nm 1P4M	Stacked BSI Top: 90nm/65nm 1P4Cu Bottom: 40nm 1P6Cu1AL	Stacked BSI Top: 90nm 1P4M Bottom: 55nm 1P7M	FSI 0.18μm 1P4M	0.11μm
HDR technology	**Integration time controllable for each block**	LOFIC	Sub-pixel	-	Integration time controllable for each block	Integration time controllable for each pixel
Number of pixels [Mpix]	**17.8**	0.6	5.7	4.1	0.4	0.05
Pixel pitch [μm]	**2.7**	2.8	3.0	4.8	5.0	11.2
Bit depth [bit]	**12**	-	12	-	-	-
Frame rate [fps]	**1000**	-	30	630	-	25
Conversion gain [μV/e-]	**161**	10 (Low) 160 (High)	6.7 (Low) 197 (High)	65	-	-
Random noise [e-]	**2.9**	-	0.6	4.2	-	-
Sensitivity [ke-/lux·s]	**20.7**	-	38.0	28.4	-	-
FWC[ke-]	**7.4**	120.0	165.8	-	-	-
Dynamic-range [dB]	**110 @ 1 frame 134 @ 16frames**	-	132	-	120	-

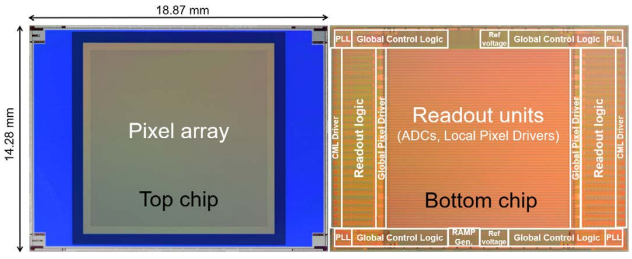

Fig. 8 Chip micrograph

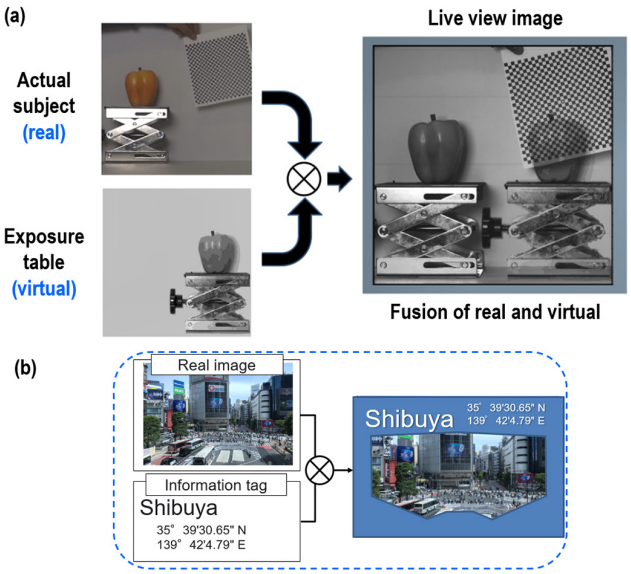

Fig. 9 (a) Experimental results of the overlay information on the real image and (b) an application example of CE

on a real image. Encoding the exposure time for each region implies that an arbitrary virtual pattern can be generated in the image. The experimental result is shown in Fig. 9(a). The photograph on the upper left shows the actual subject. The lower left figure presents an image of the exposure table, where a pseudo image is formed by expressing eight different exposure settings as gradations. The dark area indicates a short exposure, whereas the bright area indicates a long exposure. The results obtained using this exposure map are illustrated on the right side. It can be observed that a virtual image is embedded in the subject in the real space. In addition, this exposure table is created based on an actual subject; that is, it can also be used as an image-recording function.

Fig. 9(b) shows an application, where it is possible to embed tag information or a head-mounted display for virtual or augmented reality [9], [10]. Overlaying them on the image sensor reduces the processing power of the subsequent system and improves latency.

5 Conclusions

In this study, we have newly developed a CMOS image sensor with a stack structure that operates at 1000 fps while having a high resolution of 17 Mpixel with small pixel of 2.7-um pitch. By using the block-wise coded exposure function, 110 dB DR is achieved at 1000 fps in a single frame, and 134 dB DR in 16 frames. This vision system can be applied to various computational imaging using the coded exposure function, in addition to high dynamic range imaging in scenes where dark and bright areas of the subject are mixed in the frame.

Acknowledgements. The authors would like to thank all engineers at the Nikon Corporation Advanced Technology Research & Development Division, Opto Device Development Center, and Mathematical Sciences Research Laboratory for their support in this work.

References

[1] R. Raskar, et al., "Coded exposure photography: Motion deblurring using fluttered shutter," *ACM SIGGRAPH* 2006 Papers, SIGGRAPH '06, 2006, pp. 795–804.

[2] Y. Hitomi, et al., "Video from a single coded exposure photograph using a learned over-complete dictionary," *IEEE ICCV*, 2011, pp. 287–294.

[3] K. Miyauchi, et al., "A high optical performance 2.8 μm BSI LOFIC pixel with 120ke FWC and 160 μV/e conversion gain," in *Proc. Int. Image Sensor Workshop*, 2019.

[4] Y. Sakano, et al., "A 132dB single-exposure-dynamic-range CMOS image sensor with high temperature tolerance," in *IEEE Int. Solid-State Circuits Conf. (ISSCC) Dig. Tech. Papers*, San Francisco, CA, USA, Feb. 2020, pp. 106–108.

[5] T. Takahashi, et al., "A 4.1Mpix 280fps stacked CMOS image sensor with array-parallel ADC architecture for region control," in *Proc. IEEE Symp. VLSI Circuits*, Jun. 2017, pp. 244–245.

[6] S. Velichko, et al., "140 dB dynamic range sub-electron noise floor image sensor," in *Proc. Int. Image Sensor Workshop*, 2017.

[7] A. Peizerat, et al., "A 120dB DR and 5μm pixel pitch imager based on local integration time adaptation," in *Proc. Int. Image Sensor Workshop*, 2015.

[8] N. Sarhangnejad, et al., "Dual-tap pipelined-code-memory coded-exposure-pixel CMOS image sensor for multi-exposure single-frame computational imaging," in *IEEE Int. Solid-State Circuits Conf. (ISSCC) Dig. Tech. Papers*, San Francisco, CA, USA, Feb. 2019, pp. 102–104.

[9] J. Wang, et al., "Augmented reality navigation with automatic marker-free image registration using 3-d image overlay for dental surgery," *IEEE Transaction on Biomedical engineering*, 2014, vol. 61, no. 4, pp. 1295–1304.

[10] H. Hile and G. Borriello, "Positioning and orientation in indoor environments using camera phones," *IEEE Computer Graphics and Applications*, 2008, vol. 28. no. 4, pp. 32–39.

[11] T. Hirata, et al., "A 1-inch 17Mpixel 1000fps block-controlled coded-exposure back-illuminated stacked CMOS image sensor for computational imaging and adaptive dynamic range control," in *IEEE Int. Solid-State Circuits Conf. (ISSCC) Dig. Tech. Papers*, Feb. 2021, pp. 120–121.

平田友希　Tomoki HIRATA
先進技術開発本部　光デバイス開発センター
Opto Device Development Center
Advanced Technology Research & Development Division

村田寛信　Hironobu MURATA
先進技術開発本部　光デバイス開発センター
Opto Device Development Center
Advanced Technology Research & Development Division

有井　卓　Taku ARII
先進技術開発本部　光デバイス開発センター
Opto Device Development Center
Advanced Technology Research & Development Division

松田英明　Hideaki MATSUDA
先進技術開発本部　光デバイス開発センター
Opto Device Development Center
Advanced Technology Research & Development Division

米持　元　Hajime YONEMOCHI
先進技術開発本部　光デバイス開発センター
Opto Device Development Center
Advanced Technology Research & Development Division

手塚洋二郎　Yojiro TEZUKA
先進技術開発本部　光デバイス開発センター
Opto Device Development Center
Advanced Technology Research & Development Division

綱井史郎　Shiro TSUNAI
先進技術開発本部　光デバイス開発センター
Opto Device Development Center
Advanced Technology Research & Development Division


平田友希
Tomoki HIRATA


村田寛信
Hironobu MURATA


有井　卓
Taku ARII


松田英明
Hideaki MATSUDA


米持　元
Hajime YONEMOCHI


手塚洋二郎
Yojiro TEZUKA


綱井史郎
Shiro TSUNAI

エシェロンミラーを用いた高スループットなテラヘルツ分光ラインイメージング

浅井　岳，秦　大樹，原田真太郎，笠井達基，嵐田雄介，片山郁文

High-throughput Terahertz Spectral Line Imaging using an Echelon Mirror†

Gaku ASAI, Daiki HATA, Shintaro HARADA, Tatsuki KASAI, Yusuke ARASHIDA and Ikufumi KATAYAMA

本研究では，エシェロンミラーを用いたシングルショットテラヘルツ（THz）分光法と位相オフセット電気光学検出を組み合わせることにより，広帯域スペクトル情報を高感度に取得するテラヘルツ分光ラインイメージングを提案する．計測用カメラの単一ラインから得られるテラヘルツ帯スペクトル情報に対して，約 40 dB の信号対雑音比が得られ，1.2 kV/cm のピーク電場強度で最大 2 THz の帯域を検出できることを確認した．ラインイメージングにおける空間分解能は，テラヘルツ波のスペクトル成分ごとに回折限界程度であることが確認されている．今回提案したテラヘルツ分光ラインイメージングシステムにおいてサンプルを高速にスキャンすることで，二糖類（ラクトース，スクロース）の錠剤の成分分析・イメージングや樹脂サンプル等の膜厚・形状計測が可能となり，高いスループットで分光イメージングが可能であることを示した．

This work demonstrates terahertz (THz) line imaging that acquires broadband spectral information by combining echelon-based single-shot THz spectroscopy with high-sensitivity phase-offset electrooptic detection. A signal-to-noise ratio of approximately 40 dB is obtained for a THz spectrum from a single line of a camera with a detection bandwidth of up to 2 THz at the peak electric-field strength of 1.2 kV/cm. The spatial resolution of the image is confirmed to be diffraction limited for each spectral component of the THz wave. We use the system to image sugar tablets (lactose, sucrose) and film thickness/shape measurement of resin samples through a shield by quickly scanning the sample, which illustrates the capacity of the proposed spectral line imaging system for high-throughput applications.

Key words テラヘルツ波，超高速分光，イメージング，非破壊検査，高感度検出
terahertz wave, ultrafast spectroscopy, imaging, non-destructive inspection, high sensitivity detection

1 Introduction

Terahertz (THz) imaging is one of the most important applications of THz science and technology. It can be used to map materials that are difficult to distinguish using other frequency regimes [1], [2]. The material properties that can be detected using THz imaging include polymorphisms of organic materials [3], strain in rubbers [4], refractive indices of chemicals and proteins [5], [6], pigments in artificial paints [7], carriers in semiconductors [8], and foams in polymeric materials [9]. For these imaging applications, researchers have used THz cameras from microbolometers [10], THz CMOS cameras [11], and up-conversion to the near-infrared or visible range [12], etc. Although spectral information is fundamentally crucial for this technology, obtaining complete spectral information using these techniques is difficult and time-consuming.

An advanced technique for THz imaging is THz time-domain spectroscopy (THz-TDS), which uses ultrashort laser pulses and offers an important advantage over competing techniques [13], [14]. Because THz-TDS acquires the full temporal waveform of the THz transients, it can provide a precise broadband spectrum. However, increasing the measurement throughput is difficult because the temporal domain must be scanned to acquire the full waveform of the THz pulses, in addition to the spatial dimensions normally required for THz imaging.

Recently, significant efforts have been devoted to circumvent this difficulty by developing single-shot THz-TDS [15]–[17]. Yasui *et al.* used oblique crossings of THz waves and

† This paper was modified from reference [27] and added the result of thickness imaging of resin films as Fig. 5.

probe pulses in an electro-optic (EO) crystal to demonstrate single-shot THz line imaging [18]. However, the oblique-crossing technique requires a large EO crystal to map out sufficient temporal information; more importantly, the temporal information can be distorted by spatial inhomogeneities in the EO crystal and/or by scattered THz waves because different temporal information comes from different parts of the crystal.

The reflective echelon technique uses a stair-step mirror to map the temporal information to spatial positions on the mirror and allows us to focus the probe pulses on the EO crystal, which can reduce the distortion of the temporal waveforms [19], [20]. THz-TDS in a pulsed magnetic field and Kerr-gate spectroscopy have already been demonstrated using this method and have illustrated the precise acquisition of the temporal waveform and the corresponding spectrum [21]–[23]. In this study, we combine this technique based on an echelon mirror with a phase-offset method to enhance electric-field detection [24], and we implement the system in an imaging system to realize high-throughput line imaging.

2 Experiments

Fig. 1 summarizes the system used in this study. We used a Ti: sapphire regenerative amplifier with an output power of 1 mJ, center wavelength of 800 nm, and repetition rate of 1 kHz to generate and detect THz waves. Part of the laser output was used to pump the $LiNbO_3$ prism with a wavefront tilt to efficiently generate an intense THz wave [25], [26], which was subsequently collimated by using a spherical lens placed after the $LiNbO_3$ prism and linearly focused onto the sample with a cylindrical lens. Next, the THz image of the sample was transferred to the detection EO crystal, which detected the birefringence induced by the THz electric field and spatial distribution.

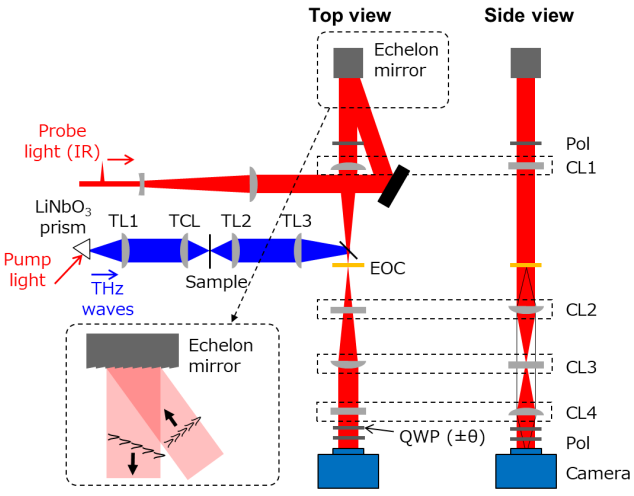

Fig. 1 Experimental setup for THz spectral line imaging using an echelon mirror. TL: THz Tsurupika lenses, TCL: THz cylindrical lens, CL: cylindrical lenses, EOC: electro-optic crystal, Pol: polarizers, QWP: quarter wave plate.

The remaining laser output of approximately 50 mW was used to probe the electric field distribution on the EO crystal, which was 1-mm-thick (110) ZnTe. The probe was reflected from an echelon mirror with a step width of 25 μm and step height of 2.5 μm, and linearly focused onto the crystal to cover the focal line of the THz wave. The number of steps on the echelon surface was 750. Because each segment of the echelon mirror reflects the probe pulse at different delay times (see inset of Fig. 1), the temporal information is mapped to the horizontal axis of the THz camera (16 bit, 2560 × 2160 pixels with a pixel size of 6.5 × 6.5 μm^2; full-well capacity of the camera was 30000 e-) upon imaging the echelon surface onto the camera. We used a set of cylindrical lenses after the EO crystal to image spatial information in the vertical direction. Using these setups, our system becomes scanless in THz spectral line imaging, which conventionally requires 2D scanning.

Because the THz pulses are linearly focused in our system, the electric field strength at the focus is less than that in other THz-TDS systems that use tightly focused THz pulses. To compensate for this reduced electric field strength, we enhanced the sensitivity of the EO sampling to obtain line imaging with a large signal-to-noise ratio (SNR). Here, we used the phase-offset method in the detection setup [24], and placed an EO crystal between the crossed polarizers and quarter wave plate with a slight offset rotation.

To describe the detection mechanism, we first write the Jones vector E_{in} of the incident probe pulse as:

$$E_{in} = \begin{pmatrix} E_x \\ E_y \end{pmatrix} = \begin{pmatrix} E_0 \\ 0 \end{pmatrix}. \quad (1)$$

The Jones matrix of modulated EO crystal is

$$J_{EO} = \begin{pmatrix} \cos\frac{\Delta}{2} & i\sin\frac{\Delta}{2} \\ i\sin\frac{\Delta}{2} & \cos\frac{\Delta}{2} \end{pmatrix}, \quad (2)$$

where Δ is the THz field-induced phase difference between the probe pulses. The Jones matrix of the offset quarter wave plate is

$$J_{\frac{\pi}{4}} = \begin{pmatrix} \cos\theta & -\sin\theta \\ \sin\theta & \cos\theta \end{pmatrix} \begin{pmatrix} e^{i\frac{\pi}{4}} & 0 \\ 0 & e^{-i\frac{\pi}{4}} \end{pmatrix} \begin{pmatrix} \cos\theta & \sin\theta \\ -\sin\theta & \cos\theta \end{pmatrix} = \frac{1}{\sqrt{2}} \begin{pmatrix} 1+i\cos 2\theta & i\sin 2\theta \\ i\sin 2\theta & 1-i\cos 2\theta \end{pmatrix}, \quad (3)$$

where θ is the angle of rotation in the 001 direction of the EO crystal. After the crossed analyzer polarizer, the output signal is

$$E_{\text{out}} = J_{\text{pol}} J_{\frac{\pi}{4}} J_{\text{EO}} E_{\text{in}} = \frac{E_0}{\sqrt{2}} \begin{pmatrix} 0 & 0 \\ 0 & 1 \end{pmatrix} \begin{pmatrix} 1+i\cos 2\theta & i\sin 2\theta \\ i\sin 2\theta & 1-i\cos 2\theta \end{pmatrix} \begin{pmatrix} \cos\frac{\Delta}{2} \\ i\sin\frac{\Delta}{2} \end{pmatrix} = \frac{E_0}{\sqrt{2}} \begin{pmatrix} 0 \\ i\sin 2\theta\cos\frac{\Delta}{2} + i\sin\frac{\Delta}{2} + \cos 2\theta\sin\frac{\Delta}{2} \end{pmatrix}. \quad (4)$$

The intensity of the signal is then

$$I(\theta,\Delta) = |E_{\text{out}}|^2 = \tfrac{1}{2}|E_0|^2 \left(\sin^2 2\theta\cos^2\tfrac{\Delta}{2} + \sin^2\tfrac{\Delta}{2} + \sin 2\theta\sin\Delta + \cos^2 2\theta\sin^2\tfrac{\Delta}{2}\right). \quad (5)$$

To eliminate the quadratic terms in this equation, we subtracted the data with the opposite phase offset to obtain

$$\frac{I(\theta,\Delta) - I(-\theta,\Delta)}{I(\theta,0)} = \frac{\Delta I}{I(\theta,0)} = \frac{2\sin\Delta}{\sin 2\theta}. \quad (6)$$

This equation ensures a one-to-one correspondence between the signal intensity and the electric field strength. Furthermore, enhancing the sensitivity of the measurement is possible by only changing the rotation angle θ of the QWP.

3 Results

Fig. 2(a) and 2(b) show the images obtained with the THz pulses at phase-offset angles of + 2° and −2°, respectively, with an exposure time of 50 ms. The images clearly show the THz pulses forming into a stripe pattern, with the two offset angles producing opposite polarities. Fig. 2(c) and 2(d) show the linear profiles taken along the 700th line of the images shown in Fig. 2(a) and 2(b), respectively, produced by calculating

$$\Delta I / I = (I_{\text{THzon}} - I_{\text{THzoff}}) / I_{\text{THzoff}}. \quad (7)$$

Using Eq. (6) to estimate the electric field, we subtracted the waveform with a negative phase offset from that with a positive phase offset to calculate the electric field strength, as shown in Fig. 2(e). Although the data were from a single line of the camera with no spatial averaging, the THz waveform obtained had a reasonable SNR.

Owing to the phase-offset method, we can use the full dynamic range of the camera for THz detection to enhance sensitivity. In contrast, if we use the QWP set at 45° for detection, as in the normal EO sampling method, we can use only 5% of the dynamic range, which results in a much worse SNR (typically 20 dB lower than SNR of the phase offset method if the THz electric field strength is similar to this work). Further enhancing the SNR may be possible if we simultaneously obtain signals with positive and negative phase offsets [16], [22]. The single-shot acquisition of an image can be demonstrated if we use a much higher power for the probe, although the data are not shown here.

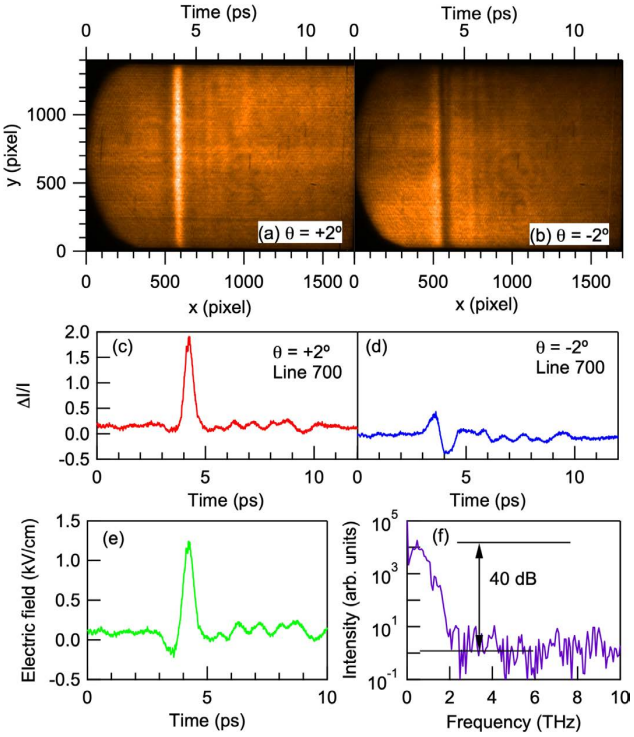

Fig. 2 THz spectral line imaging. Images taken with phase offset of (a) + 2° and (b) −2°. (c) and (d) are the vertical line profiles of the images shown in panels (a) and (b), respectively. (e) THz waveform obtained by subtracting the data of panel (d) from that of panel (c). (f) Fourier transform of panel (e).

Fig. 2(f) shows the Fourier transform of the line shown in Fig. 2(e). The spectrum of the THz wave clearly indicates that spectroscopy is possible for each pixel of the camera up to 2 THz. The SNR of this line reached 40 dB, which is very promising for THz line imaging with spectroscopic resolution. The SNR is determined primarily by the shot noise of the camera. The maximum count of the image can be set to approximately several 10000, which leads to an SNR of 100 for the electric field strength, and, thus, 40 dB for the intensity spectrum. Note that vertically averaging over several lines within the diffraction limit further increases the SNR. The results clearly demonstrate the possibility of enhancing

the throughput of THz imaging because we only need to scan one dimension (horizontal direction in our setup) to obtain full 2D information on the transmitted THz waveform at each point of the sample. The spectroscopic information acquired by this system allows us to both analyze materials with different characteristic THz absorptions and investigate the modifications of the spectrum in the THz range.

To demonstrate and characterize the imaging performance of the system, we measured the spatial resolution of the imaging system by blocking one part of the object plane with a metal plate. Fig. 3(a) shows a typical result of such an experiment, with the metal plate blocking part of the vertical extent of the image to characterize the spatial resolution in the vertical direction. In addition to the vertical lines that correspond to the incident THz pulses, we observed several non-vertical lines that originated from the edges of the metal plate. These correspond to THz pulse diffraction from the edge of the metal plate and the formation of interference patterns.

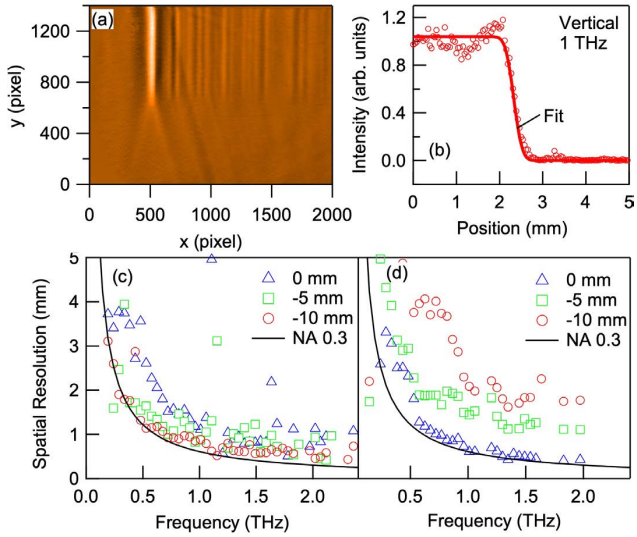

Fig. 3 (a) THz line image acquired with a metal plate blocking the bottom half of the object plane. (b) Vertical line profile of the measured THz wave at 1 THz. (c) Vertical and (d) horizontal spatial resolutions as a function of frequency estimated from the fitting shown in (b). Blue triangles, green rectangles, and red circles are the estimated spatial resolutions when the metal plate was placed just at the focus of the THz wave (0 mm), 5 mm, and 10 mm closer to the TCL, respectively. The solid line is the calculated spatial resolution considering the numerical aperture (0.3) of our setup.

The spatial resolution was estimated by fitting the vertical profile for each frequency component using the error function

$$I_0\{1+\mathrm{erf}[2\sqrt{\ln 2}(x-x_0)/d]\}/2, \quad (8)$$

as shown in Fig. 3(b), where x_0 is the central position of the THz wave, I_0 is the THz intensity, and d is the spatial resolution of the system. To characterize the horizontal resolution, we scanned the metal plate horizontally and examined the decrease in spectral intensity as a function of the position of the metal plate. The data were fitted to an error function to estimate the horizontal spatial resolution.

Fig. 3(c) and 3(d) show the vertical and horizontal spatial resolutions estimated from the width of the error function as a function of frequency. The black curve represents the diffraction limit of the system, calculated by assuming an estimated numerical aperture of 0.3. The data obtained with the metal plate not at the focal plane are also plotted. These results were consistent with those of the measured spatial resolution of the system, although the data for the vertical direction were slightly worse than those of the diffraction limit. This difference may be caused by a slight misalignment of the system, especially the focusing lens, before the sample. Because the imaging system was designed with spherical lenses, the spatial resolutions for the horizontal and vertical directions were the same, even though the sample was illuminated with a cylindrical lens.

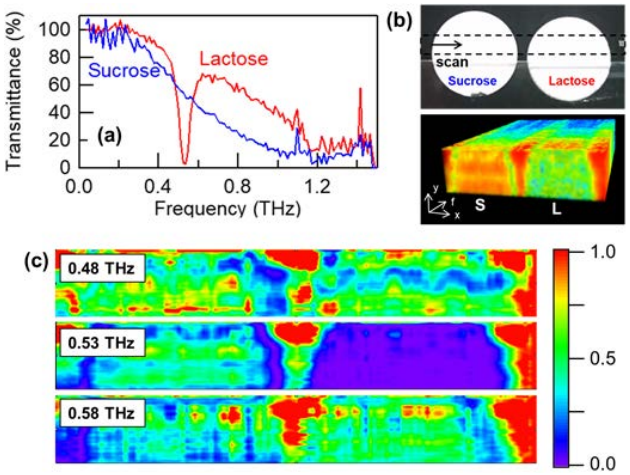

Fig. 4 (a) Transmittance spectra of the sucrose and lactose tablets. (b) Picture of the disaccharide tablets under investigation. The lower part shows the full spectral absorption image plotted in color for 3D. (c) Slices of the 3D transmittance data taken at indicated frequencies.

Next, to demonstrate spectral line imaging, we prepared two disaccharide tablets with different spectral characteristics in the THz region, as shown in Fig. 4(a). Lactose has a characteristic absorption at 0.53 THz, whereas sucrose only has a smooth absorption up to 1 THz. We scanned the sample shown in Fig. 4(b) in the horizontal direction, and data for a width of approximately 36 mm and height of approxi-

mately 5 mm were obtained. The vertical direction (y-axis) was imaged using the line-imaging system. The obtained full spectral imaging data plotted as a 3D image are shown in the lower part of Fig. 4(b). Fig. 4(c) shows the slices of the data at several frequencies: 0.48 THz, 0.53 THz, 0.58 THz. The data clearly show the difference in the absorption at 0.53 THz between two tablets where strong absorption of lactose exists.

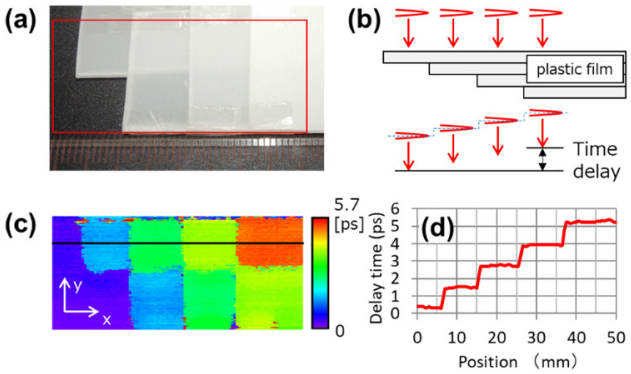

Fig. 5 (a) Picture of plastic film samples of different thickness (measurement range is in the red frame). (b) Conceptual diagram of the principle of thickness measurement. (c) Distribution of delay time transmitted through plastic film. (d) Cross-sectional graph on the black line.

Finally, to demonstrate the advantages of time-resolved spectroscopic imaging, an example of thickness imaging of a resin film that is opaque to visible light is presented. As shown in Fig. 5(a), samples with different numbers of films depending on the position were prepared and measured using the spectroscopic line-imaging system proposed in this paper. As shown in Fig. 5(b), the delay time $\tau(= nd/c)$ of the THz pulse changes depending on the thickness of the transmitted sample. Therefore, the film thickness is obtained by extracting the peak value of the time waveform acquired by time-domain spectroscopy (n: refractive index in the THz region, d: film thickness, c: speed of light). Fig. 5(c) shows a thickness map wherein the delay time is plotted for film samples of different thicknesses. Fig. 5(d) shows a cross-sectional graph on the black line (equivalent to an optical path length difference of 300 μm per 1 ps delay time).

These figures show that the step difference due to the change in the number of films is well represented. Using time-resolved spectroscopic imaging, the transmitted thickness imaging of a sample that is opaque to visible light was demonstrated and it was shown to be a promising means for measuring the 3D and film thickness of resins and ceramics in the future.

The results shown in Fig. 4 and Fig. 5 indicate that spectral line imaging using an echelon mirror is very promising for future industrial and scientific applications. A 3D color image of the sample is of essential importance for comparing and distinguishing materials with different THz responses. Using our imaging system, spectral information is obtained on a single-shot basis, which can avoid distorting the THz waveform due to temporal fluctuations, such as changes in the spectrum or position of the sample. Additionally, combining our system with a compressive sampling technique to expand the spatial dimensions of the imaging is possible. The full and reliable spectral information in the THz region obtainable in our system can be the key to realizing such applications in the future.

4 Conclusion

In summary, we demonstrated spectral line imaging by combining a single-shot THz detection technique using an echelon mirror with the phase offset method. The obtained SNR of the single line reached 40 dB, thereby offering a sufficient dynamic range for spectroscopy applications. The spatial resolutions in both the horizontal and vertical directions were comparable to the diffraction limit of the THz waves at each frequency component. The results obtained from the imaging of disaccharide tablets demonstrate the high potential of spectral line imaging for future applications.

References

[1] M. Tonouchi, "Cutting-edge terahertz technology," *Nat. Photonics*, vol. 1, no. 2, pp. 95–105, 2007.

[2] H. Guerboukha, K. Nallappan, and M. Skorobogatiy, "Toward real-time terahertz imaging," *Adv. Opt. Photonics*, vol. 10, no. 4, pp. 843–938, 2018.

[3] K. Ajito, Y. Ueno, H.-J. Song, E. Tamechika, and N. Kukutsu, "Terahertz Spectroscopic Imaging of Polymorphic Forms in Pharmaceutical Crystals," *Mol. Cryst. Liquid Cryst.*, vol. 539, no. 1, pp. 33–38, 2011.

[4] A. Moriwaki, M. Okano, and S. Watanabe, "Internal triaxial strain imaging of visibly opaque black rubbers with terahertz polarization spectroscopy," *APL Photonics*, vol. 2, no. 10, 106101, 2017.

[5] K. Kawase, Y. Ogawa, Y. Watanabe, and H. Inoue, "Non-destructive terahertz imaging of illicit drugs using spectral fingerprints," *Opt. Express*, vol. 11, no. 20, pp. 2549–2554, 2003.

[6] X. Han, S. Yan, Z. Zang, D. Wei, H. L. Cui, and C. Du, "Label-free protein detection using terahertz time-domain spectroscopy," *Biomed. Opt. Express*, vol. 9, no. 3, pp. 994–1005, 2018.

[7] K. Fukunaga, N. Sekine, I. Hosako, N. Oda, H. Yoneyama, and T. Sudou, "Real-time terahertz imaging for art conservation science," *J. Euro. Opt. Soc*., vol. 3, 08027, 2008.

[8] A. J. Huber, F. Keilmann, J. Wittborn, J. Aizpurua, and R. Hillenbrand, "Terahertz Near-Field Nanoscopy of Mobile Carriers in Single Semiconductor Nanodevices," *Nano Lett*., vol. 8, no. 11, pp. 3766–3770, 2008.

[9] D. J. Roth, S. Reyes-Rodriguez, D. A. Zimdars, R. W. Rauser, and W. W. Ussery, "Terahertz computed tomography of NASA thermal protection system materials," in *AIP Conf. Proc*., vol. 1430, p. 566, 2012.

[10] J. Oden, J. Meilhan, J. Lalanne-Dera, J.-F. Roux, F. Garet, J.-L. Coutaz, and F. Simoens, "Imaging of broadband terahertz beams using an array of antenna-coupled microbolometers operating at room temperature," *Opt. Express*, vol. 21, no. 4, pp. 4817–4825, 2013.

[11] F. Schuster, D. Coquillat, H. Videlier, M. Sakowicz, F. Teppe, L. Dussopt, B. Giffard, T. Skotnicki, and W. Knap, "Broadband terahertz imaging with highly sensitive silicon CMOS detectors," *Opt. Express*, vol. 19, no. 8, pp. 7827–7832, 2011.

[12] P. Bai, Y. Zhang, T. Wang, Z. Fu, D. Shao, Z. Li, W. Wan, H. Li, J. Cao, X. Guo, and W. Shen, "Broadband THz to NIR up-converter for photon-type THz imaging," *Nat. Commun*., vol. 10, no. 1, 3513, 2019.

[13] B. Ferguson and X.-C. Zhang, "Materials for terahertz science and technology," *Nat. Mater*., vol. 1, no. 1, pp. 26–33, 2002.

[14] T. Kampfrath, K. Tanaka, and K. A. Nelson, "Resonant and nonresonant control over matter and light by intense terahertz transients," *Nat. Photonics*, vol. 7, no. 9, pp. 680–690, 2013.

[15] Z. Jiang and X.-C. Zhang, "Electro-optic measurement of THz field pulses with a chirped optical beam," *Appl. Phys. Lett*., vol. 72, no. 16, pp. 1945–1947, 1998.

[16] S. M. Teo, B. K. Ofori-Okai, C. A. Werley, and K. A. Nelson, "Invited Article: Single-shot THz detection techniques optimized for multidimensional THz spectroscopy," *Rev. Sci. Instrum*., vol. 86, no. 5, 051301, 2015.

[17] Z.-H. Zhai, S.-C. Zhong, J. Li, L.-G. Zhu, K. Meng, J. Li, Q. Liu, Q.-X. Peng, Z.-R. Li, and J.-H. Zhao, "Time-resolved single-shot terahertz time-domain spectroscopy for ultrafast irreversible processes," *Rev. Sci. Instrum*., vol. 87, no. 9, 095101, 2016.

[18] T. Yasui, K.-I. Sawanaka, A. Ihara, E. Abraham, M. Hashimoto, and T. Araki, "Real-time terahertz color scanner for moving objects," *Opt. Express*, vol. 16, no. 2, pp. 1208–1221, 2008.

[19] Y. Minami, Y. Hayashi, J. Takeda, and I. Katayama, "Single-shot measurement of a terahertz electric-field waveform using a reflective echelon mirror," *Appl. Phys. Lett*., vol. 103, no. 5, 051103, 2013.

[20] I. Katayama, H. Sakaibara, and J. Takeda, "Real-Time Time-Frequency Imaging of Ultrashort Laser Pulses Using an Echelon Mirror," *Jpn. J. Appl. Phys*., vol. 50, no. 10, 102701, 2011.

[21] X. Li, K. Yoshioka, M. Xie, G. T. Noe, W. Lee, N. Marquez Peraca, W. Gao, T. Hagiwara, O. S. Handegard, L.-W. Nien, T. Nagao, M. Kitajima, H. Nojiri, C.-K. Shih, A. H. MacDonald, I. Katayama, J. Takeda, G. A. Fiete, and J. Kono, "Terahertz Faraday and Kerr rotation spectroscopy of Bil-xSbx films in high magnetic fields up to 30 tesla," *Phys. Rev. B*, vol. 100, no. 11, 115145, 2019.

[22] G. T. Noe, I. Katayama, F. Katsutani, J. J. Allred, J. A. Horowitz, D. M. Sullivan, Q. Zhang, F. Sekiguchi, G. L. Woods, M. C. Hoffmann, H. Nojiri, J. Takeda, and J. Kono, "Single-shot terahertz time-domain spectroscopy in pulsed high magnetic fields," *Opt. Express*, vol. 24, no. 26, pp. 30328–30337, 2016.

[23] G. Mead, I. Katayama, J. Takeda, and G. A. Blake, "An echelon-based single shot optical and terahertz Kerr effect spectrometer," *Rev. Sci. Instrum*., vol. 90, no. 5, 053107, 2019.

[24] J. Degert, M. Cornet, E. Abraham, and E. Freysz, "Simple and distortion-free optical sampling of terahertz pulses via heterodyne detection schemes," *J. Opt. Soc. Am. B*, vol. 33, no. 10, pp. 2045–2050, 2016.

[25] J. Hebling, G. Almasi, I. Z. Kozma, and J. Kuhl, "Velocity matching by pulse front tilting for large-area THz-pulse generation," *Opt. Express*, vol. 10, no. 21, pp. 1161–1166, 2002.

[26] H. Hirori, A. Doi, F. Blanchard, and K. Tanaka, "Single-cycle terahertz pulses with amplitudes exceeding 1 MV/cm generated by optical rectification in $LiNbO_3$," *Appl. Phys. Lett*., vol. 98, no. 9, 091106, 2011.

[27] G. Asai, D. Hata, S. Harada, T. Kasai, Y. Arashida and I. Katayama, "High-throughput terahertz spectral line imaging using an echelon mirror," *Opt. Express*, vol. 29, no. 3, pp. 3515–3522, 2021.

浅井　岳　Gaku ASAI
光学本部 要素開発部
Fundamental Technology Development Department
Optical Engineering Division

秦　大樹　Daiki HATA
光学本部 要素開発部
Fundamental Technology Development Department
Optical Engineering Division

原田真太郎　Shintaro HARADA
横浜国立大学
Yokohama National University

笠井達基　Tatsuki KASAI
横浜国立大学
Yokohama National University

嵐田雄介　Yusuke ARASHIDA
筑波大学
University of Tsukuba

片山郁文　Ikufumi KATAYAMA
横浜国立大学
Yokohama National University


浅井　岳
Gaku ASAI


秦　大樹
Daiki HATA


原田真太郎
Shintaro HARADA


笠井達基
Tatsuki KASAI


嵐田雄介
Yusuke ARASHIDA


片山郁文
Ikufumi KATAYAMA

ミストデポジションと高水分散性 ITO ナノ粒子によるフレキシブル基板上への高性能 ITO 薄膜の作製

鈴木涼子，西　康孝，松原正樹，村松淳司，蟹江澄志

Fabrication of High-Performance ITO Flexible Thin Films Utilizing Mist Deposition and ITO Nanoparticles with High Water Dispersibility†

Ryoko SUZUKI, Yasutaka NISHI, Masaki MATSUBARA, Atsushi MURAMATSU and Kiyoshi KANIE

フレキシブルデバイスの作製において，耐熱性の乏しい樹脂基板への透明導電膜の低温成膜は重要な技術である．ミストデポジションは超音波振動子を用いて霧化させた原料を基板に吹き付けて成膜する手法である．高温処理が不要であることから樹脂基板への成膜に適した手法だと考えられる．本報告ではミストデポジションと以前我々が報告した高水分散性酸化インジウムスズ（ITO）ナノ粒子を組み合わせて透明導電膜の作製を試みた．ミストデポジションで作製した ITO ナノ粒子膜は他の成膜法で成膜した場合よりも低い表面粗さと低い抵抗率を示した．成膜条件の制御が容易なミストデポジションを用いることで膜内部，表面での ITO ナノ粒子の凝集を抑制する条件の調整が可能であり，高性能透明導電膜の作製が可能であることが分かった．

In process of preparation of flexible device, providing a low-temperature coating method of transparent conductive film for polymeric a substrate with low heat tolerance is very important. Mist deposition is a suitable method for coating these substrates as high-temperature processes are not required. Herein, mist is formed by atomizing the coating liquid. Subsequently, it is deposited on the substrate and dried to form a thin film. In this report, a transparent conductive film is prepared utilizing mist deposition and indium tin oxide (ITO) nanoparticles with high water dispersibility, as detailed in our previous report. The mist-deposited ITO thin film exhibits the lowest roughness and resistivity when compared to the films formed using other coating methods. The results indicate that a densely packed film can be prepared by changing the coating conditions, which are easily controlled during the mist deposition. Thus, a high-performance transparent conductive film is successfully prepared using an “eco-friendly” process without high-temperature treatment.

Key words ミストデポジション法，ITO ナノ粒子，透明導電膜
mist deposition method, ITO nanoparticles, transparent conductive film

1 Introduction

Recently, low-temperature processes for the fabrication of electric wiring on substrates with poor heat tolerances have become important technologies owing to the growth of flexible devices [1] and film-type solar cells [2]. In particular, printed electronics (PE), which is the direct drawing of electrical wirings onto a substrate using conventional printing methods [3]–[5], is one of the most attractive technologies. Resist coating, exposure, and etching, which are included in the conventional process for fabrication of the electrode, are not necessary in the PE process. Therefore, PE has the advantages of low environmental load and low cost. However, the drawing of electrical wiring requires the use of conductive pastes, which results in a higher resistivity of PE electric wirings than that of the conventional process.

Indium tin oxide (ITO) is a transparent conductive oxide with low resistivity, high transparency, and moderate chemical stability and is the most commonly used material for transparent electrodes [6]. Transparent conductive films

† Reuse of R. Suzuki, Y. Nishi, M. Matsubara, A. Muramatsu and K. Kanie, “A nanoparticle-mist deposition method: fabrication of high-performance ITO flexible thin films under atmospheric conditions,” *Sci Rep*, vol. 11, pp. 10584, 2021.

using ITO nanoparticles have been prepared by inkjet-printing [7]–[9] and brash printing [10], [11]. In these reports, organic solvents and dispersants were used for the preparation of ink containing ITO nanoparticles; therefore, high-temperature treatment (possibly over 400°C) was necessary to remove organic residue for the preparation of low-resistivity ITO electric wiring. Essentially, only substrates with heat resistance can be used in the PE process.

Mist deposition, which does not use organic solvents and dispersants, has been reported as a method for the fabrication of films consisting of nanoparticles. The mist deposition process is as follows. First, the coating liquid is atomized. The resulting mist is carried by a carrier gas, deposited on the substrate, and dried to form films (Fig. 1a). The mist deposition method is similar to that of spray coating; however, the droplets in the mist are smaller than those in spray coating and remain in the air for a longer period. From this characteristic, mist deposition has the advantages of mist droplet transportation by a carrier gas and control of the film structure by tuning the gas flow. Among the reports on mist deposition, there are several reports on mist chemical vapor deposition (CVD) [12]–[14]. Gallium-doped ZnO (GZO) film and boron-doped ZnO (BZO) film were prepared by mist CVD. On the other hand, there are a few reports on mist deposition using nanoparticles. Qin *et al.* prepared a mist-deposited TiO_2 nanoparticle film [15] where a TiO_2 nanoparticles aqueous dispersion was used as the coating liquid and deposited on a Si wafer heated to 150°C. The obtained films exhibited a characteristic ring pattern on their surfaces. These patterns were formed by the aggregation of TiO_2 nanoparticles during the evaporation of water from the mist droplets on the substrate. Additionally, these patterns differed according to their position inside the Si wafer. These results indicated that mist deposition can be used to fabricate films using a low-temperature process and the surface structure of the film can be controlled by changing the evaporation conditions.

In our previous reports, protruded ITO nanoparticles [16] had a much higher water dispersibility than conventional cubic-shaped ITO nanoparticles [17]. The protruded ITO nanoparticles were single-crystalline nanoparticles with many protrusions on their surfaces, which resulted in a larger surface area and higher surface water absorption than cubic-shaped ITO nanoparticles. These protruded ITO nanoparticles could maintain their dispersion state in an aqueous medium for over one month without any dispersant. Hence, protruded ITO nanoparticles can be applied for mist deposition because of their high water dispersibility. Therefore, we expect that protruded ITO nanoparticles can form densely packed and flat surfaced films using mist deposition during a low-temperature process.

Herein, we report the advantages of mist deposition for the fabrication of transparent conductive films and the advantages of using protruded ITO nanoparticles for mist deposition.

2 Experimental Procedure

ITO nanoparticles were prepared as described in our previous reports [16], [17]. Two types of ITO nanoparticles, C-NP and P-NP, were prepared, which were cubic-shaped and protruded ITO nanoparticles, respectively, with an Sn doping of 14 at%. C-NP and P-NP powders were added to water and dispersed using a homogenizer to prepare an aqueous dispersion of ITO nanoparticles. P-NP had a higher water dispersibility in water than C-NP because of the high hydrophilicity originated from its shape. P-NP maintained a good dispersibility for over one month; whereas, C-NP settled at the bottom of the vessel after standing for one day.

ITO thin films on the substrates were prepared using the mist deposition system (Fig. 1b, 1c). The mist generation unit consisted of four ultrasonic oscillator units. The mist produced from ITO nanoparticle aqueous dispersion was transported by an N_2 carrier gas and deposited on the substrate. On the way, it was passed through a water trap to remove large mist droplets. The flow rate was fixed at 10–20 $L \cdot min^{-1}$ and the resulting thin films were heat treated in air. The thickness of the ITO thin films was adjusted to 300 nm by controlling the deposition period.

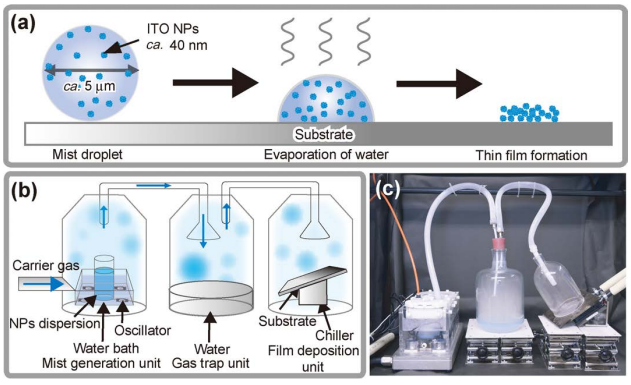

Fig. 1 (a) Scheme of film formation by mist deposition, (b) scheme of mist deposition system, and (c) appearance of experimental mist deposition system.

3 Results and Discussion

3.1. Preparation of C-NP and P-NP

From X-ray diffraction (XRD) measurement, it was confirmed that C-NP and P-NP had In_2O_3 crystal structure

(JCPDS No. 6-0416). Then, the doping amounts of Sn based on In calculated from the inductively coupled plasma (ICP) results were 14.4 mol% and 14.2 mol% in C-NP and P-NP, respectively. From these results, it was confirmed that ITO was successfully prepared. Transmission electron microscopy (TEM) and high-resolution TEM (HR-TEM) images of C-NP and P-NP are shown in Fig. 2. C-NP had a cubic shape with smooth edge surfaces (Fig. 2a), whereas P-NP had a large number of protrusions on the surface (Fig. 2c). The mean particle size of C-NP and P-NP were 39 ± 12 and 38 ± 10 nm, respectively. In the HR-TEM images (Fig. 2b, 2d), C-NP and P-NP showed uniform crystal orientations. The crystallite sizes of C-NP and P-NP were calculated to be 35 and 33 nm, respectively, using Scherrer's equation. The calculated sizes were close to the mean particle diameters determined by TEM observations. The results suggested that C-NP and P-NP have single-crystalline structures. Additionally, the uniform distribution of In and Sn atoms in the nanoparticles was confirmed by energy-dispersive X-ray spectroscopy (EDS) mapping images. These results indicate the successful preparation of the two types of ITO nanoparticles.

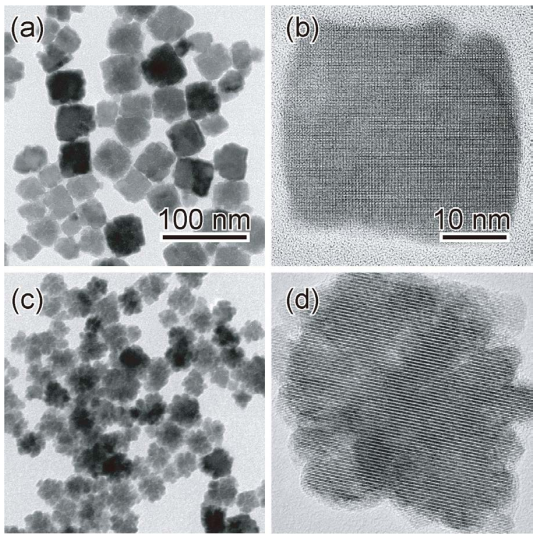

Fig. 2 Transmission electron microscopy (TEM) images of (a) C-NP and (c) P-NP, and high resolution (HR)-TEM images of (b) C-NP and (d) P-NP.

3.2. Effect of Deposition Method on Resistivity of P-NP Thin Films

To investigate the effect of the coating methods on resistivity, a glass substrate was coated with P-NP using several coating methods: mist deposition, bar coating, spray coating, spin coating, and drop casting. Fig. 3a shows the resistivities of P-NP thin films prepared by the different coating methods after heat treatment at 150, 200, 300, 400, and 500°C for 1 h under an H_2-Ar (4% H_2) atmosphere.

The mist-deposited P-NP film had the lowest resistivity (9.0×10^{-3} Ω·cm) after heat treatment at 150°C. At the same process temperature, the resistivities of the films fabricated by bar-coating, spray coating, spin coating, and drop casting were 3.0×10^{-1} Ω·cm, 4.0×10^{-2} Ω·cm, 5.0×10^{-2} Ω·cm, and 4.0×10^{-2} Ω·cm, respectively. The resistivity of the thin films decreased with increasing process temperature for all coating methods. After heat treatment at 500°C, the mist-deposited films had the lowest resistivity 5.0×10^{-3} Ω·cm. Fig. 3b–3f show scanning electron microscopy (SEM) images of the surfaces of the P-NP films after heat treatment at 150°C. From the SEM images (Fig. 3b, 3c, 3e), it was observed that P-NP films prepared by the mist deposition, spray coating, and spin coating methods had flat and smooth surfaces. In contrast, the bar-coated (Fig. 3d) and drop-casted (Fig. 3f) P-NP films had rough surfaces with aggregated P-NP structures. The roughness (R_a) of the P-NP film surfaces was measured by atomic force microscopy (AFM). The mist-deposited P-NP films had the lowest R_a of 7.6 nm. Additionally, bar-coated, spray-coated, spin-coated, and drop-casted P-NP films exhibited an R_a of 7.8, 10.0, 15.8, and 12.6 nm, respectively. In a previous report [18], the resistivity of ITO thin film decreased with decreasing R_a. In this study, the P-NP film with the lowest R_a exhibited the lowest resistivity.

Above mentioned about mist deposition, the evaporation rate of liquids in the droplets can be adjusted by controlling the substrate temperature and carrier gas flow rate, which reduces the agglomeration of nanoparticles in the mist droplets and on the substrates. The insets of Fig. 3b–3f show

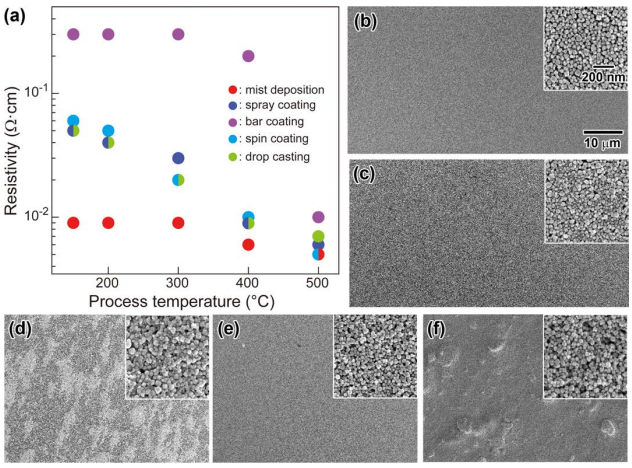

Fig. 3 (a) Resistivities of P-NP films prepared by different coating methods and scanning electron microscopy (SEM) images of P-NP film surface coated by (b) mist deposition, (c) spray coating, (d) bar coating, (e) spin coating, and (f) drop casting methods. These images were taken after annealing at 150°C. The insets in (b)-(f) are enlarged views of the surfaces.

enlarged views of the corresponding P-NP film surfaces. A densely packed uniform surface was observed, as shown in Fig. 3b, which indicates that mist deposition is advantageous for fabricating high-performance ITO thin films at low processing temperatures and is applicable to flexible films.

3.3. Characterization of Mist-Deposited C-NP and P-NP Films

ITO thin films were prepared by mist deposition using aqueous dispersions of C-NP and P-NP. Fig. 4a summarizes the resistivities of the C-NP and P-NP films fabricated by mist deposition in a low process temperature between room temperature and 200°C. Resistivities of the C-NP and P-NP films after annealing at 150°C were 8.0×10^{-2} Ω·cm and 9.0×10^{-3} Ω·cm, respectively. Fig. 4b–4c presents SEM images of the surfaces of the C-NP and P-NP films after annealing at 150°C, respectively. The C-NP film had a rough and porous surface structure. In contrast, a densely packed and flat surface was observed on the P-NP film. The lower resistivity of the P-NP film compared to that of the C-NP film can be attributed to the more densely packed structure of the P-NP film. Fig. 4d–4e present cross-sectional TEM images of C-NP and P-NP films on a polyethylene naphthalate (PEN) substrate (TEONEX, Q51-188, TOYOBO Co., Ltd., Osaka, Japan, t = 188 μm) with thicknesses of ca. 200 nm. These images correspond to the SEM images shown in Fig. 4b–4c. Loosely deposited porous inner structure with voids and irregularities was observed in the C-NP film. Additionally, a densely deposited inner structure of the P-NP film was observed. The difference in film structure between the C-NP and P-NP films is attributed to the difference in the dispersion states of C-NP and P-NP in the mist water droplets.

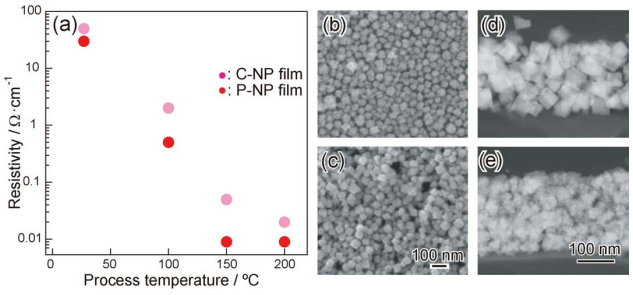

Fig. 4 (a) Resistivity of C-NP and P-NP films after heat treatment between room temperature and 200°C, scanning electron microscopy (SEM) images of the surfaces of the (b) C-NP and (c) P-NP films after annealing at 150°C, and cross-section transmission electron microscopy (TEM) images of (d) C-NP and (e) P-NP particles on polyethylene naphthalate (PEN) substrate.

The dispersion states of C-NP and P-NP in the mist water droplets were investigated using small-angle X-ray scattering (SAXS) measurements. In the water droplets, the mean particle size of particles in P-NP was 41 ± 13 nm, which was consistent with the size determined by TEM observation. This result indicates that P-NP were the primary particles in the water droplets. In contrast, C-NP had two particle sizes in water droplets, 54 ± 10 and 159 ± 30 nm. The smaller and larger sizes corresponded to the C-NP dispersed as primary and secondary particles, respectively. It was assumed that the high water dispersibility of P-NP resulted in a primary particle state in the water droplets. From these results, the stability of the ITO nanoparticles in aqueous dispersions was maintained in the mist water droplets and primary-dispersed nanoparticles can be used to form thin films with densely packed structures.

Furthermore, the effect of the ITO nanoparticle dispersion state was investigated. C-NP and P-NP films prepared using different elapsed times after the preparation of the aqueous dispersions were fabricated and their resistivities were measured (Fig. 5). The resistivity of the C-NP films increased as the elapsed time of the C-NP aqueous dispersion increased. Conversely, the P-NP films maintained a low resistivity regardless of the elapsed time. As mentioned in Section 2, C-NP has a lower water dispersibility than P-NP and settles at the bottom of the vessel after standing for one day. These results corresponded to the results that the high water dispersibility of P-NP was appropriate for high-performance ITO nanoparticle thin films.

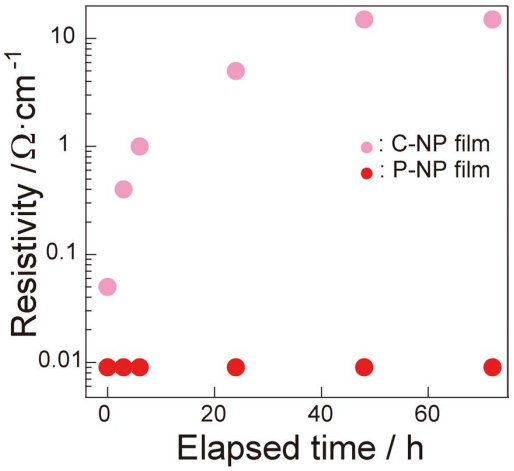

Fig. 5 Effect of elapsed time after preparation of indium tin oxide (ITO) nanoparticle dispersion on resistivity of mist-deposited film.

3.4. P-NP Mist Deposition on Flexible Films

P-NP was coated on a flexible PEN substrate by mist deposition with 300 nm thickness followed by annealing at 150°C for 1 h under N_2 atmosphere. The resulting P-NP film

showed high transparency (Fig. 6a) and had a low resistivity of 9.0×10^{-3} Ω ·cm, which is similar to the resistivity of P-NP film on a glass substrate. Additionally, the transmittance of this P-NP film was greater than 85% in the visible region (Fig. 6b). It was assumed that a highly transparent ITO thin film could be obtained on a flexible film by mist deposition. Furthermore, P-NP patterned films were fabricated by mist deposition on pre-treated hydrophilic flexible films. The method for selective deposition was as follows. First, Novec 1720 (3M) was precoated onto a PEN film (TEONEX, Q51-50, TOYOBO Co., Ltd., Osaka, Japan, t = 50 μm or t = 188 μm) to prepare a hydrophobic surface. The films were dried at 100°C for 30 min. The films were masked using a patterned SUS430 thin substrate (t = 100 μm). The resulting masked PEN films were treated with a UV-ozone cleaner for 5 min to obtain patterned hydrophilic areas. Fig. 6c and Fig. 6d exhibit an SEM image and the corresponding EDS mapping image of the P-NP film In ions on a PEN substrate, respectively. The water droplets in the mist spontaneously were deposited on the hydrophilized area of the flexible films to form a uniform pattern. Selective and spontaneous processes will become a powerful technique for fabricating ITO-patterned films under ecofriendly atmospheric roll-to-roll PE conditions.

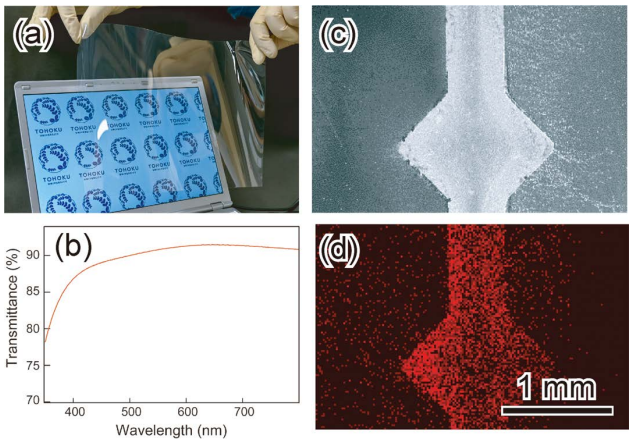

Fig. 6 (a) Appearance of P-NP film on polyethylene naphthalate (PEN) substrate coated by mist deposition, (b) transmittance spectra of the P-NP film, (c) scanning electron microscopy (SEM) image, and (d) corresponding energy-dispersive X-ray spectroscopy (EDS) mapping image of P-NP film In ions on patterned PEN substrate.

4 Conclusion

The design and synthesis of protruded ITO nanoparticles with high water dispersibility have been detailed in our previous report. ITO nanoparticles are one of the most stable materials for the fabrication of thin films using mist deposition. In this study, we prepared flexible films with high-performance ITO thin film on flexible film, that had low resistivity and high transparency using a combination of mist deposition and protrusion-rich ITO nanoparticles. A comparison to cubic ITO nanoparticles with low water dispersibility revealed that the high water dispersibility of protrusion-rich ITO nanoparticles played a critical role in fabricating high-performance ITO thin films. The high dispersibility of protrusion-rich ITO nanoparticles was maintained in mist water droplets. Protruded ITO nanoparticles were deposited on substrates in a primary particle state, and densely packed films were formed. The ITO thin films obtained by mist deposition have the following advantages. (i) Single-crystalline protrusion-rich ITO nanoparticles are readily dispersed in water for a long period without the use of surfactants or dispersants. (ii) ITO nanoparticle-based thin films can be fabricated under mild atmospheric conditions without the use of expensive vacuum production systems or dangerous and environmentally-harmful chemicals that are used in the current sputtering and etching procedure. Finally, (iii) Low resistivity and high transparency can be achieved with low-temperature annealing, which is applicable for the deposition of ITO thin films on flexible substrates. Mist deposition is a promising and powerful technique for the production of key materials essential for sustainable progress in PE technology as well as next-generation on-demand fabrication processes for wearable devices.

References

[1] J. Koo, D. Kim, H. Shim, T. Kim and D. Kim, "Flexible and Stretchable Smart Display: Materials, Fabrication, Device Design, and System Integration," *Adv. Funct. Mater.*, vol 28, no 35, pp. 1801834, 2018.

[2] Y. Li, G. Xu, C. Cui and Y. Li, "Flexible and Semitransparent Organic Solar Cells," *Adv. Ener. Mater.*, vol. 8, no 7, pp. 1701791, 2018.

[3] Y. Kamikoriyama, H. Imamura, A. Muramatsu and K. Kanie, "Ambient Aqueous-Phase Synthesis of Copper Nanoparticles and Nanopastes with Low-Temperature Sintering and Ultra-High Bonding Abilities," *Sci. Rep.*, vol. 9, pp. 899, 2019.

[4] D. Li, W.-Y. Lai, Y.-Z. Zhang and W. Huang, "Printable Transparent Conductive Films for Flexible Electronics," *Adv. Mater.*, vol. 30, no. 10, pp. 1704738, 2018.

[5] Y. Khan, A. Thielens, S. Muin, J. Ting, C. Baumbauer and A. C. Arias, "A New Frontier of Printed Electronics: Flexible Hybrid Electronics," *Adv. Mater.* vol. 32, no. 15, pp. 1905279, 2020.

[6] T. Minami, "Present status of transparent conducting oxide

thin-film development for Indium-Tin-Oxide (ITO) substitutes," *Thin Solid Films*, vol. 516, no. 17, pp. 5822–5828, 2008.

[7] M. Hwang, B. Jeong, J. Moon, S. Chun and J. Kim, "Inkjet-printing of indium tin oxide (ITO) films for transparent conducting Electrodes," *Mater. Sci. Eng. B*, vol. 176, no. 14, pp. 1128–1131, 2011.

[8] D. Angmo, T. T. Larsen-Olsen, M. Jørgensen, R. R. Søndergaard and F. C. Krebs, "Roll-to-Roll Inkjet Printing and Photonic Sintering of Electrodes for ITO Free Polymer Solar Cell Modules and Facile Product Integration," *Adv. Ener. Mater.*, vol. 3, no. 2, pp. 172–175, 2013.

[9] E. N. Dattoli and W. Lu, "ITO nanowires and nanoparticles for transparent films," *MRS Bull.*, vol. 36, no. 10, pp. 782–788, 2011.

[10] J. Jeong and H. Kim, "Ag nanowire percolating network embedded in indium tin oxide nanoparticles for printable transparent conducting electrodes," *Appl. Phys. Lett.*, vol. 104, pp. 071906, 2014.

[11] H. Shin, K. Kim, T. Kim and H. Kim, "Fiber laser annealing of brush-painted ITO nanoparticles for use as transparent anode for organic solar cells," *Ceram. Int.*, vol. 42, no. 12, pp. 13983–13989, 2016.

[12] T. Kawaharamura, G. T. Dang and M. Furuta, "Successful Growth of Conductive Highly Crystalline Sn-Doped α-Ga_2O_3 Thin Films by Fine-Channel Mist Chemical Vapor Deposition," *Jpn. Appl. Phys.*, vol. 51, pp. 040207, 2012.

[13] T. Kawaharamura, "Physics on development of open-air atmospheric pressure thin film fabrication technique using mist droplets: Control of precursor flow," *Jpn. Appl. Phys.*, vol. 53, pp. 05FF08, 2014.

[14] T. Shirahata, T. Kawaharamura, S. Fujita and H. Orita, "Transparent conductive zinc-oxide-based films grown at low temperature by mist chemical vapor deposition," *Thin Solid Films*, vol. 597, pp. 30–38, 2015.

[15] G. Qin and A. Watanabe, "Surface Texturing of TiO_2 Film by Mist Deposition of TiO_2 Nanoparticles," *Nano-Micro Lett.*, vol. 5, no. 2, pp. 129–134, 2013.

[16] R. Suzuki, Y. Nishi, M. Matsubara, A. Muramatsu and K. Kanie, "Single-Crystalline Protrusion-Rich Indium Tin Oxide Nanoparticles with Colloidal Stability in Water for Use in Sustainable Coatings," *ACS Appl. Nano Mater.*, vol. 3, no. 5, pp. 4870–4879, 2020.

[17] K. Kanie, T. Sasaki, M. Nakaya and A. Muramatsu, "Quaternary Ammonium Hydroxides-Assisted Solvothermal Synthesis of Monodispersed ITO Nanoparticles with a Cubic Shape," *Chem. Lett.*, vol. 42, no. 7, pp. 738–740, 2013.

[18] W. Tang, Y. Chao, X. Weng, L. Deng and K. Xu, "Optical Property and the Relationship between Resistivity and Surface Roughness of Indium Tin Oxide Thin Films," *Phys. Procedia*, vol. 32, pp. 680–686, 2012.

鈴木涼子　Ryoko SUZUKI
先進技術開発本部 材料・要素技術研究所
Materials & Advanced Research Laboratory
Advanced Technology Research & Development Division
東北大学
Tohoku University

西　康孝　Yasutaka NISHI
東北大学
Tohoku University
FPD 装置事業部 開発統括部 先端技術開発部
Advanced Technology Development Department
Development Sector
FPD Lithography Business Unit

松原正樹　Masaki MATSUBARA
東北大学
Tohoku University

村松淳司　Atsushi MURAMATSU
東北大学
Tohoku University

蟹江澄志　Kiyoshi KANIE
東北大学
Tohoku University


鈴木涼子
Ryoko SUZUKI


西　康孝
Yasutaka NISHI


松原正樹
Masaki MATSUBARA


村松淳司
Atsushi MURAMATSU


蟹江澄志
Kiyoshi KANIE

燃焼～溶融のCAEによる機能性評価と感度調整による試作レス開発プロセスの確立†

小西洋平，武村直輝，中野史康，齊藤卓一

Establishment of a Prototype-less Development Process by Functionality Evaluation and Sensitivity Setting using Numerical Simulation for Combustion to Melt

Yohei KONISHI, Naoki TAKEMURA, Fumiyasu NAKANO and Takuichi SAITO

生産本部技術統括部製造部では半導体露光装置やFPD露光装置に使用される高純度合成石英ガラスを製造している．石英ガラス合成は燃焼～溶融といった複雑反応を伴うため，炉内状態の計測や予測が難しい．このため従来はプロセス条件変更による品質，生産性向上のために，複数回の実機による試作～品質確認が必須であり，膨大な開発コストの発生と量産安定性に課題があった．本報では，課題解決のため，実機試作レス開発プロセスを確立したので報告する．

網羅的な機能性評価を行うため，実験は数値シミュレーション（CAE）を用いて行った．CAEを用いた二段階設計を実現するため，まずプロセス機能展開によるシステム全体の俯瞰に取り組んだ．プロセス機能展開は机上で複数の技術者によって行い，プロセス機能展開表としてシステムの見える化をすることができた．ここから抽出された制御因子や誤差因子をとりあげ，CAEを用いて網羅的に評価することで，CAEによる二段階設計を実現した．従来の開発で必要だった実機実験をCAEで代替したことによって，信頼性の高いプロセス条件を短期間で確立することができ，生産性向上を達成した．

Production Department Technology Sector Production Technology Division manufactures high-purity synthetic silica glass used in semiconductor lithography system and flat panel display (FPD) lithography system. Silica glass synthesis involves complicated reactions such as combustion and melting, so it is difficult to measure and predict the state inside the furnace. For this reason, in the past, to improve quality and productivity by changing process conditions, it was essential to perform trial production and quality confirmation with actual machines multiple times, which caused enormous development costs and problems in mass production stability. In this study, we have established an actual prototype-less development process to solve the problem.

Experiments were conducted using computer-aided engineering (CAE) for comprehensive functional evaluation. To achieve a two-step optimization using CAE, we first worked on a bird's-eye view of the entire system by process-function deploying. The process-function deploying was performed by multiple engineers on the desk, and the system could be visualized as a process function deployment table. By taking up the control factors and error factors extracted from this and comprehensively evaluating them using CAE, we achieved a two-step optimization by CAE. By substituting CAE for the actual machine experiment required in the conventional development, highly reliable process conditions could be established in a short period of time, and productivity was improved.

Key words CAE，熱流体解析，品質工学，二段階設計，合成石英ガラス
CAE, Thermo-fluid analysis, Quality engineering, Two-step optimization, Synthetic silica glass

1 はじめに

高純度石英ガラス合成プロセスの生産効率を向上させることを目的に，数値シミュレーション（CAE）を応用した網羅的かつ効率的な技術開発プロセスを確立したため，報告する．

本論文では，まず石英ガラス合成における火炎燃焼～ガラス溶融の各過程を工程における機能として定義した．プ

† 本稿は引用文献［6］に，新たに6.3新規合成炉の開発状況を加えたものである．

ロセス機能展開の手法によりプロセス全体を俯瞰しCAEで直積実験を行うことで，機能性に関する要因効果図を獲得した．さらにCAEでL_{18}実験によって制御因子の感度への効果を評価した．この結果得られたロバスト・エンジニアリング情報（RE情報）を用いて実生産炉の運転条件を設定することにより，試作レスで良品を獲得し，本開発プロセスの信頼性の高さを示した［1］，［2］．

2 背　景

2.1. 合成プロセスの説明

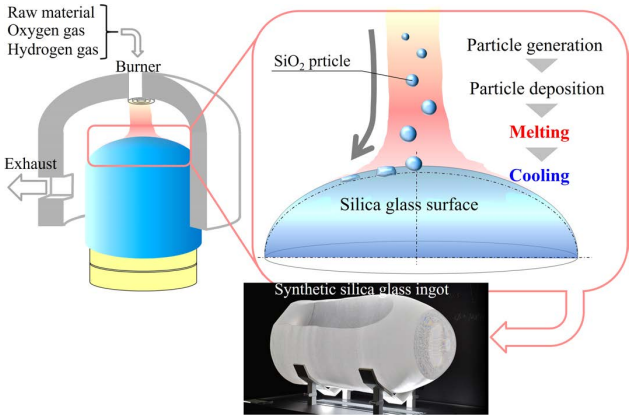

Fig. 1　石英ガラス合成模式図及び石英ガラスインゴット

当社では直接法により光学用途合成石英ガラスを製造している．直接法石英ガラスでは，バーナーから酸素，水素といった燃焼ガスと，原料となる塩化ケイ素ガスを供給することで，火炎を形成し，火炎中の化学反応によりシリカ微粒子を生成する．生成されたシリカ微粒子を石英ガラス表面に堆積させながら，バーナー火炎によって堆積物を加熱溶融することで高純度な石英ガラス塊（インゴット）を得ることができる（Fig. 1）．

合成中の石英ガラス表面は高温にさらされることで溶融し，インゴット外周側にガラスが流れて広がる過程を経て低温となり固化する．この石英ガラスの溶融から冷却までの過程によって石英ガラスの光学的品質は変化するため，合成中の炉内環境を一定に保つことが品質の安定性に対して重要である．一方で周囲環境の様々な変動により，合成中の石英ガラス周囲の温度場，ガス濃度場が絶えず変化するので，これらの変動に対して石英ガラスの品質を変動させにくい炉内構造設計，合成条件が求められる．

我々は石英ガラスの歩留まりを改善させるため，取得する石英ガラス部品の品質を変更せずに合成するインゴットを小型化することによって，合成にかかるリードタイム（L/T）短縮，廃棄されるガラス重量の最小化に取り組んだ．

2.2. 課題

石英ガラス合成炉内では，火炎中の加水分解反応，粒子堆積，溶融，冷却といった現象が同時に起きており，かつ炉内での合成期間が長いため，以下の課題を抱えていた．

①炉内状態の把握，評価が難しい．

②操業中の条件変更による実験のコストが高く，再現性のある条件改良検討が難しい．

③インゴットのサイズを変更しつつ，同じ品質の部品を作製することが難しい．

そこで，石英ガラス品質を維持しつつインゴットサイズを変更するための合成条件設計のため，CAEを用いた機能性評価プロセス開発を試みた．

3 対策－評価の進め方

3.1. プロセス機能展開とシステム分割

炉内燃焼の網羅的な把握に向けて，システムの機能を明確にするため，まずプロセス機能展開を行った．複数の技術者による協議を行った上で，石英ガラス合成炉及び周辺設備・環境に関わるパラメーターを抽出し，プロセス機能展開表にまとめた．プロセス機能展開を行った結果，炉に関わる各パラメーターはいくつかの補助的な機能（サブシステム）に分けて整理できることが分かった．

3.2. サブシステムの機能とシステム範囲

石英ガラス合成システムに付随するサブシステムの機能として，我々は，①原料供給，②粒子合成，③粒子堆積，④溶融，⑤冷却，の５つの機能に分割して考えた．それぞれのサブシステムの工程における機能を，

①原料供給：

設定供給量に対して常に安定した供給量にする．

②粒子合成：

火炎中で生成されるシリカ粒子の粒子径分布を常に一定にする．

③粒子堆積：

堆積するシリカ微粒子の堆積量が石英ガラス表面の位置ごとのシリカ微粒子堆積量分布を一定にする．

④溶融，⑤冷却：

堆積によって生成した石英ガラスの表面に与えられる熱量の分布を時間的に常に一定とする．

とそれぞれ定義した．石英ガラス合成システムに付随する制御因子（設計パラメーター及び操業パラメーター）は，一つのパラメーターが複数のサブシステムの機能に影響していると考えられる．例えばバーナーを通じて火炎の温度をコントロールすることができるが，これによって②粒子合成，③粒子堆積，④溶融，⑤冷却，の各サブシステムに対してそれぞれ別種の変化を与えると予想できる．このため，パラメーターを変化させた際の個別のサブシステムご

との評価を行うのではなく，システム全体を一つの実験で総合的に評価する必要があると判断した．

3.3. 機能の定義と評価指標

今回のシステムの評価指標と機能について検討を行った．合成中の石英ガラス表面では，中心部分の温度が高い領域でガラスが溶融し，溶融したガラスが周辺部へと流動して広がっていく過程で冷却され，固化する．よって，合成される石英ガラスの状態を一定にするためには，溶融～流動～冷却の過程に生じる温度変化のばらつきを評価しなければならない．

しかし，高温酸性ガス環境である実生産炉内でガラスの流動速度変化や，それに伴う温度変化を時間とともに観測することは困難である．そこで CAE による評価を検討した．CAE を適用した場合の問題は，高温のガラスの流動が長時間にわたる非定常的な現象であるため，計算負荷が高いことであった．ただし，石英ガラスの溶融～流動～冷却による固化の過程は，いずれも温度変化によって制御される過程である．つまり，ガラス表面に加わる熱エネルギー収支（熱流束）の変動を評価できれば，非定常性を直接表現しないまでも，ガラス流動の変動に対する代替指標として適用できると考えた［3］．

3.4. 予備実験による評価部位の確認

予備実験として，石英ガラス表面の熱流束分布を変化させた条件下での CAE 及び実際の石英ガラス合成の小規模実験を行い，評価の妥当性検証を行った．

バーナーに供給するガス流量，流速を変化させて，熱流束を変更した条件（条件 1，2，Fig. 2）を設定した．CAE 解析から，条件 1 では熱流束の大きい領域が石英ガラスインゴット表面の右側に偏っているのに対して，条件 2 では中心付近にあることがわかる．熱流束が小さい領域では，ガラスの流動速度が遅くなり，熱流束が大きい領域ではガラスの流動速度が速くなるため，条件 2 で合成したガラスインゴットは回転対称な形状を維持し，条件 1 では回転対称形状を維持できないと予想される．

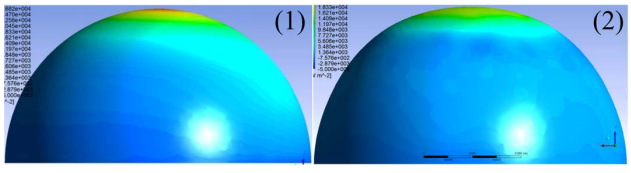

Fig. 2　石英ガラス表面の熱流束分布図（CAE）
（1）条件 1，（2）条件 2

実際に合成したインゴットの合成中の様子を比較すると（Fig. 3），条件 1 では熱流束が大きい側のガラスが流動によって片減りして，回転対称な形状を維持できないことが確認された．

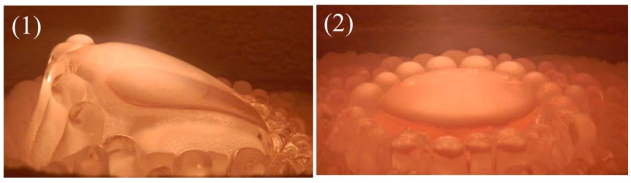

Fig. 3　各テスト条件で合成された石英ガラスインゴット
（1）条件 1，（2）条件 2

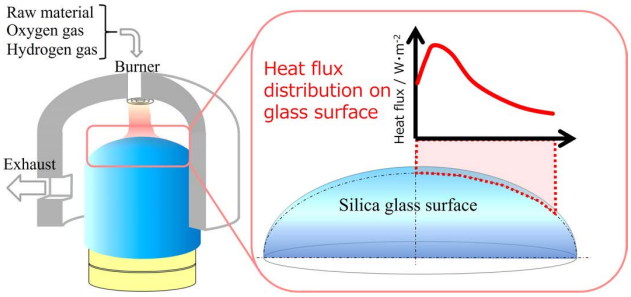

Fig. 4　石英ガラス表面熱流束分布評価の模式図

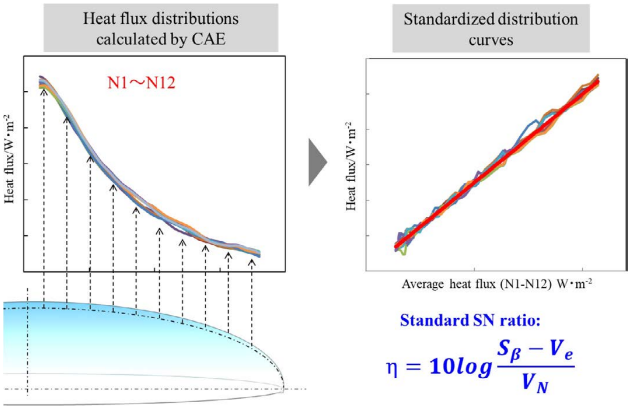

Fig. 5　基本機能（熱流束分布）と標準 SN 比評価の模式図

合成されたインゴットの品質悪化の主な原因は合成中のインゴット表面でのガラス流動の不均一であるから，以上の予備実験より，CAE 解析で得られる石英ガラス表面の位置ごとの熱流束の分布（中心：高い，周辺低い，Fig. 4）を評価することが必要と判断した．

そこで合成中の石英ガラス表面の中心からの位置を信号とし，シミュレーションによって算出される各位置の熱流束を出力とし，各位置における熱流束の誤差に対する安定性を評価することにした（Fig. 5）．

3.5. CAE による実験方法

実験は CAE 解析ソフト中に作製したシミュレーションモデルにより行った．シミュレーションモデルは，実物の設置寸法，壁面及び各ガス種の物性値を境界条件として数値化し，有限要素法による数値計算を行った．

モデル上で直交表に対応して CAE の境界条件を変更させるため，解析ソフトと自動最適化用ソフトを連動させることで，CAE によって自動で直積実験を実行することができた．

3.6. 誤差因子と水準

CAE の実験はばらつきを持たないため，誤差因子についてはプロセス機能展開表から実際のプロセス変動に関する11因子を抽出した．実際に起こりうる製造条件の変動幅を，仮想的な誤差として L_{12}外側直交表に割り付け，実生産炉におけるプロセス変動を再現することにした［4］，［5］．

3.7. SN 比算出方法

CAE で得られた熱流束分布は各実験行の平均値に対する値のばらつきを標準 SN 比として評価した．標準 SN 比は

$$\eta = 10 \log \frac{S_\beta - V_e}{V_N} \quad (1)$$

式で算出した．Fig. 5 に CAE で得られた 1 行分（12サンプル）の熱流束分布曲線と，各位置における熱流束の平均値を標準条件（N_0）として，標準条件の出力を信号（横軸）にしたグラフの例を示す．

4 CAE による機能性評価結果

4.1. 制御因子の決定

制御因子はプロセス機能展開表を基に，各サブシステムに属する制御因子から46因子を取り上げ，二つの L_{36}内側直交表にそれぞれ23因子ずつ割り付けた．誤差因子は先に取り上げた11因子を L_{12}外側直交表に割り付け，２回の $L_{36}\times L_{12}$の直積実験を CAE で行った．実験リードタイム短縮の観点から，二つの直交表を並行して計算させることを考えた．プロセス機能展開表にあるすべての因子を公平に評価するため，二つの直交表の間で誤差因子を共通とすることにした．

4.2. 実験結果

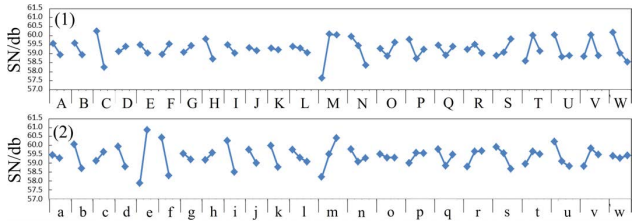

Fig. 6　要因効果図（標準 SN 比）
（1）１バッチ目，（2）２バッチ目

得られた２回分の $L_{36}\times L_{12}$実験の要因効果図を示す（Fig. 6）．

得られた要因効果図の最適条件と比較条件の確認実験を行い，利得の再現性を確認した（Table 1）．Table 1 の確認実験の利得から，今回の１度目と２度目の実験ともに利得の再現性が得られていると判断した．

Table 1　確認実験結果

	1st batch/db			2nd batch/db		
	Best	Comparison	Gain	Best	Comparison	Gain
Estimated	70.8	58.5	**12.3**	68.5	62.6	**5.9**
Confirmation experiment	70.2	59.3	**10.9**	69.4	61.5	**7.9**

5 CAE による感度情報の獲得と調整

5.1. 理想熱流束分布の定義

$L_{36}\times L_{12}$実験で得られた要因効果図から，SN 比に効果が大きい因子と効果の小さい因子があることがわかった．SN 比への効果が大きい因子は，操業上 SN 比が高くなる水準に固定するべきなのに対し，効果が小さい因子は目的を最大化するための感度調整に適用できると考えた．次にこの感度調整因子を用いた感度調整方法について検討した．

3.4節で述べたように，合成中の石英ガラス形状を維持するためには，熱流束分布を適切な状態に保つ必要がある．そこで着目しているインゴットを小型化した場合の石英ガラス表面の熱流束分布を CAE で調査したところ，Fig. 7 のようになることが分かった．

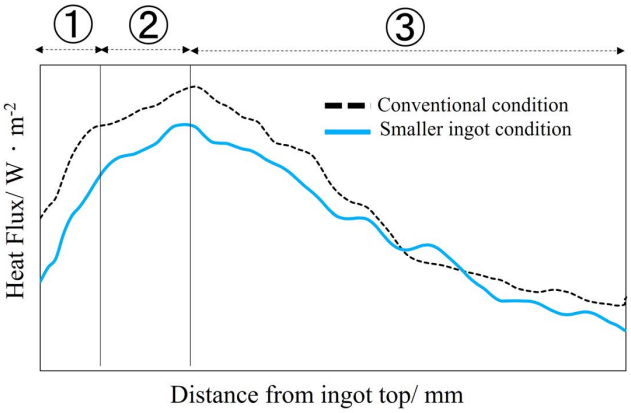

Fig. 7　従来条件と小径化条件での熱流束分布の比較

Fig. 7 から，インゴットサイズを変化させることで，石英ガラス表面の熱流束が中心付近で大きく低下することが示唆された．感度調整因子を用いて現行の操業条件の熱流束分布に合わせこむ事ができれば，インゴットサイズを小型化させた際にも品質を安定させたまま合成することができると考え，CAE による感度情報の取得を試みた．

5.2. 感度情報の取得

Fig. 7 に示した熱流束分布は，いずれも複数の変曲点を持つ分布形状を示している．この分布形状への感度調整を行うため，得られた熱流束分布の変曲点ごとにデータを①，②，③のように区切り，それぞれの区間に対する感度を算出することにした．これは，感度調整を行うにあたり，ガラス表面の中心付近の熱流束と，外周付近の熱流束を別個

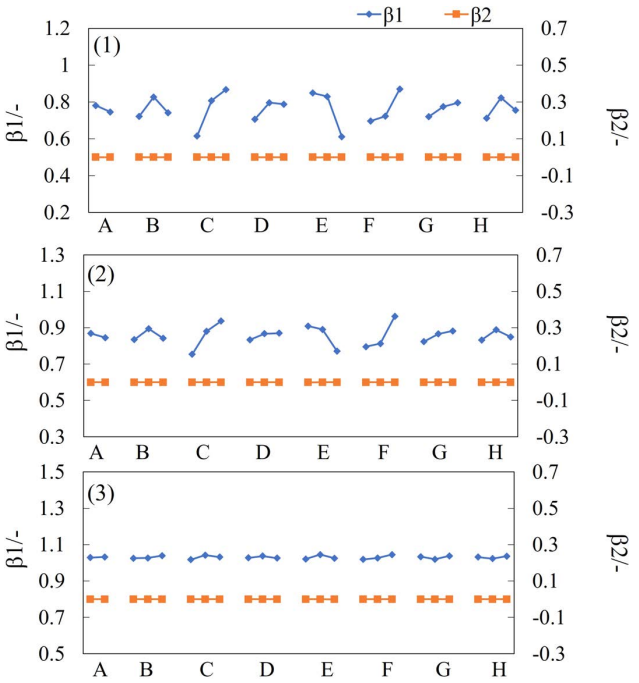

Fig. 8　β1，β2についての要因効果図
（1）区間①，（2）区間②，（3）区間③

に変化させることによって，全体の熱流束分布を制御する必要があると考えたためである．

また二次の曲率成分の評価を行うため，感度はチェビシェフの一般直交多項式に従う計算方法でβ1，β2までを算出し，現行操業条件を理想と置いた時の感度に対する効果を CAE による L_{18}直交表実験により解析した［1］．この時予め感度調整因子とした因子以外は SN 比が大きい水準に固定して実験を行った．

Fig. 8 に L_{18}直交表実験で得られた感度の要因効果図を示す．要因効果図から，各因子の感度に対する効果と，理想条件への合わせこみのための感度調整の方向を把握することができた．ここまでの取り組みにより，各制御因子について，標準 SN 比及び感度の要因効果を得ることができた．これらの要因効果図をサブシステム及びプロセス機能展開表に紐づけて整理することで，石英ガラス合成システムに関するロバスト・エンジニアリング情報（RE 情報）として，網羅的な設計情報にまとめることができた．

6 実生産炉での検証と展開

6.1. CAE での操業条件決定

得られた RE 情報を基に実炉での操業条件を決定するため，インゴットサイズを小さくした条件で感度の要因効果図β1，β2を用いて操業条件への熱流束の感度調整を行った．Fig. 9 に CAE による感度調整で得られた条件での熱流束分布を示す．Fig. 9 より，中心側の熱流束が増加し，全体の分布形状が現行条件に近づいていることが確認できた．

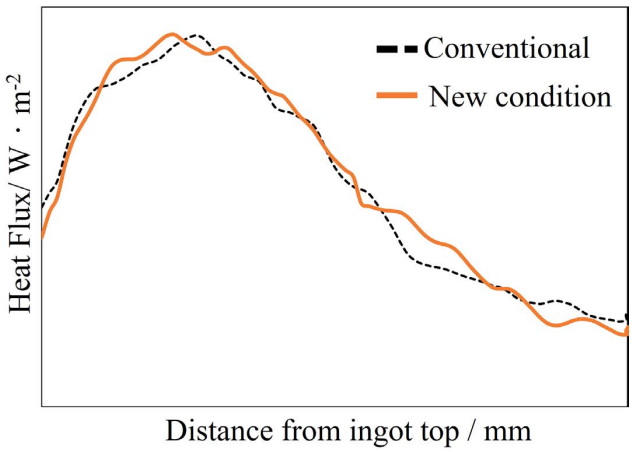

Fig. 9　従来条件と感度調整後の小径化条件の熱流束分布比較

6.2. 実生産炉での合成条件の調整と決定

得られた条件を適用して実生産炉合成を行ったところ，試作一回目の合成から安定した形状の石英インゴットを得ることができた．このことから，CAE により得られた RE 情報が現実のシステムを表現できていることを確認した．

また得られた合成条件を生産展開することで，当初のねらい通り，品質を変化させずに 1 バッチあたりの L/T の短縮及び歩留まりの低減を達成した．それぞれ，L/T は従来比84%，部品あたりの投入費用は従来比72%に低減できた．ここから，時間当たりの投入費用から見た生産性（L/T 短縮率×部品コスト低減率）を従来の1.6倍とすることに成功した．今回の CAE による取り組みにより大幅な損失コストの低減に成功した．

6.3. 新規合成炉の開発

我々はさらに生産性の高い石英合成を目指し，現在石英ガラス合成炉の熱効率改善に取り組んでいる．ここでは，石英ガラス合成炉構造を変更することにより，石英ガラス合成に必要な酸水素ガス使用量を低減することを目的としている．石英ガラス表面の熱流束についての CAE 解析から得られた RE 情報（Fig. 6）を用いて検討することにより，SN 比への寄与が大きい因子として炉内吸気口形状及び排気口の位置が重要であることが示唆された．そこで，これらの因子を現行よりも SN 比が大きくなる側へ水準変更し，SN 比の安定性を担保した．そのうえで目的の熱効率を高めるため，炉内容積を20%低減することとした．Fig. 10 に今回新規に設計した炉での石英ガラス表面熱流束の CAE 解析結果を示す．なお，新規炉での解析では，6.1節で述べた感度調整と同様の手法により操業条件を設定している．Fig. 10 に示した熱流束分布の結果から，新規炉においても現行と同様の熱流束分布を再現できることが確認された．また感度調整により得られた新規炉での操業条件では，酸水素ガス使用量が約20%減となっており，目的とする熱効率の改善効果が得られることが予想された．

以上のように，CAE を用いた二段階設計により，新規炉

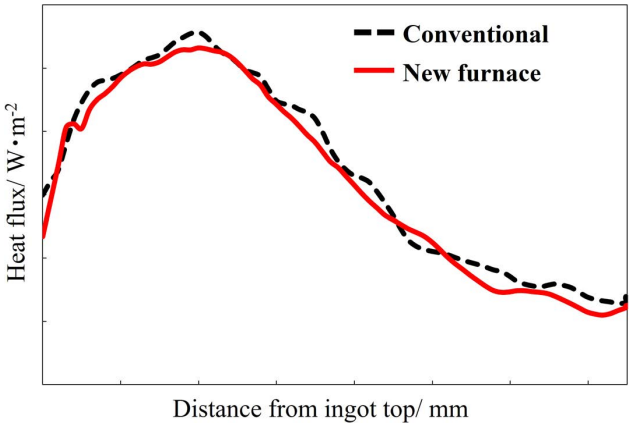

Fig. 10　従来条件と新規炉での熱流束分布の比較

構造を短い期間で，かつ RE 情報からの根拠を持って決定することができた．設計した新規炉は現在製作を完了し，実合成での品質確認を行っている．また実際に酸水素ガス量を低減した条件で合成を行い，石英インゴットが取得できることを確認できており，今後の生産性への寄与を目指して開発を継続している．

7 まとめ

本研究では，石英ガラス合成プロセスの生産効率を向上するため，まずプロセス機能展開を行うことで網羅性のある制御因子，誤差因子の抽出を行い，合成炉内環境の CAE による機能性評価を行った．次に理想の熱流束分布曲線を考慮した感度調整を行い，実生産炉に適用可能な製造条件を見出した．

本論文では，石英ガラス合成の開発を通じて，機能性評価手法の効果を確認できた．複雑な現象を伴うパラメーターの効果を機能に対する要因効果としてプロセス機能展開表上に整理することで，定量的かつ網羅的な技術情報として蓄積した．CAE による熱流束分布形状の感度調整と，実生産炉での効果を確認したことで，CAE を用いた試作レスの開発プロセスを確立することができた．

以上により得られた RE 情報は，今回機能として選んだ熱流束分布だけでなく，他の品質及び生産性課題についても汎用的に適用できるものである．今後今回得られた RE 情報を用いて，石英ガラス合成の更なる生産性向上及び高品質化に取り組んでいく．

引　用　文　献

[1] 田口玄一，横山巽子，*ベーシックオフライン品質工学*，日本規格協会，2008.
[2] 嘉指伸一，“プロセス機能展開表の活用とロバストエンジニアリング情報の活用による初期型不良の撲滅と立上げリードタイムの短縮，”*全国能率大会*，63, pp. B73-76, 2012.
[3] 水谷幸夫，*燃焼工学　第 3 版*，森北出版株式会社，2013.
[4] 嘉指伸一，“品質工学を実務で活用する「品質工学ステップ展開」，”*標準化と品質管理*，vol. 69, no. 9, pp. 57-69, 2016.
[5] 佐藤幸太，嘉指伸一，“プロセス機能展開表を活用した光学ガラスの溶解技術開発，”*品質工学*，vol. 29, no. 1, pp. 30-38, 2021.
[6] 小西洋平，武村直輝，齊藤卓一，“燃焼～溶融の CAE による機能性評価と感度調整による試作レス開発プロセスの確立，”*第29回品質工学研究発表大会*，No. 5, pp. 20-25, 2021.

小西洋平　Yohei KONISHI
生産本部 技術統括部 製造部
Production Department
Technology Sector
Production Technology Division

武村直輝　Naoki TAKEMURA
生産本部 技術統括部 製造部
Production Department
Technology Sector
Production Technology Division

中野史康　Fumiyasu NAKANO
生産本部 技術統括部 製造部
Production Department
Technology Sector
Production Technology Division

齊藤卓一　Takuichi SAITO
生産本部 技術統括部 製造部
Production Department
Technology Sector
Production Technology Division

小西洋平
Yohei KONISHI

武村直輝
Naoki TAKEMURA

中野史康
Fumiyasu NAKANO

齊藤卓一
Takuichi SAITO

Nikon Research Report Vol. 4
Published September 2022

NIKON CORPORATION